From Melting Dynamics to Medical Diagnostics: Studies in Geochemical Kinetics

Thesis by

Emily Yishiuan Miaou

In Partial Fulfillment of the Requirements for

the degree of

Doctor of Philosophy

CALIFORNIA INSTITUTE OF TECHNOLOGY

Pasadena, California

2025

Defended December 10, 2024

© 2025

Emily Miaou
ORCID: 0000-0003-4688-3024

ACKNOWLEDGEMENTS

It is with immense gratitude that I dedicate my PhD to the following people and entities that shaped both my work and my personal growth. I would not be where I am today without them.

First and foremost, I must express my appreciation for the faculty members who have supported and guided me: Paul Asimow, François Tissot, George Rossman, and Ed Stolper. I would like to thank the random number generator that assigned Paul to be my freshman advisor in 2014—this bit of luck really changed my life. Paul, I could not have asked for a better advisor, both as an undergrad and as a PhD student. In undergrad, it was a privilege to have you as an instructor. Your excitement for ideas, big and small, combined with your patience and ability to convey those concepts to students of all levels, helped grow my appreciation for the geosciences. Taking Ge1 as a frosh had a profound impact on my education and career; thank you for entrusting me to TA the class during the last five iterations and give back to the course that shaped my trajectory all those years ago. As my PhD advisor, you taught me how to approach scientific problems in a systematic and quantitative way, and to never lose enthusiasm for the pursuit of knowledge. I have had the unique opportunity to learn from you as a theorist, experimentalist, and field geologist, and you have inspired me to improve in all of those directions. I cannot thank you enough for the last ten years. François, I am so grateful to have had such a trailblazing and zealous PhD co-advisor. Thank you for seeing the potential in me during our first year at Caltech together and encouraging me to pursue and perform truly interdisciplinary work. I admire your attention to detail and commitment to best practices in everything you do, and learning from you has undoubtedly made me a better scientist. George, thank you for taking me into your lab when I was a freshman and teaching me what it meant to do geology research. I feel so fortunate to have found you early on during my time at Caltech. In addition to being an indispensable resource during my research pursuits, I have always appreciated that you were invested in and looking out for my future. Your ever-relevant question, “where do

you want to be in five years?" will be in the back of my mind as I move forward in life. Ed, thank you for being a fountain of wisdom and for always being willing to share your ideas. It has been an absolute pleasure to work with you and Paul together as a dynamic duo.

My research could not have been accomplished without the patient assistance and counsel of many others as well. Mike Baker, thank you for keeping me alive in the igneous petrology labs and for sharing your experimental wisdom. I owe every successful experiment to your efficient and pragmatic solutions. I am grateful to the members of the Isotoparium, especially Michael Kipp, Gerrit Budde, and Eugenia Hyung, for teaching me all I know about operating in a clean lab. To my collaborators at City of Hope, Ravi Salgia and Tamara Mirazoiapova, thank you for providing medical insight on our work together and for generously sharing your lab spaces with me.

To my cohort – Juliet Ryan-Davis, Philip Woods, Sergio Parra, Elliott Mueller, Shaelyn Silverman, Ren Marquez, Xenia Boyes, Haoyu Li, Carl Swindle, Sarah Zeichner, and Makayla Betts – you are such a wonderful, dynamic group, and I am so grateful I could share the PhD journey with you. As one of the youngest in the crew, I really appreciated and learned from your varied perspectives. Juliet, thank you for being the free spirit and connector of the group. It has been a privilege to be a part of your life and capture some of your joyous milestones on camera. Philip, thank you for sharing a home with me for the last four years. You (and Maple) have made our apartment a happy place for me to return to at the end of each day. Ren and Haoyu, your camaraderie in the Isotoparium was invaluable. To everyone, thanks for the chats and laughs over hikes, good food, and coffee breaks. Pits forever!

The GPS department is special in a way that cannot be put into words. I could not have asked for a better place to spend my grad school years. Krittanon Sirorattanakul, thank you for letting me rope you into Science Olympiad, chatting about life on our regular boba runs, and being a reliable friend over the last six years. Henry Peterson, James Atterholt, and David Bonan, Iceland would not have been the

same without you. Ruolin Deng, Juan David Hernández-Montenegro, Theresa Marlin, Renee Wang, Guannan Dong, Eran Funaro, and Oliver Wilner, thank you for making my time in the department even more enjoyable. Julie Lee, you are a ray of sunshine, and I am so grateful for your hard work behind the scenes.

I would be remiss if I did not acknowledge the positive influences of my past educators who taught me to love STEM and gave me the skills and confidence to get to where I am today. To my grade school teachers Jamie Bassett, Michelle Jedlicka, John Tollett, Bart Taylor, Casey Akin, Vanita Vance, Jan Fechhelm, and Nancy Boswell, thank you for going above and beyond for your students. The hours spent after school and during weekends helping us pursue our passions will never be forgotten. Mike Vicic, thank you for your dedication to undergraduate education at Caltech. The ChE option has benefitted infinitely from your presence. Camille McAvoy, Alison Tisdale, and Kelly Zhang, I am grateful for your compassionate research mentorship during my undergraduate years that inspired me to pursue a PhD.

Competing in the Science Olympiad event Rocks & Minerals was my first exposure to quantitative geology, and I will always be indebted to this organization for helping me find my love for geosciences. Leading Science Olympiad outreach during my PhD has added so much purpose to my life—working with talented and devoted individuals around the country to help inspire the next generation of scientists has been an incredibly rewarding experience. Dustin Schroeder, thank you for entrusting me with the future of the National Earth & Space Science Committee. Peter Hung, Kevin Kha, Eric Ma, Albert Kyi, Christopher Wang, Edward Zhang, and the rest of the SoCal/Caltech Science Olympiad planning team, I will always appreciate the warm and supportive community you provided over the last ten years. Peter, thank you for being a great role model and one of the kindest people I know; you hold us all together.

To all the members of the Caltech Squash Club, thank you for enriching my life and sharing my love for the sport. I would like to give special mentions to Fan Wu, Shaowu Zhang, and Ruizhe Wang. Fan, thank you for excitedly stopping me en

route to the gym two and a half years ago to ask if the racquet in my bag was a squash racquet; the rest is history. You inspired me to start building the squash community on campus, and I would not be the player I am today without you. Ivan and Roger, you have been great friends both on and off the court, and I am excited for you to carry the torch for the club in coming years. It has been wonderful to grow and improve with you all.

My PhD experience has also been enhanced by others in the broader Caltech community. To my College Station Texpats: Zachary Wu, Brandon Zhao, and Brooke Versaw, thank you for being lifelong friends and for providing a slice of home away from home. Peishi Cheng, Daniel Wackelin, and Emile Oshima – you are all such caring individuals, and my life has been much better with you in it.

To the LA locals outside of Caltech who kept me grounded: Haojie Zhuang and Cindy Cao, thanks for the adventures. Tyler Okamoto, thank you for sharing my enthusiasm for Pokémon Go. Herman Au and I-Jou Tsai, I am grateful you took a chance on me and helped me grow as a photographer. Crystal Liang, it has been a treat to be your neighbor and cat-sitter. Joseph Lee, you go the distance for your friends, and I am beyond privileged to be in your circle.

To my friends spread out all over the world, thank you for your regular messages of support and for always being only a phone call away. I am so grateful for our enduring friendships over time and space: Gene Hsu, Vicky Yao, Patrick Lynch, Travis Stebbins, Shreya Shankar, Nahrin Majid, Priyansi Kikani, Sarah Porter, Nick Lindner, Ezekiel Hsieh, Pablo Leon, Victor Leon, Ivy Lee, Bethany Anderson, Abi McDougal, Amanda Gao, Gloria Ha, Stephanie Gu, Erin Wang, Nicholas Hutchins, Aaron Shih, Joe Donermeyer, Anant Desai, Anish Thilagar, Aaron Lin, and Terry Huang.

Thank you to my extended family, Eric, Elaine, Eugene, and Tiffany Miao, for taking care of me while I have been at Caltech. It has been a great source of

comfort to have you all nearby, and it has been wonderful to spend time together and grow closer throughout the last ten years.

To my parents, Shaw-Pin Miaou and Yuh-Ru Chen, I owe everything to you. To my dad, thank you for showing me the definition of hard work and dedication to your craft. From you, I have learned to always do the right thing, no matter how difficult; that if I am going to do a job, I must do it well. Though you are no longer with us, your ideas and values live on in me. To my mom, thank you for supporting me in my endeavors, no matter how near or far. You are capable and meticulous in everything you do, and there is no one I trust more in the world. I only become more grateful to you both as time goes on, and I hope I have made you proud. I love you both very much.

ABSTRACT

This thesis investigates geochemical kinetics across different subfields, from isotope metallomics in the human body to melting dynamics in igneous petrology. Chapters II and III explore the chemical complexities of rapid mineral melting in igneous systems. An experimental-computational approach is used, with the experiments providing data that help calibrate the numerical model. This integrated strategy contributes to a comprehensive understanding of the kinetics of melting that could not be captured by either method alone. Chapter II outlines the experimental work, which includes both equilibrium and kinetic melting experiments performed on the ubiquitous igneous mineral series plagioclase. The kinetic experiments are designed to deliberately access a parameter space of disequilibrium behaviors rarely studied experimentally yet likely to be relevant in various natural settings where systems evolve too quickly to follow the predictions of equilibrium theory. Quantitative and qualitative analyses of the recovered experimental products allow us to observe unique textures and chemical gradients that arise from the interplay of thermal and chemical diffusion within the phases, coupled with phase boundary motion and associated surface reactions. Chapter III details the theory and computational methods used to develop a numerical model that describes chemical evolution of melt and crystal phases during two-component melting. Novel application of thermodynamic data is used to describe chemical behavior at the phase boundary, allowing for departure from traditional equilibrium assumptions. Results of the model bring us one step closer to the ultimate goal of understanding disequilibrium in multicomponent rock systems. Chapter IV investigates the kinetics of stable isotopes in biomedicine. Box modeling was used to simulate copper (Cu) stable isotope dynamics in the human body, allowing us to quantify the possible effects of various health conditions (*e.g.*, cancer, liver disease) on isotopic compositions throughout different organs. In turn, we determine whether Cu isotopes can act as diagnostic or prognostic markers for certain diseases using detection by modern mass spectrometry and provide recommendations on their potential uses in the medical field.

PUBLISHED CONTENT AND CONTRIBUTIONS

Chapters 2 & 3 are to be submitted as:

Miaou, Emily, and Asimow, P.D. Kinetics of rapid melting in two-component systems.

Both authors participated in project conceptualization and experimental design. E.M. performed the experiments, data collection & analysis, numerical model development, figure preparation, and manuscript writing. P.D.A. supervised the project and contributed to data interpretation and manuscript preparation.

Chapter 4 is published as:

Miaou, Emily, and François L.H. Tissot (2023). Copper isotope ratios in serum do not track cancerous tumor evolution, but organ failure. In: *Metallomics* 15(11): mfad060. DOI: 10.1093/mtomcs/mfad060

Both authors participated in project conceptualization. E.M. performed the model development, data analysis & visualization, and writing. F.L.H.T supervised the project and contributed to data interpretation and manuscript preparation.

TABLE OF CONTENTS

LIST OF FIGURES

Number *Page*

LIST OF TABLES

NOMENCLATURE

Delta notation – A system used to express the relative abundance of isotopes in a sample, relative to a standard. It is often represented as $\delta^x A = [({}^{x/y}R_{sample} / {}^{x/y}R_{standard}) - 1] * 1000$, where *A* is the element of interest, *x* and *y* are isotopes of *A* (with *x* typically being the heavier isotope), and *R* being the ratio of *x* to *y* present in the sample or standard. The units are usually expressed in per mil (‰).

Equilibrium – The condition in which the concentrations of reactants and products in a chemical reaction remain constant over time, as the rates of the forward and reverse reactions are equal. The expected end state of a chemical process. At the system level, a state where all reactions have gone to completion and no macroscopic variables change during the period of observation.

Isotope – Variants of a particular chemical element that differ in the number of neutrons in their nuclei and thus have different atomic masses. Isotopes of an element have nearly the same chemical properties but may differ in physical properties such as stability and radioactivity, and may be fractionated from one another by equilibrium, kinetic, or resonant processes.

Kinetics – The study of rates of reactions and the mechanisms by which they proceed.

Liquidus – In thermodynamics, the temperature above which a material is completely liquid. On a temperature-composition phase diagram at a given pressure, the two-phase region lies below this line and above the solidus.

Metallomics – The study of functions, interactions, and distribution of metals in biological systems, including their effects on metabolism and health.

Plagioclase – A solid solution series of tectosilicate minerals within the feldspar group, characterized by a range of compositions between albite ($NaAlSi_3O_8$) and anorthite ($CaAl_2Si_2O_8$). Plagioclase is a common constituent of igneous rocks.

Solidus – In thermodynamics, the temperature below which a material is completely solid. On a temperature-composition phase diagram at a given pressure, the two-phase region lies above this line and below the liquidus.

Stable Isotope – An isotope of an element that does not undergo radioactive decay over time.

Stefan problem – A mathematical problem concerning the evolution of a body undergoing phase change, such as ice melting into water. It involves the study of the

movement of the phase boundary and how it is influenced by temperature, time, and material properties.

Thermodynamics – The study of how energy is transferred and transformed and the laws that govern its behavior, providing a macroscopic perspective of the properties of systems at equilibrium.

C h a p t e r 1

INTRODUCTION

"All models are wrong, but some are useful." – George E. P. Box

Thermodynamics is the study of how energy is transferred and transformed and the laws that govern its behavior. It provides a macroscopic perspective of the properties of systems, allowing us to understand important concepts such as equilibrium. *Kinetics* is the study of rates of reactions and the mechanisms by which they proceed. It provides the critical details about timescales and paths taken to achieve equilibrium.

It may seem strange that the opening sentences of a thesis containing "kinetics" in the title are about thermodynamics, but it is difficult to talk about one without the other in many scientific pursuits. Though equilibrium as understood by thermodynamics provides an expected end state of a chemical process, we may not be able to observe systems on sufficiently long time scales to ensure they have reached this point. Instead, the snapshots in time that we see as scientists, ranging from fractions of a second up to a human lifetime, may instead reflect intermediate states in a kinetic pathway. One classic example of observing kinetic rather than thermodynamic behavior is with diamonds: thermodynamics predicts that diamonds are not the most stable form of carbon at standard temperature and pressure and should turn into graphite. However, the transition from diamond to graphite takes billions of years, and it is physically impossible for one person to observe the end state of reaction. Hence, thermodynamic equilibrium gives us a destination, but kinetics describes the journey. Together, they provide a more complete story.

Historically, attempts to explain many natural geochemical phenomena have utilized equilibrium assumptions due to their sound theoretical basis and the tractability of such problems. However, over time, with the improvement of

technology and therefore observational resolution and computational ability, we are able to more easily discern and understand the complexity in cases where kinetics dominate. Using a combination of forward modeling and experimental methods, this thesis explores the ways that kinetics and thermodynamics are intertwined in different systems, as well as the wide range of phenomena encompassed by both. We acknowledge the distance that equilibrium studies have taken us thus far and attempt to build on this body of work by integrating the kinetic perspective, taking us one step closer to a true understanding of natural processes. This body of work investigates geochemical kinetics in two very different domains: phase changes in multicomponent mineral systems and stable metal isotope signatures in human diseases.

Chapters II and III present a combined experimental-computational approach to understanding the melting of minerals under disequilibrium conditions. The interplay of chemical diffusion within and between phases, coupled with a moving phase boundary, creates deviations from equilibrium behavior. Most approaches to this problem have nonetheless assumed that the melt and mineral phases are always in equilibrium at their common boundary; the approach presented here is designed to allow for the relaxation of that constraint to explore whether this leads to a more useful predictive theory. Chapter II describes the suite of equilibrium and kinetic heating experiments performed on an intermediate plagioclase composition, a common igneous mineral series that exhibits binary solid solution and melt/solid chemical fractionations. The experiments span a wide range of heating rates in order to provide a baseline for describing melting behavior in natural systems across various time and length scales. We observe and describe an interesting range of melting textures and compositions generated by these experiments and offer possible explanations for their formation. Chapter III builds upon the experiments, developing a numerical model of melting that departs from traditional equilibrium assumptions as a means to further probe the nuances of melting kinetics in magmatic systems. The current model is one-dimensional. It incorporates thermodynamic descriptions

of the plagioclase and melt phases tuned to reproduce the correct equilibrium behavior and to provide quantitative estimates of the driving forces for system evolution, and it allows for the coupling of multiple fluxes in response to those driving forces (interdiffusion of the two chemical components in each phase, motion of the boundary, and chemical exchange *across* the boundary), each of which may be rate-limiting in the approach to equilibrium melting behavior. We offer further insight on the experimental observations by comparison to model results.

Chapter IV shifts to kinetics from a biomedical perspective, utilizing the powerful geochemical tool of stable isotopes. We develop a box model that accurately simulates copper (Cu) stable isotope kinetics in the human body, then use this model to examine possible perturbations to a healthy Cu metabolism during illnesses such as cancer or liver disease. The results of these simulations help elucidate both the potential and limitations for the Cu stable isotope ratio to act as a biomarker under various conditions and timescales, allowing me to make recommendations to the community regarding its utility in the medical field.

Melting Dynamics

Geochemists have historically treated many of Earth's natural processes with equilibrium assumptions. For magmatic systems especially, the long geologic timescales and high temperatures associated with processes like mantle convection, magma storage, and eruption may appear at first glance to be appropriate justifications for assuming equilibrium as a first-order approximation. Partial melting in particular is a crucial process that dictates much of the geochemistry we observe on Earth's surface, including both oceanic and continental crust formation, exchange of matter between interior and surface reservoirs, volcanism, and the development of many economically significant ore deposits. Several simplified models or paradigms are commonly used to guide understanding of melting in magmatic systems, with two primary factors that distinguish them from each other: (1) whether melt is segregated as it forms and (2) the extent to which gradients within the solid phase

relax towards homogeneity. In all common models, diffusion in the liquid/melt phase is reasonably assumed to occur significantly faster than the rate of melting, supported by empirical data. Below, we identify and discuss the validity of the assumptions used in a few standard melting scenarios that arise from different choices of the two factors mentioned above, using a common and simple two-component system, olivine (Figure 1.1):

- *Batch melting* – Melting of the bulk material occurs with no melt extraction. Both solid and liquid phases are allowed to equilibrate completely at each step of melting, meaning each phase is always homogeneous. For this to be true, diffusion in the solid is assumed to be fast enough to relax completely any chemical gradients that would arise as a result of temperature changes. Because this is a closed system, the final total melt composition must match that of the original solid, and melting is complete at the intersection of the liquidus curve and the starting composition, as shown in Figure 1.1a.

- *Fractional melting* – As melting begins, a thin film of liquid is considered to exist in equilibrium with a homogeneous solid. This layer of melt is then assumed to be removed and isolated from any further reaction with the solid. Because the equilibrium melt composition differs from the source solid composition, continuing this process requires the solid to evolve in composition as temperature rises. The assumption of homogeneity in the solid thus requires sufficiently rapid solid-state diffusion, compared to the timescale of melt extraction, that the changes in solid composition developing at the grain boundary propagate all the way to the grain centers. Upon further melting of the solid, a new liquid-solid equilibrium contact is formed, and that new melt is again extracted from interaction with the solid, possibly to be mixed with prior increments of liquid in a separate reservoir. In a simple binary system such as olivine, this series of discretized equilibrium steps approaches, in the limit of infinitesimal steps, an overall melting scheme

shown in Figure 1.1b. We can see that the solid and liquid composition will change over time in accordance with the phase loop: the first melt formed is more Fe-rich and the remaining solid evolves towards higher concentrations of Mg. Residual solid will persist all the way to the maximum on the solidus, at the pure Mg end member.

- *Disequilibrium melting* – The rate of diffusion in the solid is taken to be much slower than the melting rate. In the limiting case, each layer of melt inherits the homogeneous composition of the layer of solid that is stripped away immediately. As a result, the compositions of both the solid and liquid should theoretically always remain the same as the starting material. The phase loop then collapses instead into a line—an unstable, pseudo-unary equilibrium, at some temperature intermediate between the equilibrium solidus and liquidus curves—as the instantaneous compositions of the solid and liquid do not change, shown in Figure 1.1c. In this model, complete melting is expected to happen at a single temperature. It begins at a temperature higher than the equilibrium solidus and ends, surprisingly, at a temperature lower than the equilibrium liquidus.

The above theories of melting require solid state diffusion assumptions at opposite extremes, either occurring very quickly or not at all. However, real physical systems certainly exhibit behavior in between these two extremes — finite solid-state diffusion rates that allow development and maintenance of compositional gradients (zoning) within the solid. Ultimately, accurate descriptions and models of melting need to move away from any of the limiting models and their severe assumptions to capture the behavior of real systems. Therefore, Chapters II and III explore the numerous complexities behind melting in natural systems under different heating rate regimes, including compositional gradients in the solid and melt, phase partitioning of the major elements, and melt fraction as a function of changing temperature. In

order to accomplish this, we incorporated kinetic considerations that are not apparent from equilibrium phase diagrams such as those shown in Fig. 1.1.

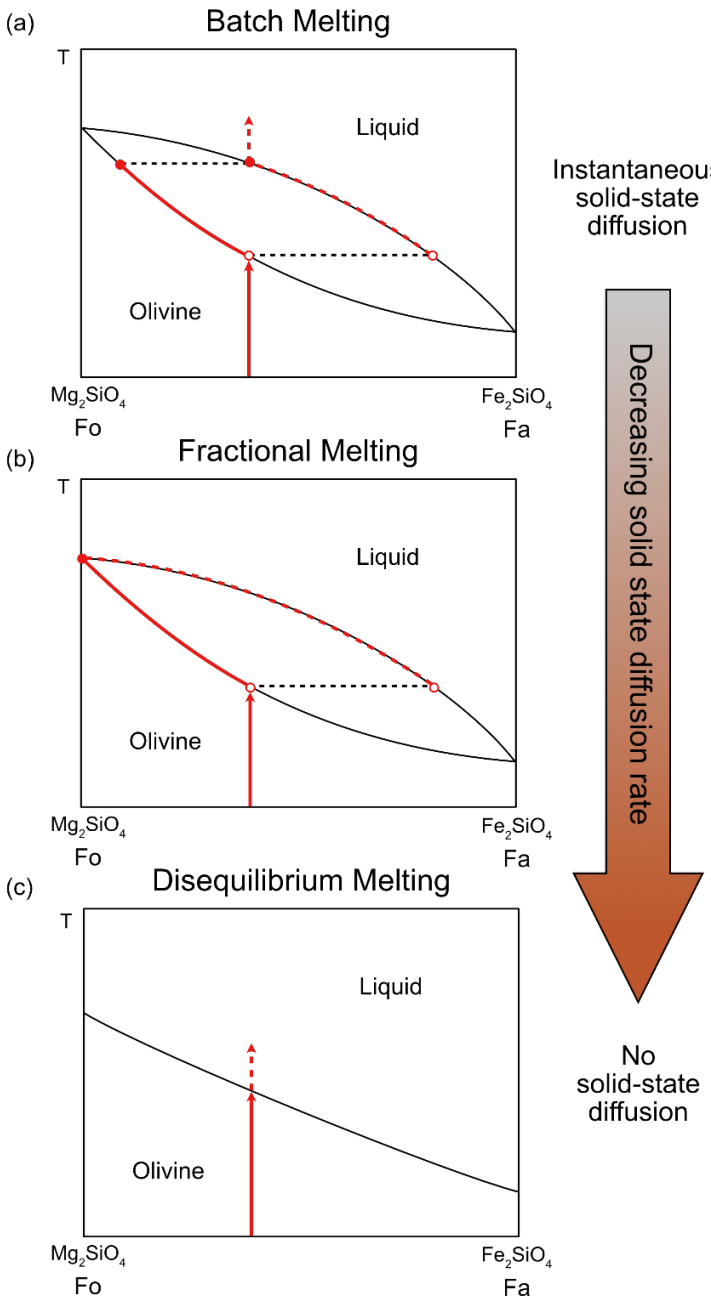

Figure 1.1. *Melting models.* Melt/liquid composition is mapped by dotted arrows, while the solid phase is represented by the solid arrows.

There exist a wide range of approaches by which one might investigate the kinetics of rapid melting in geologic materials. These include analysis of natural samples, controlled experiments (in furnaces, quasi-static compression apparatus, or shock facilities), and computational models. The chemical, isotopic, and petrological properties of natural samples are of course fundamental, but such studies may be sample-limited or inconclusive because natural objects have extended histories that may include complex formation processes or multiple alteration events that are difficult to reconstruct by inverse modeling. Laboratory-controlled experiments continue to offer essential insights but are time-consuming and constrained by available samples, facilities, instruments, etc. to certain combinations of pressure (*P*), temperature (*T*), and duration. Computational forward modeling in a vacuum provides us with reproducible data based on fundamental physical principles, but often falls short of describing empirical observations due to their simplistic nature. Pursued in isolation, experimental and computational methods each have strengths and limitations. Pursued in parallel, they can bring about dramatic gains in understanding. Therefore, we performed a simple, well-defined set of complementary experimental and computational studies to probe the relationship between diffusion and phase change. Their results informed and validated each other in their respective development and ultimate application.

Medical Diagnostics

Isotope metallomics is the study of the distribution, role, and impact of metal isotopes in biological systems. Common organic elements — such as C, H, O, N, and S — are transferred between compounds and reservoirs by a vast variety of biological reactions in the human body and are therefore difficult to connect to any specific biological process. In contrast, metals tend to play more unique functional roles, and their turnover rates in the body are relatively rapid, making it possible for observations of their dynamics to inform us about specific processes and their timescales in the body. Isotopes are well-established as powerful tracers of physical and chemical processes in geosciences, and the development of the Multi-Collector

Inductively Coupled Plasma Mass Spectrometer (MC-ICP-MS) made it possible within the last few decades to routinely perform high-precision isotopic measurements of metabolically critical metals (*e.g.*, Cu, Ca, Fe) in biological samples. This technological advancement allowed for pioneering studies to be done in the past decade to build a basic understanding of metal isotopes in the context of the human body.

Isotope geochemistry is built upon observations of the partitioning, or fractionation, of isotopes of a given element into different reservoirs of a system. Causes of isotope fractionation can be divided into two major categories: equilibrium and kinetic (Figure 1.2). Molecular bonds can be approximated as harmonic oscillators due to the roughly linear relation between atomic displacements and the restoring force acting on the atoms in the molecule, and their vibrational frequency can be expressed as

$$\nu = \frac{1}{2\pi}\sqrt{\frac{k}{m}} \quad (1)$$

where k is a spring constant and m is the mass of the atom (for a case where the mode is dominated by motion of a single atom; more generally a reduced mass μ may describe common motion of two atoms or a system of atoms). Therefore, the heavier the isotope participating in a bond, the lower the vibrational frequency and energy state. This relationship contributes to the zero-point energy (ZPE) of molecules — lighter isotopes of an element have a higher ZPE than heavier isotopes when bonded. At equilibrium, it is thermodynamically favorable for heavier isotopes to participate in bonding relative to lighter isotopes of the same element because of this energy minimization, generally causing molecules with comparatively strong chemical bonds to select for heavier isotopes. In contrast, kinetic isotope effects occur during rapid, incomplete, and/or unidirectional processes. Because lighter isotopes have a higher vibrational frequency, they require less activation energy to proceed in a reaction and are capable of reacting faster than heavier isotopes. Figure 1.2 provides

a visualization of the energy differences contributing to each of these fractionation effects.

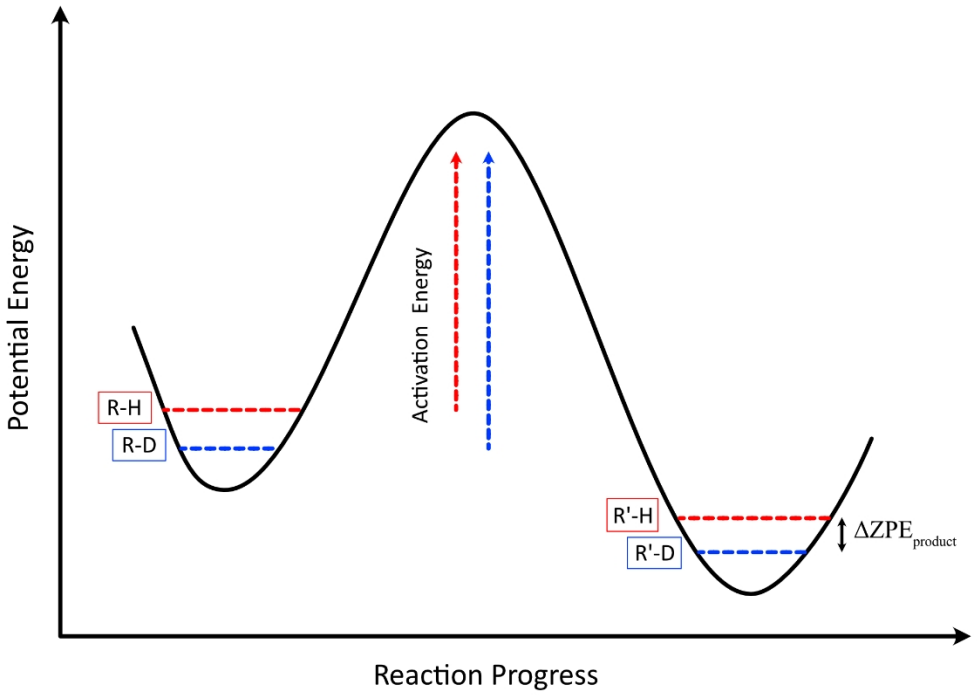

Figure 1.2. *Potential energy vs. reaction progress.* Hydrogen (H) and deuterium (D) participating in the same reaction will have differing reactant and product energies that help determine equilibrium isotope fractionation, as well as different activation energies that dictate kinetic isotope effects.

Isotope fractionation for a given element is expressed using delta notation. This notation uses relative abundances for ease of comparison, shown below for the stable isotopes of copper:

$$\delta^{65}\text{Cu} = \left(\frac{\left({}^{65}\text{Cu} / {}^{63}\text{Cu} \right)_{\text{sample}}}{\left({}^{65}\text{Cu} / {}^{63}\text{Cu} \right)_{\text{standard}}} - 1 \right) \times 1000 \quad (2)$$

The standard, by international consensus, is NIST SRM 976 for Cu. Isotopes in the human body are fractionated through many processes: people take in food with a

certain isotope ratio, which is then absorbed by the digestive system, circulated through the body, and incorporated into various molecules and reservoirs. Each of these steps may involve a series of chemical reactions and/or active/passive transport on the cellular level, with each step approaching equilibrium to some degree and being limited by kinetic factors to some degree. The combination of these processes generates a net isotope fractionation in a given reservoir (*e.g.*, liver, blood, etc.) that can be measured by mass spectrometry. Natural stable isotope variations of Cu and Zn in the organs of healthy humans and other animals are shown below.

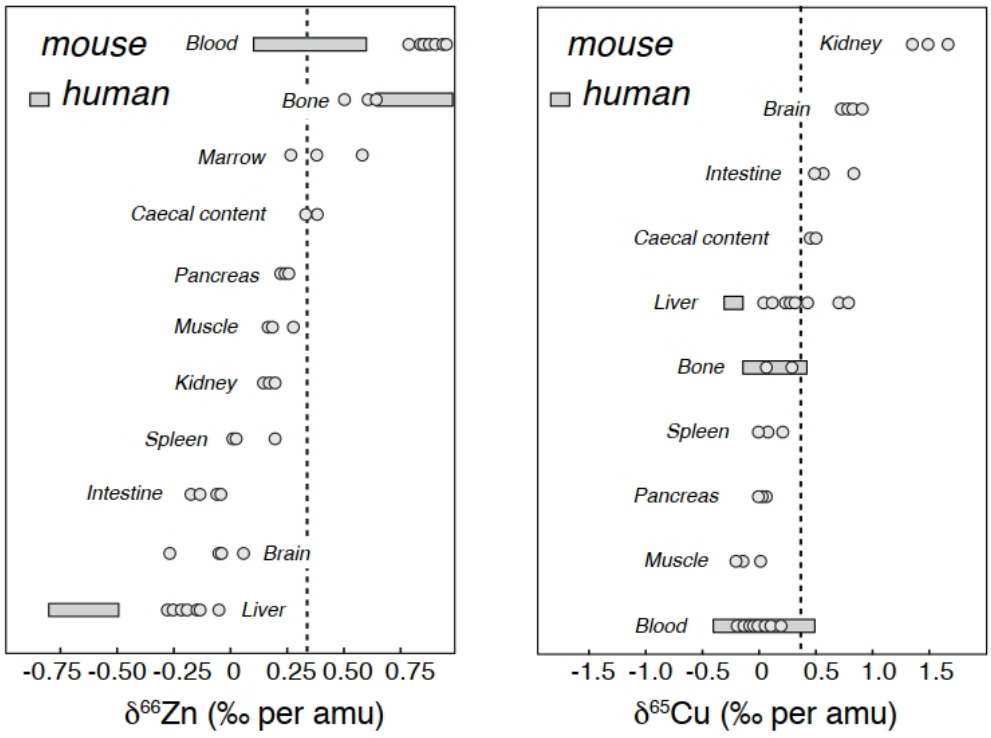

Figure 1.3. *Natural isotope variations in organs.* The dotted line marks the isotopic composition of the diet. Taken from Albarède et al. (2017).

Recent literature in isotope metallomics found that unique isotopic signatures in human samples (*e.g.*, tissue, blood, etc.) are correlated with certain diseases, spurring conversations about the potential for stable metal isotopes to act as routine diagnostic or prognostic tools. These studies paved the way for us to explore the metal

isotope landscape of the human body, bringing forth two major questions that motivate future directions of the field: (1) what do these signatures tell us about the molecular mechanisms that bring about these measurable isotopic changes? For instance, how do kinetic or equilibrium effects due to specific enzymes, transporters, or other proteins dictate these observations? And (2) what are possible applications of these measurements? Even if we do not yet understand all the mechanistic components that contribute to a given measurement, under what conditions could these signatures still serve as prognostic or diagnostic for diseases? Chapter IV focuses on answering these questions, with an emphasis on the applications of stable isotope measurements of Cu.

Chapter 2

KINETICS OF RAPID MELTING IN TWO-COMPONENT SYSTEMS: EXPERIMENTAL METHODS

Introduction

While the evolution of petrological systems through a series of equilibrium states can be reliably predicted using phase diagrams and studied through nominally time-independent experiments, natural processes often proceed at rates that are too fast for strict equilibrium to obtain. This is proven by the existence of zoned crystals (Anderson 1984; Maaløe 1976; Pearce and Kolisnik 1990; Shea, Lynn, and Garcia 2015) or even, in very rapid cases, by zoned glassy melt inclusions (Newcombe et al. 2014; Saper and Stolper 2020). This poses a challenge, because neither phase diagrams nor free energy minimization models can fully define the evolution of systems that depart from equilibrium. Prediction of the behavior of such systems depends on knowing the limiting equilibrium behavior but also on kinetic factors. While the rate constants of isolated kinetic processes such as thermal diffusion, chemical diffusion in solids and melts, crystal dissolution, crystal nucleation, and crystal growth have been extensively studied, a disequilibrium melting process in a multicomponent system involves all of these processes operating together, and it is not obvious which is the rate-limiting process.

Studies of zoning patterns in igneous systems as a means to understand formation and alteration conditions date back to optical microscope observations in the 1930s (Homma 1935; Phemister 1934), with some of the most evident examples found in plagioclase crystals due to their relatively large size. Improvement of analytical techniques over the following decades (*e.g.*, SIMS, EPMA) allowed for higher spatial resolution measurement of composition profiles associated with zoning, providing additional insight. Now, it is widely believed that different zoning patterns (*e.g.*, normal, reverse, oscillatory, patchy) may indicate various

disequilibrium conditions, driving our need to better understand phase change kinetics.

The kinetics of crystallization are more frequently studied than those of melting, in part because they are more easily preserved—crystals capture a chemical record as they grow. Additionally, there is an extensive history of materials science literature (Cabane, Laporte, and Provost 2005; Jackson 1984, 2010; Karato 1989; Nancollas and Purdie 1964; Nielsen and Toft 1984) on crystallization due to its relevance to material synthesis applications. The kinetics of melting are less understood. There has been exploration of the analogous process of crystal dissolution in melts, in which a solid is placed in a (usually large volume of) melt in which it is undersaturated and allowed to dissolve into the melt (usually under isothermal conditions) (Chen and Zhang 2008; Liang 1999, 2000, 2003; Morgan and Liang 2003; Tsuchiyama 1985, 1986; Zhang, Walker, and Lesher 1989). Examination of crystal dissolution in melts constrains factors relevant to melting, such as how the relative rates of interface reaction, melt phase transport, and solid state diffusion affect the final chemical composition in the phases that are present. However, several aspects of melting are not captured by dissolution experiments. First, the melt-crystal assemblage in most dissolution experiments begins out of equilibrium, with the expectation that they converge toward equilibrium over time. In contrast, during melting experiments, there is only one solid phase initially, which is expected to be homogenous and in equilibrium. As the sample is heated, the nucleation and growth of melt then creates gradients that may, if unrelaxed, lead to disequilibrium conditions. Melting takes place under changing temperature conditions, with possible modulation of chemical potential gradients by latent and sensible heat transport. Second, most dissolution problems assume equilibrium of the major elements at the melt-crystal boundary. However, during melting, especially at rapid rates, this is an unproven assumption, and we suggest it is important to consider relaxation of this constraint. The geometries of dissolution and melting processes may also be quite different. These considerations, unique to melting,

warrant experiments that specifically capture such behaviors in order to properly observe and quantify them.

Melting is an important process across numerous geologic settings, including decompression melting in the mantle, flux melting in subduction zones, lower crustal melting in orogens, and impact melting. In each case, the rates of melt production may exceed the rates necessary to maintain strict equilibrium. Therefore, we aim to contribute to this body of knowledge by performing experiments that provide fundamental information about melting kinetics. Existing literature provides some insight on superheating of one-component systems using a combination of experiments and simulations (Luo et al. 2003; Luo and Ahrens 2004; Mei and Lu 2007; Wunderlich 2007). Historically, studies of two-component systems are less common, with the focus primarily on metal alloys. Given the multicomponent compositions of igneous rocks, there is certainly a need to push these boundaries in order to accurately describe melting kinetics in natural samples; this work provides a critical step in that direction by investigating a common two-component igneous mineral series, plagioclase. Our selected set of parameters gives a comprehensive framework for observing the melting behavior, textures, and compositional profiles of plagioclase, which can be extended in future work to other relevant igneous systems, such as olivine or K-feldspar, bringing us closer to understanding multicomponent systems. We performed long-timescale experiments that approached equilibrium behavior, which acted as a baseline with which to interpret the results of faster experiments where kinetic constraints come into play. Then, by performing heating rate experiments spanning several orders of magnitude with target temperatures ranging from subsolidus to superliquidus, we sought to elucidate melting dynamics in igneous systems where the equilibrium assumptions progressively fail. The goal is to provide both qualitative descriptions of disequilibrium melting phenomena at various rates and quantitative targets for the development of models that account simultaneously for the multiple kinetic processes occurring during rapid melting of multicomponent systems.

Methods

Sample Selection and Preparation

Gem-quality plagioclase was selected from a set of tumbled single crystals of labradorite mined from northern Chihuahua, Mexico. The source may be the Dorado Mine in Casas Grandes but the provenance is not completely certain. The single crystals were visually transparent, ranging from 1.5-2 cm in the longest dimension and a minimum of 7 mm in their shortest dimension for coring purposes. Crystals were polished to form an optically transparent plane parallel to the longest dimension. Initial composition determination was performed using energy-dispersive X-ray spectroscopy (EDS) on a ZEISS 1550VP Field Emission SEM, to confirm similarity of labradorite composition among the selected crystals. Using point analysis, all crystals were determined to be homogeneous and compositionally similar, with 58±2 mol% An. No exsolution phenomena such as Bøggild or Huttonlocher lamellae were found. This information was used to determine appropriate target temperatures according to the 1 atm. phase diagram of Bowen (1913), which gives a solidus temperature of 1330 °C and a liquidus temperature of 1470 °C for this composition. Let $\phi' \equiv (\phi - \phi_{solidus})/(\phi_{liquidus} - \phi_{solidus})$. We ran experiments subsolidus (1300 °C), at ϕ' = 0.25 (1365 °C), 0.50 (1400 °C), and 0.75 (1435 °C), and superliquidus (1490 °C).

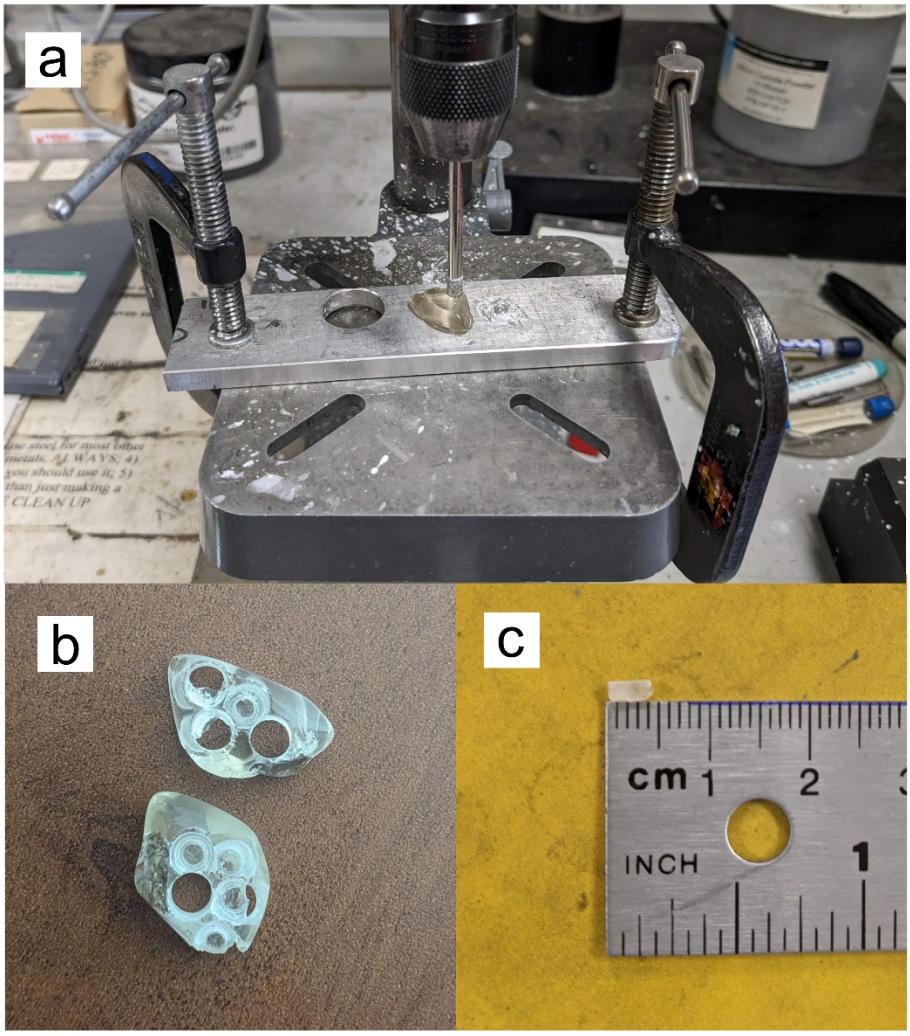

Figure 2.1. *Crystal coring procedure.* (a) Coring single crystal with diamond drill bit, (b) single crystals with several cores removed from each, and (c) one plagioclase core measuring ~4 mm.

Five single crystals were cored using a 4 mm OD diamond drill bit to obtain as many identical cores from each crystal as possible (Figure 2.1ab). All cylindrical cores were 3-4 mm in length and approximately 2.11 mm in diameter (Figure 2.1c). Samples are numbered X-Y, where X is a given single crystal, and Y denotes the core number drilled from the crystal. See Table 2.1 for each experimental condition and the corresponding sample number. Samples were inserted into cylindrical Pt

buckets of 2.41 mm OD and 0.15 mm wall thickness, ensuring the surface of the sample was flush with the wall of the bucket.

(a)	**Dwell Time at 1400 °C (** ϕ' = 0.50**)**	**Sample #**
	10^1 min	4-1
	10^2 min	4-2
	10^3 min	4-3
	10^4 min	4-4

(b)		**Heating Rate**			
		15 °C/hr with intermittent holds	**10 °C/hr**	**100 °C/hr**	**1000 °C/hr**
Target Temperature	**1300 °C** (Subsolidus)	3-1	4-5	--	5-1
	1365 °C (ϕ' = 0.25)	3-3	1-1	2-2	5-2
	1400 °C (ϕ' = 0.50)	--	1-2	2-3	5-3
	1435 °C (ϕ' = 0.75)	3-2	4-6	2-4	5-4
	1490 °C (Superliquidus)	--	1-4	2-5	5-5

Table 2.1. *Experimental samples.* A matrix of experimental conditions is provided with the corresponding sample numbers. Samples are numbered X-Y, where X is a given single crystal, and Y denotes the core number drilled from the crystal. When possible, cores drilled from the same single crystal were used for the heating rate $\phi' \equiv (\phi - \phi_{solidus})/(\phi_{liquidus} - \phi_{solidus})$. (a) Equilibrium experiments. Samples were held at 1400 °C at several time intervals. (b) Heating/kinetic experiments. Intermittent holds for the 15 °C/hr ramp ranged from 64-72 h.

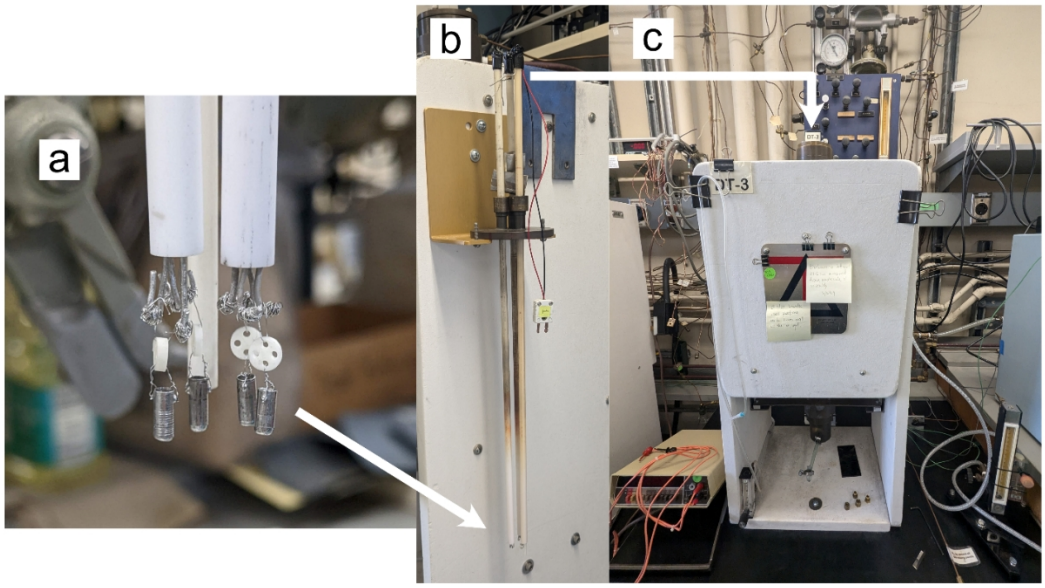

Figure 2.2. *Gas-mixing furnace experimental setup.* (a) Pt capsules containing cylindrical plagioclase cores suspended using thin Pt wire, (b) hollow alumina rods containing conductive Pt wire for hanging samples, and (c) gas-mixing furnace.

Experimental Procedures

All experiments were completed in a 1-atm Deltech vertical gas-mixing furnace, in flowing air (Figure 2.2c). The Pt buckets containing the samples were suspended in the furnace hotspot using hollow alumina rods bearing conductive 0.76 mm Pt wires with hooked ends (Figure 2.2b). Buckets were hung on the hooks using 0.127 mm Pt wire (Figure 2.2a). A B-type thermocouple was suspended alongside the samples for real-time reading of the hotspot temperature. The hotspot thermocouple was regularly calibrated to the melting point of gold for accuracy. For heating experiments, between one and four samples were lowered together into the hotspot and homogenized at the selected subsolidus temperature, 1300 °C, for 12-24 h. Samples were then heated at various linear heating rates using a programmed Eurotherm controller monitoring a separate B-type thermocouple near the furnace heating elements. When the hotspot thermocouple reached a target temperature, one of the samples was drop-quenched into water using a DC electrical source to burn through the 0.127 mm Pt wire. Equilibrium experiments closely follow the methods

of Tsuchiyama & Takahashi (1983). Sample were homogenized at 1300 °C for 24 h and subjected to a rapid 1000 °C/hr ramp rate to reach the target temperature of 1400 °C. After the target temperature was achieved, samples were held isothermally and drop-quenched after the appropriate amount of time. Experimental conditions for each suite of samples are shown in Table 2.1.

Sample Analysis

Each sample, contained within its Pt bucket, was mounted in petropoxy 154 (Burnham Petrographics, LLC) and cut to expose a circular cross-section. The sample surface was polished with increasingly fine sandpaper, from 150 μm down to 1 μm, until an optical mirror finish was achieved, then cleaned with ethanol and carbon coated (20 nm thickness). Samples and standards were analyzed by wavelength-dispersive X-ray spectroscopy (WDS) on a JEOL JXA-iHP200F Field Emission EPMA. A 90000 μm^2 area of each cross section was mapped for major element concentrations of Si, Ti, K, Na, Fe, Al, Ca, and Mg (expressed as weight percent oxides assuming all Fe as FeO). Standards were synthetic anorthite for Si, Al, and Ca; synthetic forsterite for Mg; synthetic rutile for Ti; synthetic fayalite for Fe; natural Amelia albite for Na; and natural Asbestos microcline for K. Regions were manually selected to avoid surface contaminants, polishing defects, and fractures (which likely resulted from the temperature shock of the drop-quench). The electron beam, focused to 0.1 μm diameter, had a 15 kV accelerating voltage, 20 nA beam current. Maps were generated with 0.5 μm step size and 75 ms dwell time at each point. For samples 3-1, 3-2, and 3-3, time-dependent intensity (TDI) calibrations were utilized for each area scan due to glass sensitivity to Na diffusion during measurement. Background subtraction used the Mean Atomic Number method, calibrated for each element using all standards from which that element is absent. Matrix correction used the CITZAF routine as implemented in the Probe for EPMA software.

Image Analysis

Backscattered electron (BSE) images and WDS chemical maps of Ca and Na in each sample were analyzed to define the distribution of glass and crystalline phases and their compositional patterns. Processing was performed in MATLAB's Image Segmenter application: an appropriate global threshold was determined for each image, implementing Otsu's method to output a mask distinguishing between crystal and melt regions. Global threshold masks were then refined using image convolution to remove artificial signatures (*i.e.*, to reduce noise, melt pools were not characterized as such unless the identified region surpassed a threshold number of adjacent pixels). Refined masks were compared across BSE and WDS images for a given sample to confirm their accuracy and consistency in identifying melt vs. crystal regions, regardless of which map type was used to generate them. The refined masks were then used to classify crystal vs. melt regions of each image and calculate relevant parameters for characterization (Tables 2.2-2.8).

Melt pools were manually selected for compositional line profile analysis. They were chosen with three factors in mind: (1) The melt pool must be generally circular, (2) it should not be too close to another visible melt pool (so as to minimize confounding factors when interpreting diffusion kinetics), and (3) the minimum dimension of the melt pool needs to be 6 μm in order to capture the diffusion profile. Given the analytical limitation that every pixel represents a 0.5 μm step size, the lower bound was set in order for there to be a sufficient number of data points for analysis on either side of the melt-crystal boundary. Samples 4-4, 3-3, and 1-2 fulfilled the aforementioned criteria for compositional line profile analysis. A rectangular region of interest (ROI) was drawn around each melt pool, and its centroid was identified. Line profiles were then drawn from the centroid to every edge pixel of the ROI (Figure 2.7). This generated a set of line profiles of varying lengths that were aligned at the melt-crystal boundary and overlaid (Figure 2.8). The profiles were then averaged to capture the diffusion behavior surrounding a given melt pool (Figures 2.9-2.10). Data points from several melt pools were combined to obtain an average diffusion profile for the given sample (Figure 2.11).

Results

Textural Evolution

Clear trends in textural evolution can be seen in the BSE images of both the equilibrium and heating rate experimental suites (Figure 2.3). Variations in characteristics such as melt fraction, melt pool size distribution, melt pool shape, melt pool preferred orientation, and melt pool connectivity are qualitatively evident to the eye. Several parameters were calculated to quantitatively describe these trends in the analyzed regions: percentage of melt by area (Table 2.2), melt pool density per unit area (Table 2.4), and the dimensionless shape factor $(\text{melt pool perimeter})^2/\text{melt pool area}$ (Table 2.5). The minimum possible value of the dimensionless shape parameter would be 4π, or 12.57, representing a perfect circle; more elongated or irregularly shaped melt pools, yield larger values.

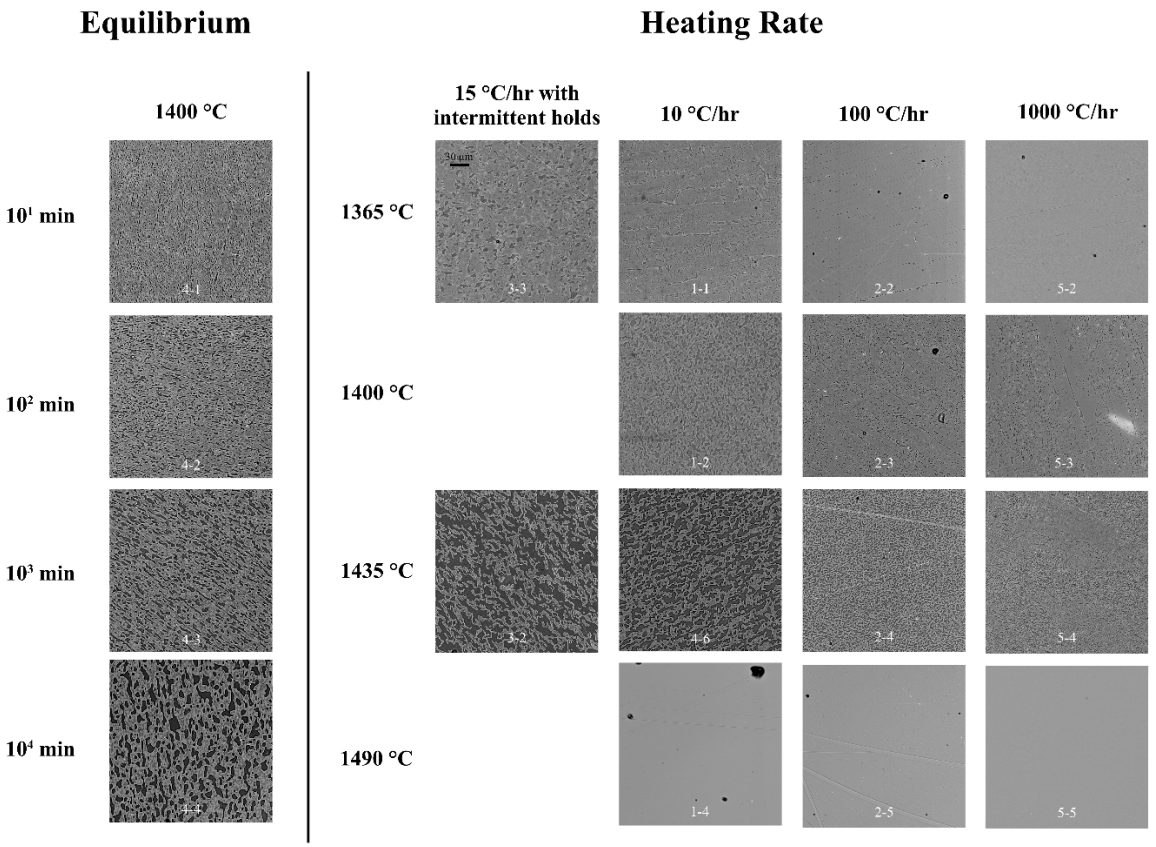

Figure 2.3. *BSE images of all samples.* The first column shows the time series of isothermal experiments at 1400 °C. The other columns correspond to the layout of Table 1, except that subsolidus experiments are not shown. Each image displays a 300 µm x 300 µm area of the sample. Darker regions in the images are melt pools, while lighter regions are crystal.

The equilibrium experiments were performed to establish the baseline behavior of melting with which to compare the results of the heating rate experiments. While holding samples at 1400 °C, melt formed rapidly with a sieve-like texture within the first ten minutes, consisting largely of elongated melt pools ("rods") of ~1-2 μm width and small circular melt pools with diameters of ~1-2 μm. The long axes of the rods demonstrated a clear preferred orientation in the samples quenched from 10^1-10^3 minutes, indicating diffusion anisotropy. This behavior is consistent with observations of Tsuchiyama & Takahashi (1983), who noted that the long axes of the rods in their equilibrium experiments were nearly parallel to [010] or [001] crystallographic orientations. From 10^1-10^3 min, these rods grew in width, from ~1-2 μm to > 5μm, and the number of small circular melt pools decreased. Then, a visible transition in melt geometry occurred from 10^3 to 10^4 minutes, in which the majority of the melt pools changed from elongated rods to more circular shapes, and a preferred orientation is no longer visible. Overall, the equilibrium experiments showed a monotonic increase in melt percentage by area as dwell time increased, as expected. The number of melt pools per area monotonically decreased, quantitatively describing merging of small melt pools into larger ones. However, the melt pool shape factor exhibits a complex behavior with time; although "rounding-out" of each initially rod-shaped pool decreases this factor, mergers of adjacent melt pools create temporarily complex compound pool shapes that yield a (likely transient) tendency to increase this factor.

The heating rate experiments add another layer of complexity. At a given heating rate, samples quenched at increasing temperatures had progressively higher percent melt per area, as expected. Additionally, the percent difference from expected melt proportion at equilibrium generally decreased with increasing temperature for a given heating rate. Regardless of heating rate, each sample quenched at superliquidus temperature was 100% melt, even though their counterparts had vastly different melt fractions at ⬚ = 0.75. This is consistent with ultrafast dynamic experiments (*e.g.*, planar shock-wave loading and laser heating) in existing literature, which found that

solid crystals can survive beyond the equilibrium melting point, but only at rates significantly faster (>10^6 °C/hr) than those applied here (Luo et al. 2003; Macris et al. 2018). For samples quenched at a given temperature between the solidus and liquids, an increase in heating rate resulted in a decrease of percent melt by area. With each order-of-magnitude increase in heating rate, the percent melt deviated further from expected equilibrium behavior. Generally, we see a common evolution of texture with time: melt pools initially form with an elongated geometry and a preferred orientation and mature into more circular shapes. The competing effects of increasing temperature and increasing time trade off to yield somewhat unpredictable trends in melt pool density and shape factor; nucleation of new melt pools, merging of melt pools, and rounding of melt pools all compete to influence these parameters. We must note that samples quenched at different temperatures and different heating rates can have similar patterns, because the effects of temperature and time trade off against one another. For example, the melt pool geometries in 3-3, 1-2, and 2-4 are similar despite a range of 70 °C in final temperature and an order of magnitude in heating rate. Evaluated alone, it would be difficult to discern their melting paths, but they could be differentiated by the length scale of the melt pools (decreasing as heating rate increases) and the density of melt pools (increasing along with heating rate). This example indicates that multiple textural characteristics must be considered to effectively constrain the melting path of a given sample.

(a)	**Dwell Time at 1400 °C (𝜙'= 0.50)**	**% Melt by Area**
	10^1 min	17.02
	10^2 min	21.87
	10^3 min	28.81
	10^4 min	33.04
	Equilibrium (Bowen 1913)	33.1

(b)			**Heating Rate**			
		Equilibrium (Bowen 1913)	**15 °C/hr with intermittent holds**	**10 °C/hr**	**100 °C/hr**	**1000 °C/hr**
Target Temperature	**1300 °C** (Subsolidus)	0	0	0	--	0
	1365 °C (𝜙'= 0.25)	14.1	11.67	11.06	4.08	1.59
	1400 °C (𝜙'= 0.50)	33.1	--	25.52	11.23	11.98
	1435 °C (𝜙'= 0.75)	55.3	55.09	47.43	34.88	23.52
	1490 °C (Superliquidus)	100	--	100	100	100

Table 2.2. *Percent melt by area.* (a) Equilibrium experiments and (b) heating experiments.

(a)	**Dwell Time at 1400 °C (**ϕ'= 0.50**)**	
	10^1 min	-48.5%
	10^2 min	-33.3%
	10^3 min	-12.1%
	10^4 min	0.0%

(b)		**Heating Rate**			
		15 °C/hr with intermittent holds	**10 °C/hr**	**100 °C/hr**	**1000 °C/hr**
Target Temperature	**1365 °C** (ϕ'= 0.25)	-16.6%	-21.0%	-70.9%	-88.6%
	1400 °C (ϕ'= 0.50)	--	-22.7%	-66.0%	-63.7%
	1435 °C (ϕ'= 0.75)	-0.4%	-14.2%	-36.9%	-57.5%

Table 2.3. *Percent difference from expected melt proportion at equilibrium.* (a) Equilibrium experiments and (b) heating experiments. Subsolidus and superliquidus experiments are not listed.

(a)	**Dwell Time at 1400 °C (ϕ = 0.50)**	
	10^1 min	0.0188
	10^2 min	0.0128
	10^3 min	0.0084
	10^4 min	0.0048

(b)		**Heating Rate**			
		15 °C/hr with intermittent holds	**10 °C/hr**	**100 °C/hr**	**1000 °C/hr**
Target Temperature	**1365 °C** (ϕ = 0.25)	0.0051	0.0084	0.0048	0.000072
	1400 °C (ϕ = 0.50)	--	0.0108	0.0124	0.0116
	1435 °C (ϕ = 0.75)	0.0031	0.0044	0.0176	0.0132

Table 2.4. *Melt pool density.* Number of melt pools per area in units of μm^{-2}. Subsolidus and superliquidus experiments are not listed.

(a)	**Dwell Time at 1400 °C (**Φ'= 0.50**)**	
	10^1 min	17.51
	10^2 min	18.88
	10^3 min	19.91
	10^4 min	17.04

(b)		**Heating Rate**			
		15 °C/hr with intermittent holds	**10 °C/hr**	**100 °C/hr**	**1000 °C/hr**
Target Temperature	**1365 °C** (Φ'= 0.25)	14.23	17.79	63.30	62.13
	1400 °C (Φ'= 0.50)	--	17.46	16.34	22.17
	1435 °C (Φ'= 0.75)	29.55	28.82	22.16	29.98

Table 2.5. *Dimensionless shape factor: mean value of melt pool perimeter^2/area of melt pool.* Subsolidus and superliquidus experiments are not listed.

Chemical Composition - Bulk

Within error, the bulk compositions of the samples remain constant throughout the experiments, as measured by integrating the complete quantitative map images (Table 2.6). The highest temperature superliquidus experiments may have experienced some Na volatilization, but this may also reflect Na loss from the analytical volume during measurement.

In the equilibrium experiments, the residual crystal composition became more calcic with time, moving toward anorthite, while the melt composition becomes more sodic (Table 2.7a). This behavior cannot be predicted by the equilibrium phase diagram, which at constant temperature suggests both compositions should be constant and with variable temperature suggests both should evolve in the same direction in composition space. At 10^4 minutes, the sample almost but not quite reaches the equilibrium solidus and liquidus compositions for bulk composition An60, according to Bowen (1913). For all samples, the crystal composition remains consistent with binary albite-anorthite solid solution plagioclase stoichiometry, while the melt tends to deviate slightly from the binary. Using the lever rule, we can calculate the percent deviation from expected equilibrium compositions within each phase (Table 2.8). In the melt, sodium is consistently depleted and calcium is consistently elevated relative to equilibrium composition, and the crystal experiences the inverse of this trend.

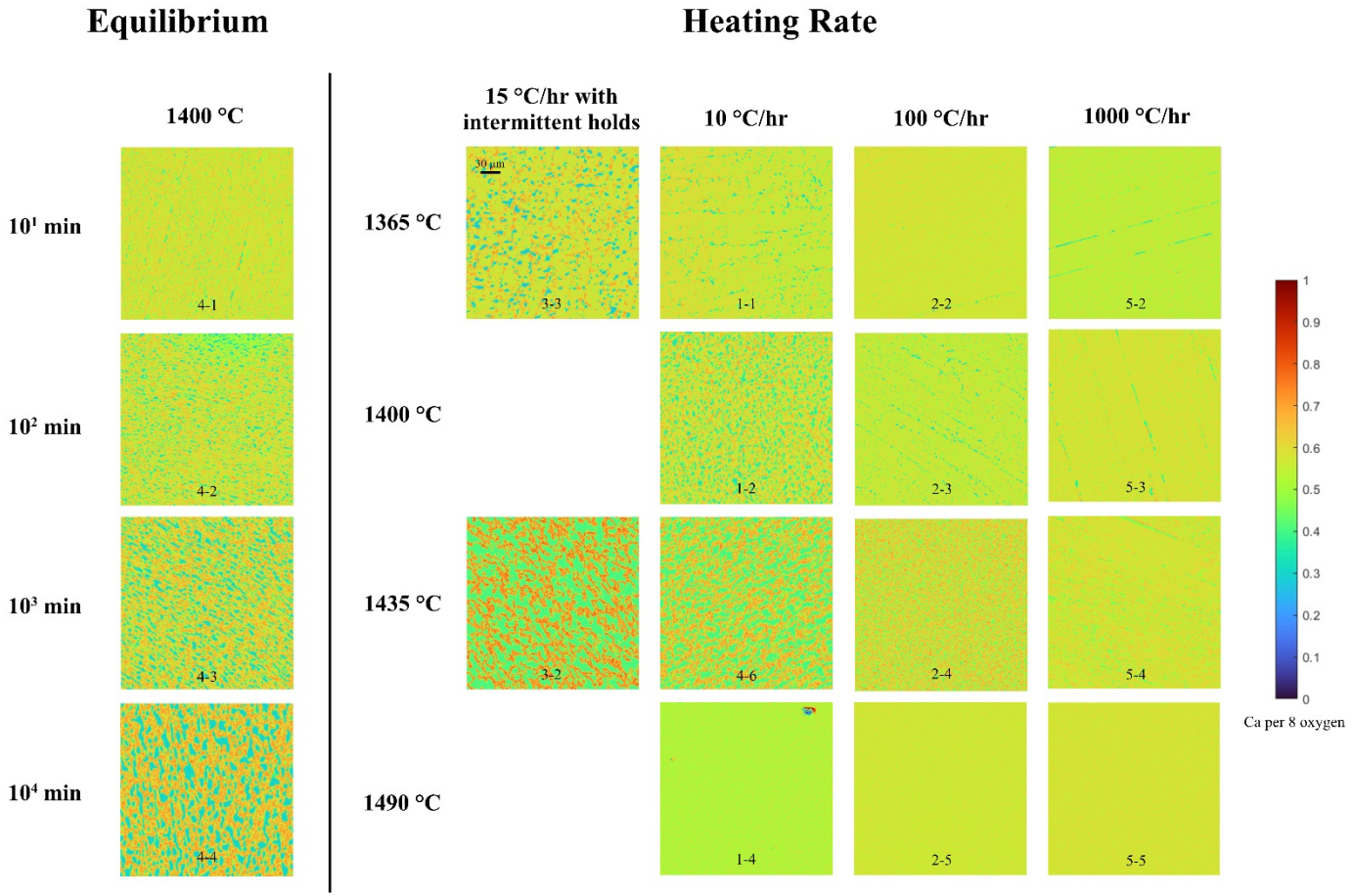

Figure 2.4. *Calcium per 8 oxygens.* Corresponding to the layout of Figure 2.3, the spatial distribution of calcium composition for each sample is plotted. The corresponding data is listed in Table 2.7.

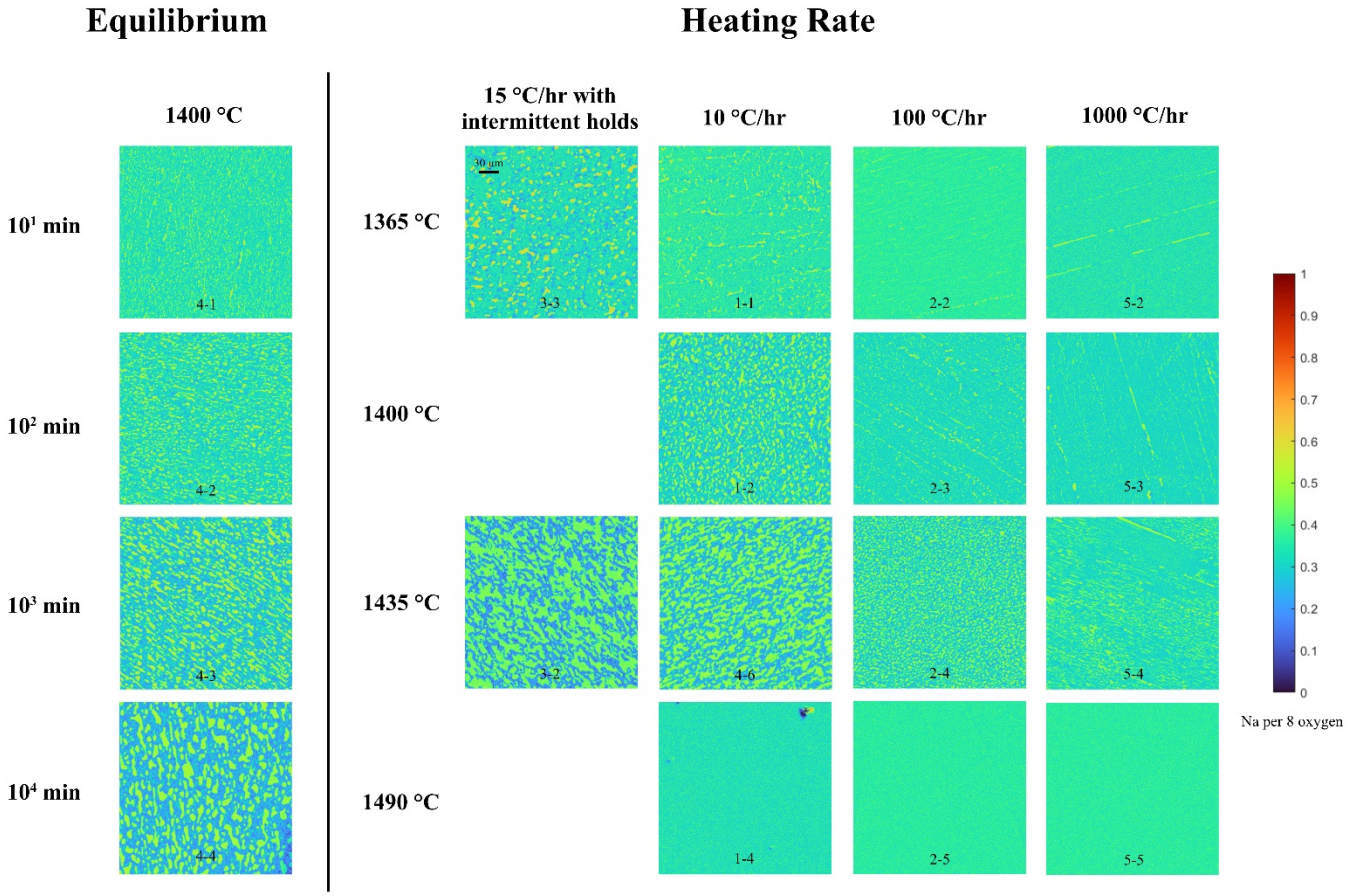

Figure 2.5. *Sodium per 8 oxygens.* Corresponding to the layout of Figure 2.3, the spatial distribution of sodium composition for each sample is plotted. The corresponding data is listed in Table 2.7.

Dwell Time at 1400 °C (𝑓O2' = 0.50)	
10^1 min	Ca: 0.5960 Na: 0.3992
10^2 min	Ca: 0.5964 Na: 0.3970
10^3 min	Ca: 0.5953 Na: 0.3916
10^4 min	Ca: 0.5920 Na: 0.3697

(b)		**Heating Rate**			
		15 °C/hr with intermittent holds	**10 °C/hr**	**100 °C/hr**	**1000 °C/hr**
Target Temperature	**1300 °C** (Subsolidus)	Ca: 0.6020 Na: 0.3879	Ca: 0.6033 Na: 0.4093	--	Ca: 0.6048 Na: 0.3920
	1365 °C (𝑓O2' = 0.25)	Ca: 0.6051 Na: 0.3918	Ca: 0.6068 Na: 0.4073	Ca: 0.6001 Na: 0.3916	Ca: 0.5972 Na: 0.3925
	1400 °C (𝑓O2' = 0.50)	--	Ca: 0.5943 Na: 0.3922	Ca: 0.5955 Na: 0.3810	Ca: 0.6012 Na: 0.3734
	1435 °C (𝑓O2' = 0.75)	Ca: 0.6074 Na: 0.3813	Ca: 0.5961 Na: 0.4014	Ca: 0.6010 Na: 0.3940	Ca: 0.5977 Na: 0.3916
	1490 °C (Superliquidus)	--	Ca: 0.5876 Na: 0.3857	Ca: 0.5959 Na: 0.3862	Ca: 0.6039 Na: 0.3880

Table 2.6. *Calcium and sodium atoms per 8 oxygen formula unit, integrated over total analyzed area*. Blue text = Ca, red text = Na. Note that the consistently lower mole fraction of Na measured in the glassy superliquidus samples is likely due to loss from beam diffusion during measurement. (a) Equilibrium and (b) heating/kinetic experiments.

(a)	**Dwell Time at 1400 °C (**ϕ' = 0.50**)**		
	10^1 min	Ca: 0.4933 Na: 0.4694	Ca: 0.6171 Na: 0.3848
	10^2 min	Ca: 0.4526 Na: 0.5123	Ca: 0.6366 Na: 0.3647
	10^3 min	Ca: 0.4222 Na: 0.5438	Ca: 0.6654 Na: 0.3300
	10^4 min	Ca: 0.3942 Na: 0.5229	Ca: 0.6895 Na: 0.2942
	Equilibrium (Bowen 1913)	Ca: 0.36 Na: 0.64	Ca: 0.72 Na: 0.28

Table continued on next page.

(b)				Heating Rate							
		Equilibrium (Bowen 1913)		15 °C/hr with intermittent holds		10 °C/hr		100 °C/hr		1000 °C/hr	
Target Temperature	1365 °C (F = 0.25)	Ca: 0.27 Na: 0.73	Ca: 0.66 Na: 0.34	Ca: 0.3712 Na: 0.5723	Ca: 0.6360 Na: 0.3679	Ca: 0.4815 Na: 0.4301	Ca: 0.6224 Na: 0.4044	Ca: 0.6006 Na: 0.3898	Ca: 0.5877 Na: 0.4354	Ca: 0.4738 Na: 0.5012	Ca: 0.5990 Na: 0.3910
	1400 °C (F = 0.50)	Ca: 0.36 Na: 0.64	Ca: 0.72 Na: 0.28	--	--	Ca: 0.4498 Na: 0.5158	Ca: 0.6438 Na: 0.3499	Ca: 0.4864 Na: 0.4707	Ca: 0.6093 Na: 0.3697	Ca: 0.5359 Na: 0.4207	Ca: 0.6101 Na: 0.3670
	1435 °C (F = 0.75)	Ca: 0.45 Na: 0.55	Ca: 0.78 Na: 0.22	Ca: 0.4892 Na: 0.4834	Ca: 0.7525 Na: 0.2561	Ca: 0.4864 Na: 0.5032	Ca: 0.6951 Na: 0.3095	Ca: 0.4971 Na: 0.4900	Ca: 0.6566 Na: 0.3426	Ca: 0.5254 Na: 0.4641	Ca: 0.6200 Na: 0.3694

Table 2.7. *Calcium and sodium atoms per eight oxygen formula unit in melt- and crystal-identified regions.* Red background = melt, blue background = crystal, blue text = Ca, red text = Na. Figures 2.4-2.6 provide visualization of this data. (a) Equilibrium and (b) heating/kinetic experiments.

(a)	**Dwell Time at 1400 °C (** = 0.50**)**		
	10^1 min	Ca: 37.0% Na: -26.7%	Ca: -14.3% Na: 37.4%
	10^2 min	Ca: 25.7% Na: -20.0%	Ca: -11.6% Na: 30.25%
	10^3 min	Ca: 17.3% Na: -15.0%	Ca: -7.6% Na: 17.9%
	10^4 min	Ca: 9.5% Na: -18.3%	Ca: -4.2% Na: 5.1%

Table continued on next page.

(b)		Heating Rate							
		15 °C/hr with intermittent holds		10 °C/hr		100 °C/hr		1000 °C/hr	
Target Temperature	**1365 °C** (𝑓𝑂2 = 0.25)	Ca: 37.5% Na: -21.6%	Ca: -3.6% Na: 8.2%	Ca: 78.3% Na: -41.1%	Ca: -5.7% Na: 18.9%	Ca: 22.4% Na: -46.6%	Ca: -11.0% Na: 28.1%	Ca: 75.5% Na: -31.3%	Ca: -9.2% Na: 15%
	1400 °C (𝑓𝑂2 = 0.50)	--	--	Ca: 24.9% Na: -19.4%	Ca: -10.6% Na: 25.0%	Ca: 35.1% Na: -26.5%	Ca: -15.4% Na: 32.0%	Ca: 48.9% Na: -34.3%	Ca: -15.3% Na: 31.1%
	1435 °C (𝑓𝑂2 = 0.75)	Ca: 8.7% Na: -12.1%	Ca: -3.5% Na: 16.4%	Ca: 8.1% Na: -8.5%	Ca: -10.9% Na: 40.1%	Ca: 10.5% Na: -10.9%	Ca: -15.8% Na: 55.7%	Ca: 16.8% Na: -15.6%	Ca: -20.5% Na: 67.9%

Table 2.8. *Percent difference from equilibrium composition: calcium and sodium atoms per eight oxygen formula unit in melt- and crystal-identified regions.* Red background = melt, blue background = crystal, blue text = Ca, red text = Na. (a) Equilibrium and (b) heating/kinetic experiments.

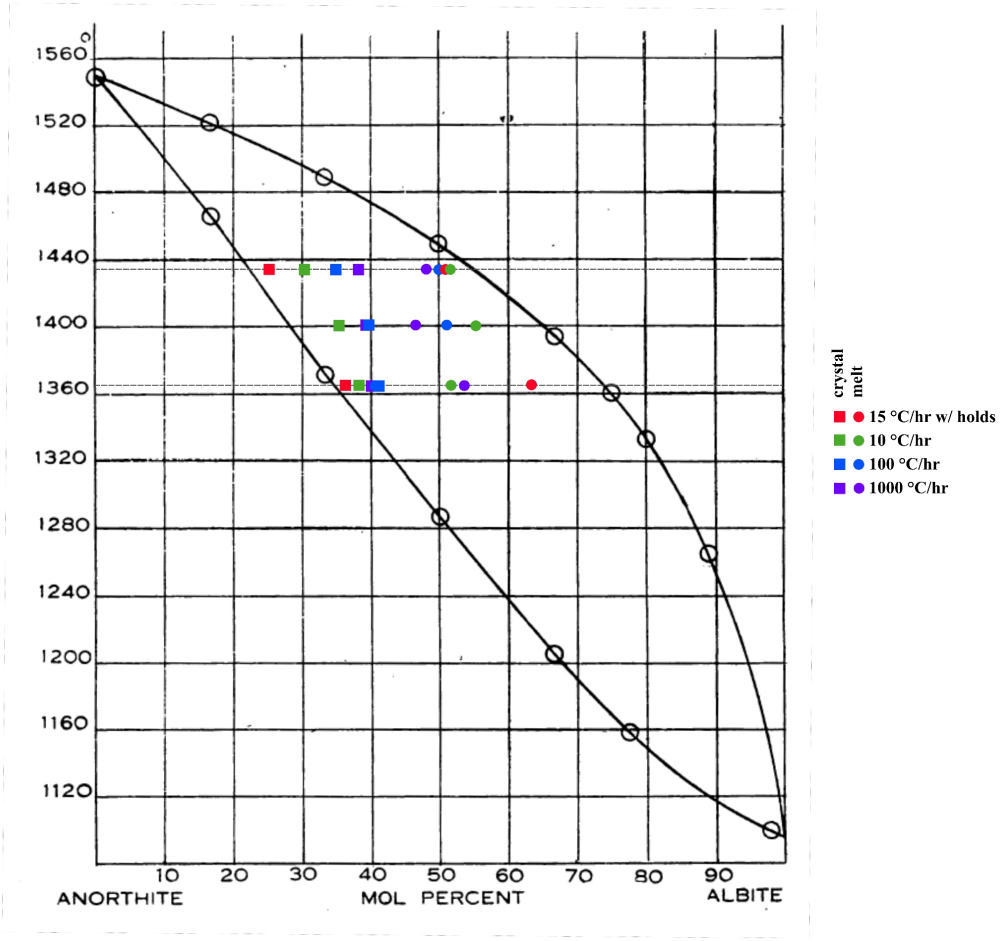

Figure 2.6. *Compositional deviation from equilibrium partitioning.* Ca contents per eight oxygen formula unit basis are used to estimate mol percent albite in each sample and plotted on the plagioclase equilibrium phase diagram. Crystal compositions are marked by squares and melt by circles. Modified from Bowen (1913).

Chemical Composition – Line Profiles

Diffusion of the major elements Ca and Na within and between melt and crystal phases generated interesting compositional profiles under different experimental conditions. Comparison of individual melt pool diffusion profiles (Figures 2.9 and 2.10) shows the various length scales for diffusion in the different samples: for 4-4, profiles extend 6 μm from either side of the phase boundary, 4 μm for 3-3, and 3 μm for 1-2. For all three samples analyzed, the standard deviation of

Ca content in the melt is smaller than that in the solid. Interestingly, this is not true for Na – the standard deviation of Na in the melt and solid are comparable. Looking at sample 4-4, the average diffusion profiles for both Ca and Na appear to be perfectly sigmoidal, with clear plateaus in composition starting ~1-2 μm away from the melt-crystal boundary in both phases. This acts as our simplest base case, which is what we may expect to see at equilibrium. Adding a layer of complexity, in sample 3-3, which experienced a slow heating rate and intermittent hold, we see that while the general profile is still sigmoidal, the composition on either side of the phase boundary does not plateau in the same way as the equilibrium sample. Ca in the crystal appears higher on average closer to the phase boundary and decreases slightly moving away from it. It is possible that this short-range profile reflects the net diffusion of Ca from melt to crystal, considering the depletion of Ca in the crystal phase relative to equilibrium composition. We see the reverse being true for Na, such that Na in the melt is higher near the phase boundary. For samples 3-3 and 1-2, the profile traversing the melt-crystal boundary is significantly less sharp than that of sample 4-4. The deviations at the right end of each profile may be due to the influence of other nearby melt pools and their respective diffusion processes. The stacked diffusion profiles show that the interaction between the moving phase boundary and the chemical kinetics generates behavior that deviates from equilibrium, to be further explored in Chapter 3.

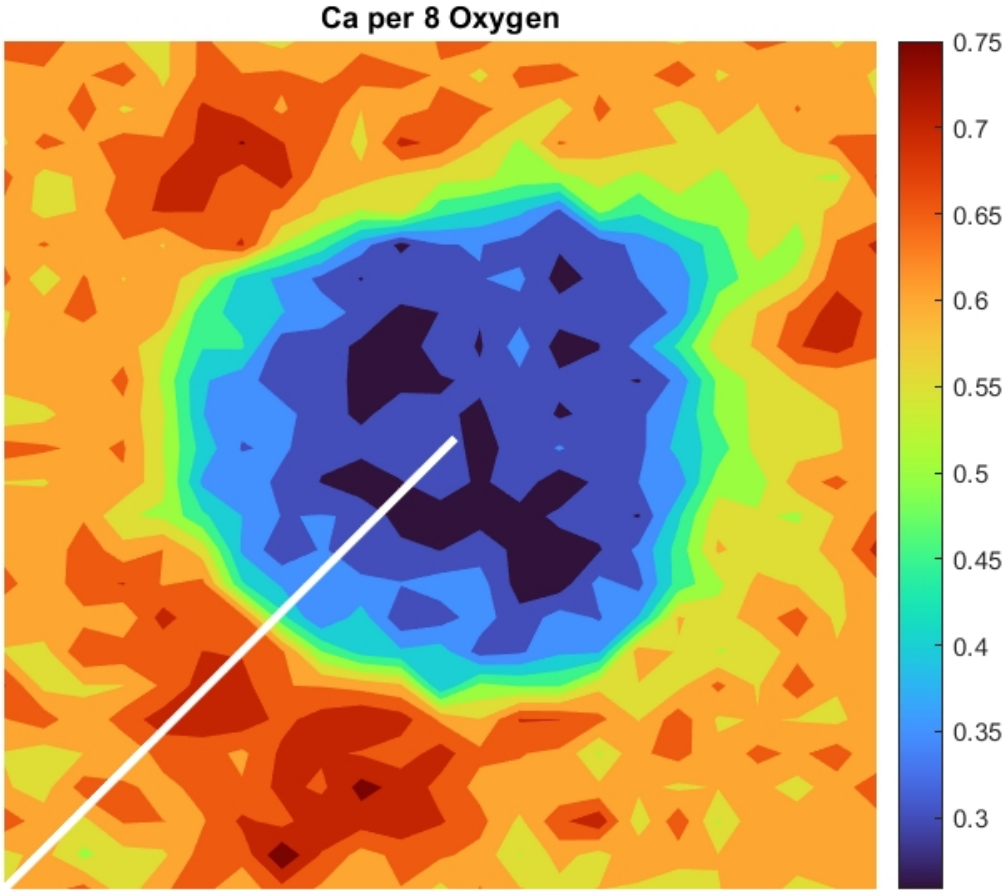

Figure 2.7. *Example line profile across melt-crystal boundary.* The colors show a contour plot of gridded electron probe analyses for Ca cations per eight oxygens. Line profiles (white) were drawn from the centroid of the melt pool area to every edge pixel of the manually selected ROI. This generated a large data set of line profiles that were averaged to capture the diffusion behavior surrounding a given melt pool.

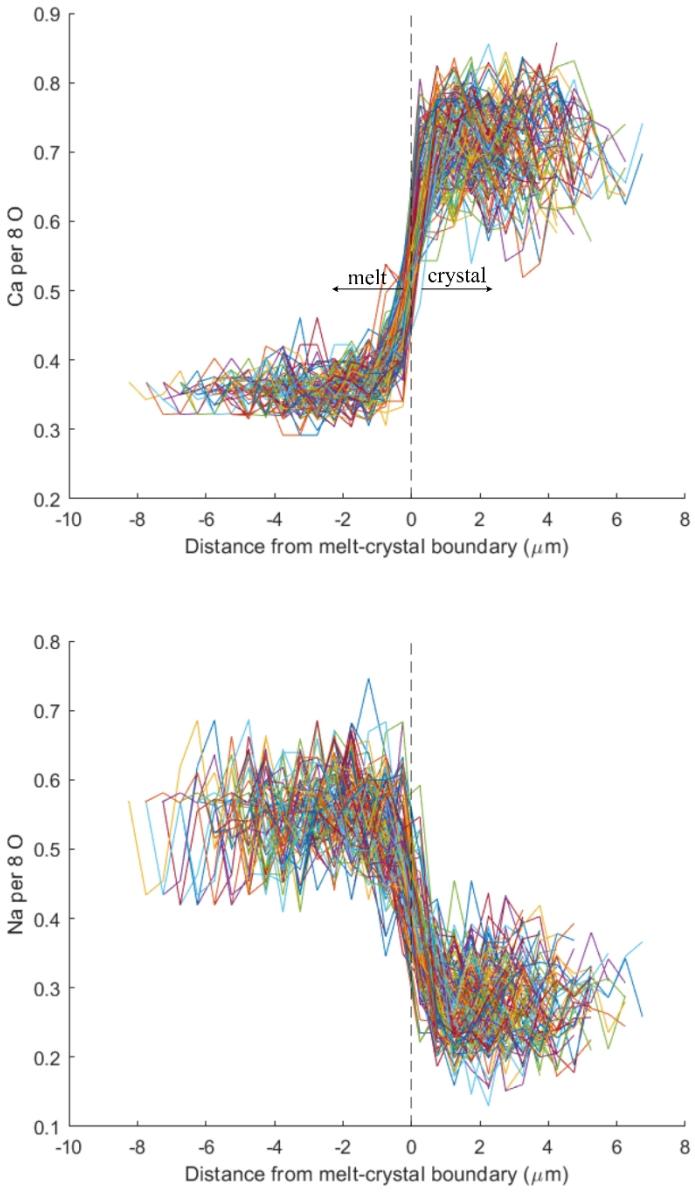

Figure 2.8. *Line profiles across melt pool #1 from sample 4-4.* Each color represents a different line profile, aligned such that the melt-crystal boundary is situated at x = 0.

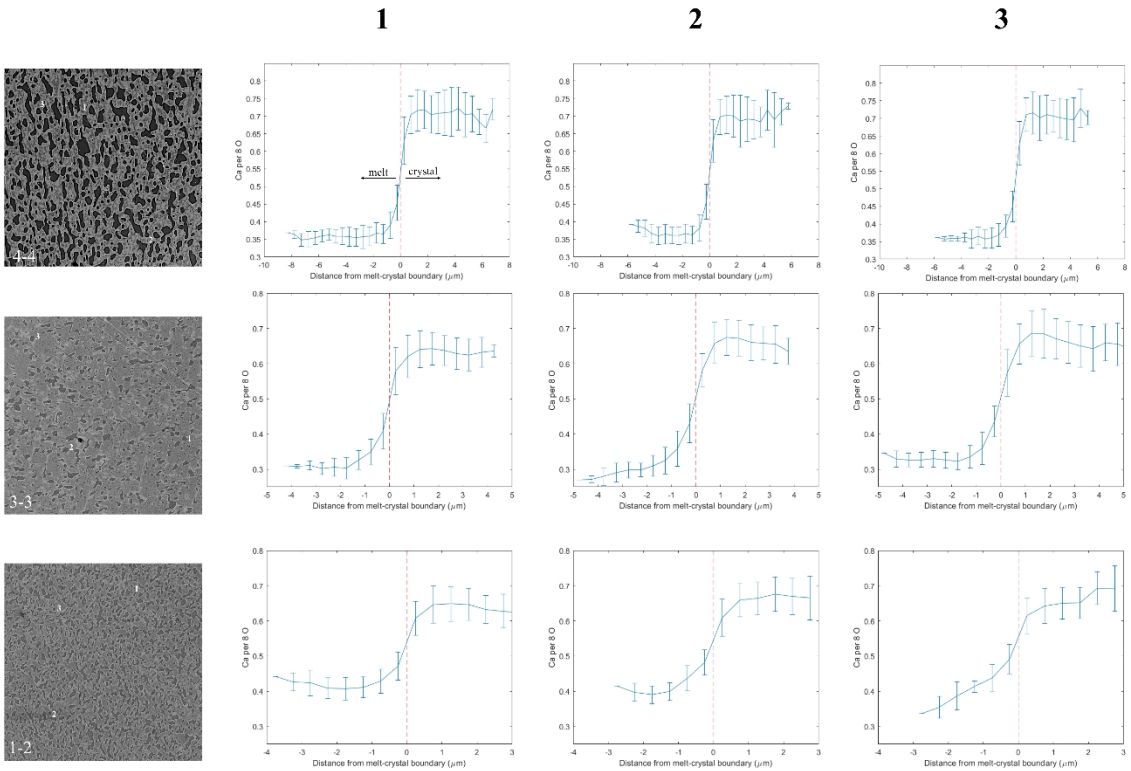

Figure 2.9. *Average Ca diffusion profile across individual melt pools.* Three melt pools each were selected in samples 4-4, 3-3, and 1-2, with the column numbers corresponding to the labeled melt pools in the BSE images. Na profiles of the same melt pools are shown in Figure 2.10. Error bars reflect ±1σ.

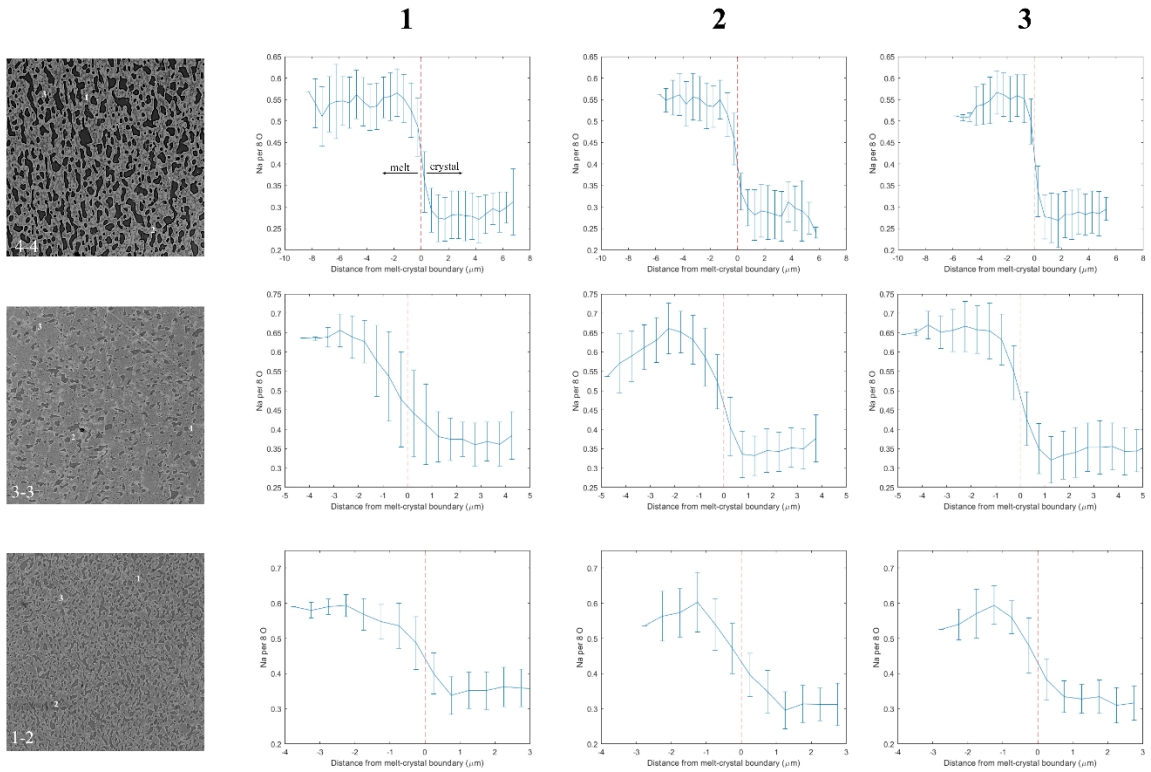

Figure 2.10. *Average Na diffusion profile across individual melt pools.* Three melt pools each were selected in samples 4-4, 3-3, and 1-2, with the column numbers corresponding to the labeled melt pools in the BSE images. Ca profiles of the same melt pools are shown in Figure 2.9. Error bars reflect ±1σ.

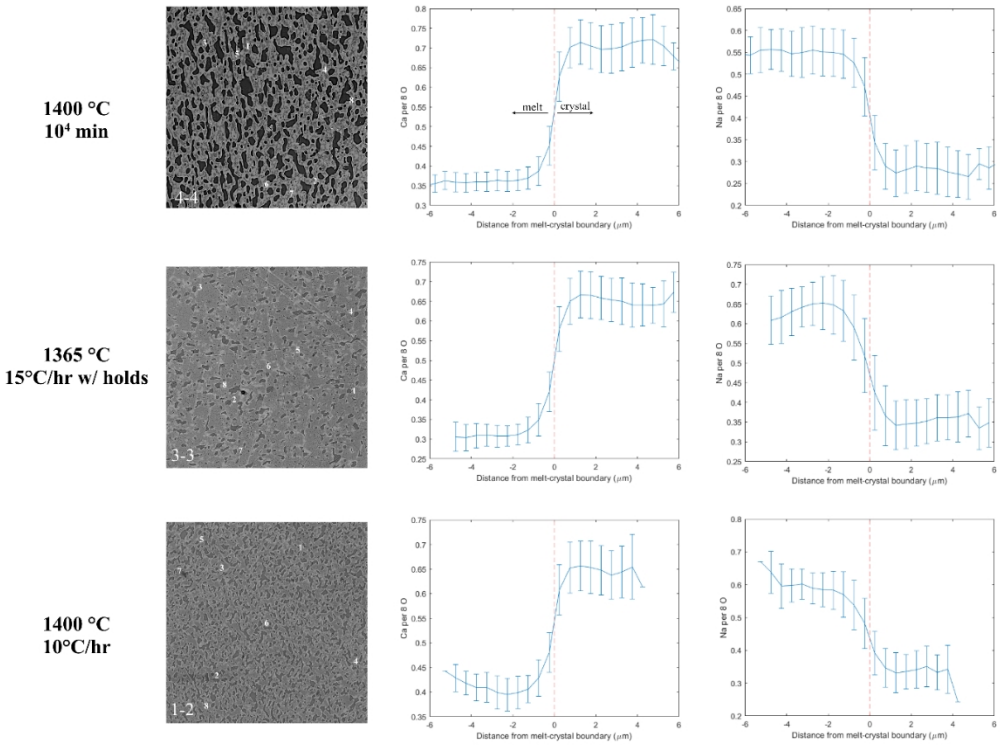

Figure 2.11. *Average Ca and Na diffusion profiles across eight melt pools.* Line profiles from eight melt pools were averaged to capture the generalized diffusion behavior of each sample. Error bars reflect ±1σ.

Discussion

Textural Evolution

Melt generation and connectivity is most often discussed in the context of multimineralic systems (*e.g.*, melt formation at a eutectic). In these scenarios, melt is thought to form at grain boundaries, achieving textural equilibrium by maturation of grain boundary geometry. As melting progresses, melt at grain boundaries becomes interconnected and can begin to migrate by porous flow, with considerations such as melt viscosity, permeability, and melt network geometries dictating melt migration. However, this suite of experiments on single crystals reveals an additional process that can occur: melt formation and segregation *within* the interior of a grain. Though less common, there are certain conditions that could

generate melt in this way. One such environment is exactly that which we have created, where heating rates are sufficiently rapid that the internal temperatures of the grains surpass the melting points of the individual phases quickly enough that melting can occur before the grain has completely melted from the boundary inward. Another is the case of melt generation originating from fluid inclusions within a grain – the presence of fluid would depress the solidus, causing melting to occur locally at lower temperatures compared to the dry inter-crystal medium, generating intragrain melts. Another is a peritectic assemblage, where the initial melting reaction involves one solid phase breaking down to melt and a second phase, rather than reacting with neighboring phases to generate melt. Finally, this scenario is to be expected in a monomineralic rock, such as dunite or anorthosite.

Observations from these experiments raise the following question about intragrain melting: what governs geometric changes and migration of the melt pools? Melt pool geometry naturally evolves to minimize the total energy of the system, which is accomplished by minimizing the area of high-energy interfaces. In the equilibrium experiments, nucleation of melt pools occurs in under 10^1 min, with the initial amount of melt estimated to be ~17% by area in sample 4-1, with most melt pools no more than 3 μm wide in the shortest visible dimension. We see many melt pool rods at low melt fraction. As the proportion of melt increases, the favored geometry becomes circular, but this process is relatively slow. Changes in melt geometries are dominated not by melt extraction and flow like in multimineralic systems, but rather through precipitation and dissolution kinetics. Based on the relative sizes of the melt pools in the transition from 1-1 to 1-2 and from 2-3 to 2-4, it appears that the evolution can occur in two ways: (1) an already circular melt pool continues to grow radially outwards, or (2) rod-shaped melt pools are broken up into smaller pieces as certain points along the rod close by precipitation, while the separated parts the rod are enlarged and rounded by dissolution.

Although analysis of these planar cross-sections provides an excellent starting point for discussion, future directions of this work would benefit from 3D analysis through methods such as x-ray computed tomography. 3D imaging techniques would add valuable information about the geometry of melt connectivity throughout the sample volume, allowing us to investigate topics such as the melt fraction threshold at which melt pools connect to each other or to the grain boundary.

Chemical Composition - Bulk

Though the timescales of observation in this study were not sufficiently long to achieve textural equilibrium, we are able to see a wide spectrum of chemical compositions among the samples, ranging from disequilibrium to near-equilibrium. Figure 2.6 shows the extent of disequilibrium for each set of heating rate experiments. Generally, the deviations behave as expected, with slower heating rates generating quenched melt and crystal compositions closer to equilibrium compared to faster rates. This representation of the data makes it clear that, for plagioclase, all heating rates yield some level of disequilibrium, supporting the idea that zoning in natural samples is a likely indicator of kinetic effects. Using this data to evaluate the assumption of phase boundary equilibrium, one possibility is that the boundary is in equilibrium but lags the temperature ramp, resulting in a composition that satisfies equilibrium at a lower temperature than that of the drop-quench. In this scenario, the lower-temperature equilibrium would predict that compositions in both phases are more sodic than the equilibrium prediction at the phase boundary. This is inconsistent with the observation that the solid and melt compositions both plot within the phase loop, with the solid more calcic than the equilibrium value. Another possibility is a metastable equilibrium at the phase boundary, where $\Delta\mu$ is zero but Gibbs energy is not globally minimized; that is, the slopes of the tangents to the molar Gibbs energy curves of the solid and liquid might be equal while their intercepts are different. This assumption corresponds to the idea that solid-liquid equilibrium at the boundary can be described using a distribution coefficient $\equiv$ (Morse, 2015)

that maintains its equilibrium value even when the compositions of solid and melt are not at the values predicted by the phase diagram. However, this notion is also rejected by the data, as it requires that both liquid and solid be shifted in the same direction, either towards higher Na or towards higher Ca. Such metastable equilibrium is not consistent with the observed behavior, where the solid has higher Ca than expected and the liquid has lower Ca than expected. The observation necessarily yields a value of K_D closer to unity than the equilibrium value.

Melt compositions were noted to deviate from the binary (Table 2.7) in both isothermal and heating rate experiments. Two possible explanations for this deviation could be: (1) heavy volatilization of Na during WDS measurement of the glass, or (2) the composition of the sample does not lie exactly on the albite-anorthite binary, skewing composition calculations. Initial EDS of the single crystals showed up to 0.04 potassium (K) per eight oxygens. Our assumed binary composition does not account for the incorporation of K, and this simplification of the system to two-component exchange neglects the orthoclase phase in the feldspar ternary.

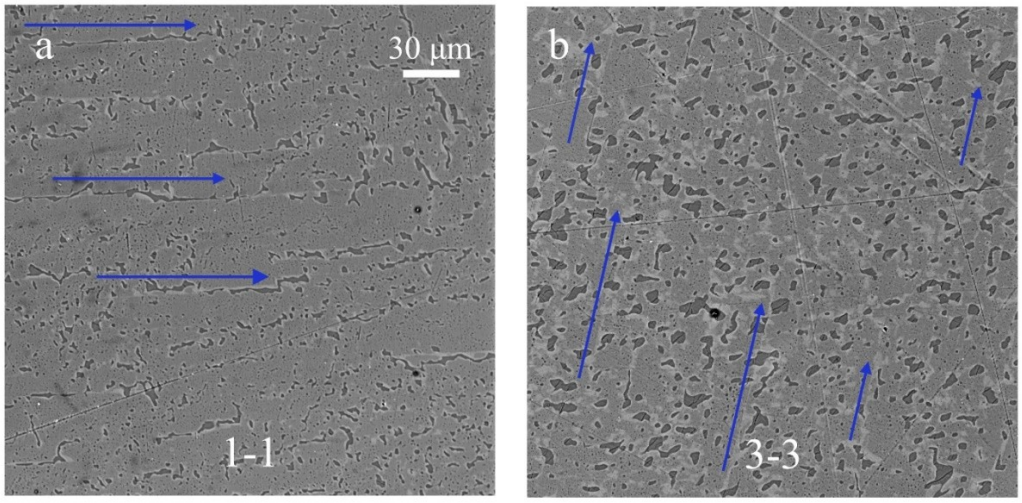

Figure 2.12. *Melt pool halos.* (a) 10 °C/hr ramp to 1365 °C with immediate quench. There is clearly a preferred orientation for several of the melt pool rods, indicated by the blue arrows. (b) 15 °C/hr ramp to 1365 °C with a subsequent 64 h hold. The

halos surrounding the melt pools appear to show a preferred orientation as well, indicated by the blue arrows.

BSE images (Figure 2.12) show "halos" of slightly higher contrast surrounding the darker melt pools. Comparison of Figures 2.4-2.5 tells us that these halos are not just optical artifacts, but rather direct indicators of chemical gradients and therefore proxies to understand diffusion and melt migration timescales. For example, samples 1-3 and 3-3 together tell an interesting story. They both underwent heating of the same order of magnitude and were quenched at the same temperature, but sample 3-3 was held for 64 h after reaching the target temperature. This hold caused the rod-shaped melt pools to round out over time to minimize energy, creating the notable difference in melt pool geometry between the two samples. However, it appears that chemical diffusion rates were not as fast as those of the precipitation/dissolution during the isothermal hold—the halos seen in Figure 2.12b are trails of high calcium, low sodium regions, likely left behind by the textural evolution of the melt pools, considering the similarities between the preferred orientation in 1-1 and the preferred orientation of several of the halos in 4b. This comparison allows us to estimate a rate of change for the moving phase boundary under these conditions: if we treat the ramp rates as functionally identical, given that they are the same order of magnitude, the velocity of the moving boundary is equal to the reduction in longest dimension of the melt pool divided by the hold time, yielding ~0.5 μm/hr. This provides a good starting point or lower bound for the velocity of the moving boundary during phase change, to be further explored in Chapter 3.

Chemical Composition – Line Profiles

Equilibrium at crystal-melt interfaces is a commonly enforced boundary condition in dissolution and other phase change studies. However, as previously stated, it is an unproven assumption, especially in the case of melting. Observation of the average measured line profiles in this study (Figure 2.11) seems to indicate that equilibrium compositions are not achieved at the boundary, based on electron

probe analyses of Ca and Na in both melt and crystal phases with spacing between points of 0.5 μm, supporting the need to study disequilibrium boundary conditions. However, before concluding that we have produced disequilibrium phase boundary compositions, we must first consider the possibility that the phase boundaries are in equilibrium, but the analytical method cannot get close enough to the interface to resolve the surface compositions. Given the beam size (focused to 0.1 μm diameter) and spatial resolution (step size 0.5 μm) of the analytical method, what is effectively being measured is expressed in Equation 2.1:

$$C_{measured} = \frac{\int_{x_1}^{x_2} C\,(x)\,dx}{x_2 - x_1} \#\,(2.1)$$

That is, each concentration measurement is actually an average: the total amount of the component present over some distance, divided by that distance. Figure 2.13 takes sample 4-4 as an example and sketches some possible concentration profiles that would satisfy the requirements of (1) having equilibrium compositions at the boundary, (2) averaging out to the measured concentrations in the melt and the crystal at points centered 0.5 μm from the boundary on either side (from Figure 2.11), and (3) re-approaching the measured equilibrium concentrations beyond 0.5 μm from the boundary on either side. In order for the three conditions to be satisfied, the profiles must have large positive and negative concavity over a short distance. The material flux necessary to maintain this can be approximated using Fick's second law. Sample 4-4 is conducted at 1400 °C, for which the diffusion coefficients are $D_{Ca}^{melt} \sim 10^{-14}$ m^2/s and $D_{Ca}^{solid} \sim 10^{-21}$ m^2/s. Taking Profile 1 in both melt and crystal to be parabolic, concentration in mole fraction calcium can be expressed vertex form $C_m = -2.56\,(x - 0.25)^2 + 0.52$ and $C_s = 2.88\,(x - 0.25)^2 + 0.34$, respectively. $\frac{\partial^2 C_m}{\partial x^2} = -5.12\ \mu m^{-2} = -5.12 * 10^{12}\ m^{-2}$ and $\frac{\partial^2 C_s}{\partial x^2} = 5.76\ \mu m^{-2} = 5.76 * 10^{12}\ m^{-2}$. Evaluating the concentration flux

necessary to maintain this curvature at $x = 0$ to ± 0.25 μm, we get that the timescales over which this profile could persist in the melt and crystal would be less than one second and about one year, respectively. Therefore, any anomalous concave concentration profiles in the melt would diffuse away so quickly that it would not support the possibility that there is an unmeasured gradient due to limitations on analytical capabilities. However, we acknowledge such a profile could persist in the solid on timescales longer than our experiments; even so, because there are no known driving forces to generate such an unusual profile to begin with, and this behavior is not seen in other diffusion experiments or natural samples, it seems reasonable to say that the likelihood that our analytical capability is the limiting factor in resolving an accurate profile is low.

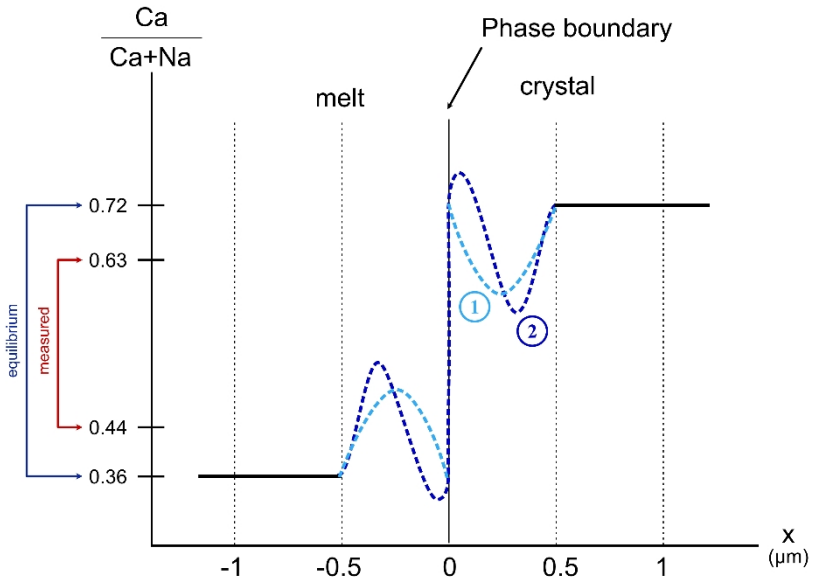

Figure 2.13. *Chemical gradients to satisfy equilibrium at the boundary.* Dotted profiles 1 and 2 are proposed chemical composition gradients for sample 4-4 that would satisfy (1) equilibrium compositions at the boundary (2) measured average concentrations at 0.5 μm, and (3) an approach to equilibrium compositions past 0.5 μm.

Concluding Remarks

We have conducted a series of equilibrium and kinetic experiments on plagioclase, a common constituent in igneous systems. Analysis of the samples showed that timescales of 10^4 min are required to achieve chemical equilibrium between melt and crystal phases in the sample. Any shorter timescales and any imposed heating rates in this study only resulted in disequilibrium compositions, lending confidence to the argument that kinetics should be considered during phase change in igneous systems, particularly in slow-diffusing phases such as plagioclase. We utilize these data to further explore the constraints on disequilibrium melting in Chapter 3.

References

Anderson, A. (1984). *Probable relations between plagioclase zoning and magma dynamics, Fuego Volcano, Guatemala*. American Mineralogist.

Bowen, N. L. (1913). The melting phenomena of plagioclase feldspars. *American Journal of Science, 35*, 577–599.

Cabane, H., Laporte, D., & Provost, A. (2005). An experimental study of Ostwald ripening of olivine and plagioclase in silicate melts: Implications for the growth and size of crystals in magmas. *Contributions to Mineralogy and Petrology, 150*(1), 37–53. https://doi.org/10.1007/s00410-005-0002-2

Chen, Y., & Zhang, Y. (2008). Olivine dissolution in basaltic melt. *Geochimica et Cosmochimica Acta, 72*(19), 4756–4777. https://doi.org/10.1016/J.GCA.2008.07.014

Homma, F. (1935). The Classification of the Zonal Structure ef Plagioclase. *Memoirs of the College of Science, Kyoto Imperial University, 11*(2), 135-155.

Jackson, K. A. (1984). Crystal growth kinetics. *Materials Science and Engineering, 65*(1), 7–13. https://doi.org/10.1016/0025-5416(84)90194-0

Jackson, K. A. (2010). *Kinetic Processes: Crystal Growth, Diffusion, and Phase Transitions in Materials*. John Wiley & Sons.

Karato, S. (1989). Grain growth kinetics in olivine aggregates. *Tectonophysics, 168*(4), 255–273. https://doi.org/10.1016/0040-1951(89)90221-7

Liang, Y. (1999). Diffusive dissolution in ternary systems: Analysis with applications to quartz and quartzite dissolution in molten silicates. *Geochimica et Cosmochimica Acta, 63*(23–24), 3983–3995. https://doi.org/10.1016/S0016-7037(99)00203-3

Liang, Y. (2000). Dissolution in molten silicates: Effects of solid solution. *Geochimica et Cosmochimica Acta, 64*(9), 1617–1627. https://doi.org/10.1016/S0016-7037(00)00331-8

Liang, Y. (2003). Kinetics of crystal-melt reaction in partially molten silicates: 1. Grain scale processes. *Geochemistry, Geophysics, Geosystems, 4*(5). https://doi.org/10.1029/2002GC000375

Luo, S. N., & Ahrens, T. J. (2004). Shock-induced superheating and melting curves of geophysically important minerals. *Physics of the Earth and Planetary Interiors, 143–144*(1–2), 369–386. https://doi.org/10.1016/J.PEPI.2003.04.001

Luo, S. N., Ahrens, T. J., Çağın, T., Strachan, A., Goddard, W. A., & Swift, D. C. (2003). Maximum superheating and undercooling: Systematics, molecular dynamics simulations, and dynamic experiments. *Physical Review B, 68*(13), 134206. https://doi.org/10.1103/PhysRevB.68.134206

Maaløe, S. (1976). The Zoned Plagioclase of the Skaergaard Intrusion, East Greenland. *Journal of Petrology*, *17*(3), 398–419. https://doi.org/10.1093/PETROLOGY/17.3.398

Macris, C. A., Asimow, P. D., Badro, J., Eiler, J. M., Zhang, Y., & Stolper, E. M. (2018). Seconds after impact: Insights into the thermal history of impact ejecta from diffusion between lechatelierite and host glass in tektites and experiments. *Geochimica et Cosmochimica Acta*, *241*, 69–94. https://doi.org/10.1016/j.gca.2018.08.031

Mei, Q. S., & Lu, K. (2007). Melting and superheating of crystalline solids: From bulk to nanocrystals. *Progress in Materials Science*, *52*(8), 1175–1262. https://doi.org/10.1016/J.PMATSCI.2007.01.001

Morgan, Z., & Liang, Y. (2003). An experimental and numerical study of the kinetics of harzburgite reactive dissolution with applications to dunite dike formation. *Earth and Planetary Science Letters*, *214*(1–2), 59–74. https://doi.org/10.1016/S0012-821X(03)00375-3

Morse, S. A. (2015). Linear partitioning in binary solutions: A review with a novel partitioning array. *American Mineralogist*, *100*(5–6), 1021–1032. https://doi.org/10.2138/AM-2015-5056

Nancollas, G. H., & Purdie, N. (1964). The kinetics of crystal growth. *Quarterly Reviews, Chemical Society*, *18*(1), 1–20.

Newcombe, M. E., Fabbrizio, A., Zhang, Y., Ma, C., Le Voyer, M., Guan, Y., Eiler, J. M., Saal, A. E., & Stolper, E. M. (2014). Chemical zonation in olivine-hosted melt inclusions. *Contributions to Mineralogy and Petrology*, *168*(1), 1–26. https://doi.org/10.1007/S00410-014-1030-6/FIGURES/13

Nielsen, A. E., & Toft, J. M. (1984). Electrolyte crystal growth kinetics. *Journal of Crystal Growth*, *67*(2), 278–288. https://doi.org/10.1016/0022-0248(84)90188-X

Pearce, T. H., & Kolisnik, A. M. (1990). Observations of plagioclase zoning using interference imaging. *Earth-Science Reviews*, *29*(1–4), 9–26. https://doi.org/10.1016/0012-8252(0)90024-P

Phemister, J. (1934). Zoning in plagioclase felspar. *Mineralogical Magazine and Journal of the Mineralogical Society*, *23*(145), 541–555.

Saper, L. M., & Stolper, E. M. (2020). Controlled cooling-rate experiments on olivine-hosted melt inclusions: Chemical diffusion and quantification of eruptive cooling rates on Hawaii and Mars. *Geochemistry, Geophysics, Geosystems*, *21*(2). https://doi.org/10.1029/2019GC008772

Shea, T., Lynn, K. J., & Garcia, M. O. (2015). Cracking the olivine zoning code: Distinguishing between crystal growth and diffusion. *Geology*, *43*(10),

935–938. https://doi.org/10.1130/G37082.1

Tsuchiyama, A. (1985). Dissolution kinetics of plagioclase in the melt of the system diopside-albite-anorthite, and origin of dusty plagioclase in andesites. *Contributions to Mineralogy and Petrology*, *89*(1), 1–16. https://doi.org/10.1007/BF01177585/METRICS

Tsuchiyama, A. (1986). Melting and dissolution kinetics: Application to partial melting and dissolution of xenoliths. *Journal of Geophysical Research: Solid Earth*, *91*(B9), 9395–9406. https://doi.org/10.1029/JB091IB09P09395

Tsuchiyama, A., & Takahashi, E. (1983). Melting kinetics of a plagioclase feldspar. *Contributions to Mineralogy and Petrology*, *84*(4), 345–354. https://doi.org/10.1007/BF01160286

Wunderlich, B. (2007). One hundred years research on supercooling and superheating. *Thermochimica Acta*, *461*(1–2), 4–13. https://doi.org/10.1016/J.TCA.2006.11.015

Zhang, Y., Walker, D., & Lesher, C. E. (1989). Diffusive crystal dissolution. *Contributions to Mineralogy and Petrology*, *102*(4), 492–513. https://doi.org/10.1007/BF00371090/METRICS

Chapter 3

KINETICS OF RAPID MELTING IN TWO-COMPONENT SYSTEMS: NUMERICAL METHODS

Introduction

As established in Chapter 2, melting is important across numerous geologic settings, but its kinetics are insufficiently characterized. Our experiments add to the evidence that accurate descriptions of melting may require integration of disequilibrium effects. To understand how natural and experimental observations constrain chemical processes, we turn to modeling. Numerical modeling within geochemistry is a well-established method used to explore topics such as the dynamics of explosive eruptions, geothermometry, and ocean biogeochemical cycles (Albaréde 1996; Lasaga & Kirkpatrick 1981; Zhang 2008). Typically, models are separated into two categories: forward and inverse. Forward modeling is a process in which established principles and/or parameters are used to simulate and predict the outcome of a system when given initial conditions. Inverse modeling is a process used to constrain unknown parameters or system behaviors based on observed data. The two methods can be complementary, and the information gained using both methods can contribute to bridging the gap between simple physical principles and complex observations. In geochemistry, investigation of phase change dynamics usually employs methods of forward modeling.

In both experimental and computational methods, equilibrium conditions are the most convenient to explore because they are path-independent. Several forward modeling strategies have already been developed to describe equilibrium crystallization and melting in a self-consistent manner (Asimow & Ghiorso 1998; Ghiorso et al. 2002; Ghiorso & Sack 1995; Gualda et al. 2012; Jennings & Holland 2015). Much of the existing work in this field leans heavily on equilibrium assumptions to reduce the number of unknowns when solving coupled systems of

equations, oftentimes by drawing from thermodynamic data. While these methods allow for improved computational tractability of these problems, the next natural step in the investigation of melting is to generate more rigorous descriptions of time-dependent disequilibrium evolution to encompass a wider breadth of realistic scenarios. Admittedly, this is challenging—the interplay between volume diffusion, surface reaction rates, and spatially varying chemical potentials leads to nonlinear feedbacks between rates of phase boundary motion and the thermodynamic forces driving such motion. While trace element kinetics and partitioning during phase changes have been more extensively studied and modeled (Grose & Afonso 2019; Kogiso et al. 2004; Liang & Liu 2016; Qin 1992; Spiegelman & Elliott 1993; Spiegelman & Kenyon 1992), few studies have addressed the difficult question of major element disequilibrium in melting (Keller & Katz 2016; Rudge et al. 2011; Tirone & Sessing 2017). Tracking major element transport during melting is a demanding task, as it requires gradient calculations of thermodynamic potentials at each time step, as well as methods to determine component fluxes and melt production rates. Some of the aforementioned major element studies approach these challenges using phenomenological coefficients or parameterizations in their kinetic or thermodynamic balances. Though certainly useful, the basis of these methods is not grounded in fundamental physical principles, instead requiring retroactive justification of their physical meanings. In this work, we aim to address some of the difficulties encountered in existing literature when depicting major element evolution during melting.

Tracking one-dimensional (1D) melt evolution is a moving boundary problem that falls under the class of mathematical investigations called Stefan problems. These problems typically consist of a set of partial differential equations (PDEs) with a unique boundary condition (Stefan condition) that describes the velocity of the moving phase boundary. Various numerical methods have been developed to solve these problems, with different combinations of implicit/explicit finite difference schemes combined with fixed/variable grids in time or space. This

method is applicable not only to melting, but also to analogous processes such as crystal dissolution, which has been more extensively studied in geochemical literature (Liang 2003). As discussed in Chapter 2, standard crystal dissolution models assume that the crystal-melt interfacial compositions exist on the solidus and liquidus, respectively, to maintain equilibrium. In contrast, our model allows for departure from this constraint. Comparison of these disequilibrium simulation results to the experimental data allows us to determine the validity of these assumptions. Here, we build a forward model that describes 1D, two-component melting by tracking chemical diffusion within each phase and utilizing thermodynamic potentials to determine chemical fluxes across the phase boundary and minimization of free energy to satisfy the Stefan condition and dictate boundary velocity.

Methods

Model Framework

Consider a plagioclase crystal undergoing melting, following the experiments described in Chapter 2. At first, only the solid phase is present, but past the solidus, the first melt pools begin to nucleate within the crystal. In this monomineralic system, we select a given region of interest consisting of a circular melt pool immediately after nucleation and the surrounding solid. Drawing a line from the center of the melt pool radially outward some distance L, this is defined as the total length scale of our 1D model. For simplicity, our model is not concerned with the dynamics of nucleation, but rather the composition profile across L after melting occurs. In practice, all equations are solved after nondimensionalizing in time and space with the following choices of characteristic length- and timescale,

$$\tilde{t} = \frac{t}{t_{max}}, \qquad \tilde{x} = \frac{x}{L}$$

where t_{max} is the total runtime of the experiment/simulation. However, all expressions are expressed below in dimensional form for clarity.

Far from the phase boundary, concentrations (C) of each component (Ca or Na) follow Fick's second law within both the solid and liquid phases. Melt (□□) and solid (□ phases are denoted in subscripts.

$$\frac{\partial \square_{\square\square}}{\partial \square\square} = \square\square_{\square\square} \frac{\partial^2 \square_{\square\square}}{\partial \square\square^2} \quad \#(3.1)$$

$$\frac{\partial \square_{\square\square}}{\partial \square\square} = \square\square_{\square\square} \frac{\partial^2 \square_{\square\square}}{\partial \square\square^2} \quad \#(3.2)$$

Initial conditions assume the concentrations of a given component in the two phases are at equilibrium at an initial temperature T, with constants α and β representing the melt and solid compositions, respectively. The phase boundary location is denoted by x_b.

$$\square\square\square\square 1: \square_{\square\square}\left(0 \le \square\square < \square_{\square\square}, \square\square = 0\right) = \square\square \quad \#(3.3)$$

$$\square\square\square\square 2: \square_{\square\square}\left(\square_{\square\square} \le \square\square < \square\square, \square\square = 0\right) = \square\square \quad \#(3.4)$$

No-flux boundary conditions (BCs) are imposed on either end of the profile, far from the phase boundary.

$$\square\square\square\square 1: \frac{\partial \square_{\square\square}}{\partial \square\square}\left(\square\square = 0, \square\square\right) = 0 \quad \#(3.5)$$

$$\square\square\square\square 2: \frac{\partial \square_{\square\square}}{\partial \square\square}\left(\square\square = \square\square\square\square\right) = 0 \quad \#(3.6)$$

A unique Stefan condition was developed to describe behavior on either side of the phase boundary (BC 3 & 4).

$$\square\square\square\square 3 \square\square\square\square\square\square 4 \&: \frac{\partial \square_{\square\square}}{\partial \square\square}\left(\square\square = \square_{\square\square^-}, \square\square\right) + \square\square\,\square_{\square\square} + \square_{\square\square\square\square\square\square} \Delta\square\square$$
$$= \frac{\partial \square_{\square\square}}{\partial \square\square}\left(\square\square = \square_{\square\square^+}, \square\square\right) + \square\square\,\square_{\square\square} - \square_{\square\square\square\square\square\square} \Delta\square\square \quad \#(3.7)$$

The first terms on each side of the equality are the changes in concentration of the component adjacent to the boundary, independent of boundary motion.

To that, we add on either side the second term $+VC_{m/s}$ to describe the velocity V of the moving boundary and whether the movement adds or removes the component from either the melt or solid phase. This effectively determines whether the phase boundary region will experience net melting or crystallization. Eqs. 3.8–3.9 describe how thermodynamic relationships and Gibbs free energy minimization are used to determine the direction and magnitude of the velocity, such that a positive $+V$ is defined as the melt front advancing to the right (Figure 3.1).

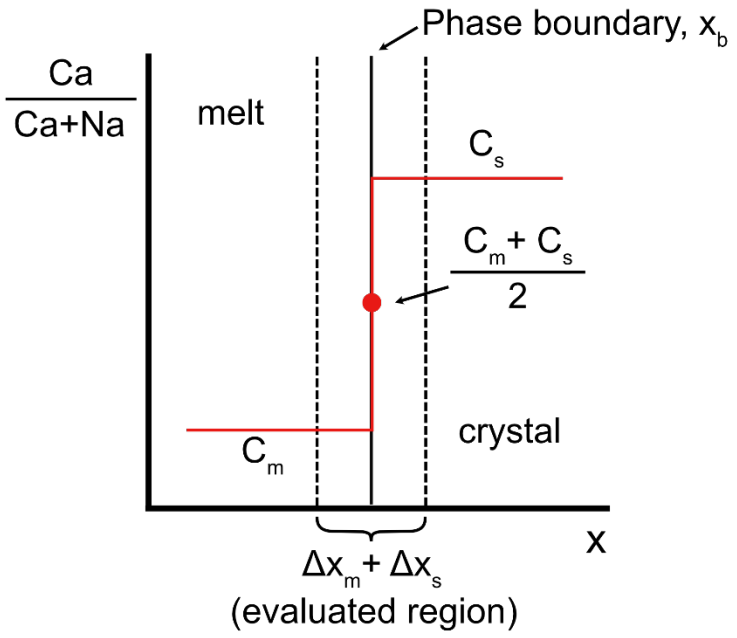

Figure 3.1. *Moving boundary at the melt-crystal interface*. Velocity of the moving boundary is determined by Gibbs free energy minimization based on existing compositions of the melt, crystal, and a hypothetical averaged composition, calculated over a small step $\Delta x_m + \Delta x_s$ on either side of the boundary. $C_{m/s}$ denotes the concentration of Ca in each phase.

$$\frac{\partial G}{\partial x} = \mu_{Ca,melt} - \mu_{Ca,cryst} \quad (3.8)$$

$$C_{m/s} = C_{melt}\left(\frac{C_m + C_s}{2}\right), \qquad \Delta x = \begin{cases} x_{melt} - x_b & \text{if } \mu_{Ca} < \mu_{Ca,melt} \\ x_{cryst} - x_b & \text{if } \mu_{Ca} < \mu_{Ca,cryst} \\ 0 & \text{if } \mu_{Ca,melt} < \mu_{Ca} < \mu_{Ca,cryst} \end{cases} \quad \text{where} \quad (3.9)$$

$$C_{m/s} = C_{melt}\left(\frac{C_m + C_s}{2}\right).$$

To calculate V at each time step, the free energies associated with (1) melting (g_m), (2) crystallization (g_s), or (3) no change (g_{ms}) are determined based on the compositions of material immediately adjacent to the boundary. Δg is then defined as maximum free energy decrease that can be obtained by replacing g_{ms} with either g_m (a driving force for melting) or g_s (a driving force for crystallization). k_{growth} acts as a scaling factor, translating the energy difference into a step size of the moving boundary.

The last term on either side of the equation introduces a kinetic process associated with the chemical exchange across the boundary that, in turn, allows us to relax the conventional assumption of strict chemical equilibrium at the melt-crystal interface. Existing phase change literature has shown cases in which equilibrium boundary conditions do not satisfy experimentally determined diffusion profiles, prompting the development of a parameter that accounts for this discrepancy (Fogel & Rutherford 1995; Saal et al. 2008). k_{exch} can be thought of as describing the permeability of the interface: when k_{exch} goes to zero, the boundary is impermeable to chemical exchange, and when it goes to infinity, chemical exchange occurs instantaneously. The driving force for chemical exchange across the boundary is the difference in chemical potentials ($\Delta\mu$) of the endmembers in the two phases. Spontaneity of the change in either direction will be calculated by Eq. 3.10, where $\Delta\mu$ is defined to be negative (–) if it is more favorable for Ca to move from melt to solid than for Na to move from melt to solid.

To reduce complexity of the two-component system, we must assume the plagioclase sample falls strictly on the $NaAlSi_3O_8$-$CaAl_2Si_2O_8$ (Ab-An) binary, such that $1 = X_{An}+X_{Ab}$. We acknowledge here that imposing this strict one-to-one exchange of components across the boundary to simplify the tracking of chemical species is not exactly accurate given the existence of the feldspar ternary and the presence of

potassium in the samples used in Chapter 2. Additionally, as seen in the experimental results, melt compositions may deviate from feldspar stoichiometry altogether.

Our formulation of this moving boundary condition allows us to parameterize any unexpected effects using constants k_{exch} and k_{growth}. In the limit of large values of k_{exch} and k_{growth}, this model reduces to the conventional assumption of equilibrium at the boundary applied in most formulations of the Stefan problem. As k_{growth} becomes small enough that the system cannot maintain Δg strictly equal to zero, this term becomes a potential new rate-limiting step in the achievement of equilibrium (*e.g.*, if the boundary cannot move fast enough to keep up with imposed changes during a temperature ramp). That is, at high rates of temperature change that require rapid melting to maintain equilibrium, the melt-solid phase boundary may be unable to move fast enough to maintain equilibrium, independently of the rate at which the components diffuse on either side of the boundary. On the other hand, as k_{exch} becomes small enough that the system cannot maintain $\Delta\mu$ strictly equal to zero, this term becomes another potential new rate limiting step in the achievement of equilibrium, if the chemical components cannot transfer across the boundary fast enough to keep up with the flux necessary to balance the diffusive and grain-boundary motion fluxes. This is the most novel aspect of our formulation. Exploration of these two parameters will be discussed in the Results section.

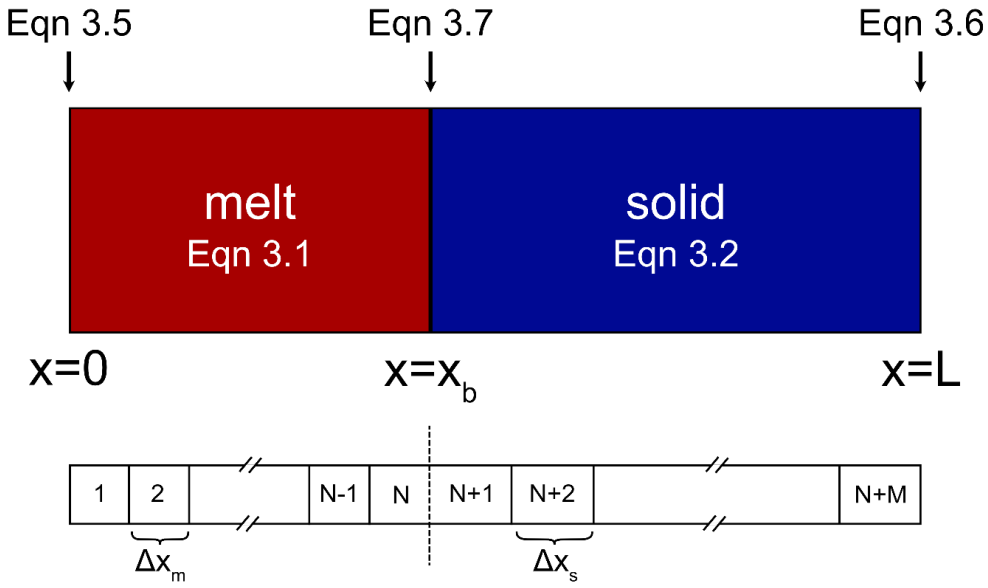

Figure 3.2. *Finite difference scheme*. Melt and solid regions are defined using a variable space grid, with a fixed number of points on either side of the moving boundary, x_b. Adapted from Liang (2003).

Numerical Methods

To implement the model framework, a finite difference method was employed with a fixed time, variable space grid (Crank 1975). A fixed time method was selected because the heating rate (and therefore duration) of each run was an independent variable in our experiments, allowing us to clearly define t_{max} for each simulation for direct comparison to experimental results. Our work closely follows that of Liang (2003), with modifications to accommodate our novel parameters.

As shown in Figure 3.2, melt and crystal domains were instantiated with a fixed number of grid points – N points in the melt, M in the solid – defined on either side of the boundary, x_b, such that $\Delta x_m = x_b/N$ and $\Delta x_s = (L-x_b)/M$. Step sizes Δx_m and Δx_s are updated with each time step Δt. Let [illegible] be the concentration of the given component in the melt at time point i and at grid point j, where $t = i\Delta t$.

Discretizing Eqn. 3.1 using a forward in time, central in space finite difference scheme:

$$\frac{T_{i,j}^{n+1} - T_{i,j}^{n}}{\Delta t} = \frac{\alpha_f}{(\Delta x)^2}\left(T_{i+1,j}^{n} - 2T_{i,j}^{n} + T_{i-1,j}^{n}\right)$$

$$T_{i,j}^{n+1} = T_{i,j}^{n} + \frac{\alpha_f \Delta t}{(\Delta x)^2}\left(T_{i+1,j}^{n} - 2T_{i,j}^{n} + T_{i-1,j}^{n}\right)$$

Defining

$$r_f = \frac{\alpha_f \Delta t}{(\Delta x)^2}, \qquad r_s = \frac{\alpha_s \Delta t}{(\Delta x)^2}$$

We get

$$T_{i,j}^{n+1} = r_f T_{i+1,j}^{n} + (1 - 2r_f) T_{i,j}^{n} + r_f T_{i-1,j}^{n} \quad (3.11)$$

The analogous expression for the solid (Eqn 3.2) is

$$T_{i,j}^{n+1} = r_s T_{i+1,j}^{n} + (1 - 2r_s) T_{i,j}^{n} + r_s T_{i-1,j}^{n} \quad (3.12)$$

Discretizing initial conditions (Eqns. 3.3-3.4) results in

$$T_{i,1}^{0} = T_f \quad (3.13)$$

$$T_{i,jmax+1}^{0} = T_s \quad (3.14)$$

Using a central difference scheme for BC 1 (Eqn 3.5),

$$\frac{T_{i,2} - T_{i,0}}{2\Delta x} = 0$$

Rearranging, we get that

$$T_{i,0} = T_{i,2}$$

Which can be substituted into the expression:

$$T_{i,1}^{n+1} = T_{i,1}^{n} + r_f\left(T_{i+1,1}^{n} - 2T_{i,1}^{n} + T_{i,0}^{n}\right) \quad (3.15)$$

The analogous expression for BC 2 (Eqn 3.6) is

$$C_{0,i+1} = (1 - 2k_p)\,C_{0,i} + 2k_p\,C_{1,i} \quad (3.16)$$

Boundary conditions 3 & 4 can be discretized using a second order asymmetric finite difference scheme

$$D_L\left(\frac{3C_{0,i} - 4C_{1,i} + C_{2,i}}{2\Delta x}\right)_{i+1} + V C_{0,i} = D_S\left(\frac{-3C_{N+1,i} + 4C_{N,i} - C_{N-1,i}}{2\Delta x}\right)_{i+1} + V C_{N+1,i} \quad (3.17)$$

Where V is calculated with Eqn. 3.8 using the component concentrations at the boundary grid points,

$$k_L = k_L\left(\frac{C_{0,i} + C_{1,i}}{2}\right)_{i+1} \qquad k_S = k_S\left(\frac{C_{N+1,i} + C_{N,i}}{2}\right)_{i+1} \qquad C_{avg} = \frac{k_L(C_L)_{i+1} + k_S(C_S)_{i+1}}{2}$$

And the exchange term $\Delta\mu$ is calculated based on the compositions adjacent to the phase boundary, N in the melt and N+1 in the solid:

$$\Delta\mu = \Delta x_i \left[\left(\mu_L(C_{N,i}) - \mu_L(C_{avg})\right) - \left(\mu_S(C_{N+1,i}) - \mu_S(C_{avg})\right)\right] \quad (3.18)$$

After the calculation for each time step i is completed, the grid spacing is updated to reflect the new location of the phase boundary based on the calculated velocity (denoted "old" vs "new"). This gives us $x_{m,new} = x_{m,old} + \Delta x_m$, $\Delta x_m = V_{new}/N$, and $\Delta x_s = (L - x_{m,new})/M$. All concentrations calculated for time step $i+1$ must be converted into concentrations on the new grid using the following relations:

$$C_{L,new} = C_{L,new} + \frac{\left(C_{L,new} - C_{L,old}\right)\Delta x}{x_{m,new}} * \frac{C_{L,old+1} - C_{L,old-1}}{2\Delta x} \quad (3.19)$$

$$C_{S,new} = C_{S,new} + \frac{\left(x - x_{m,new}\right)\Delta x}{x - x_{m,new}} * \frac{C_{S,old+1} - C_{S,old-1}}{2\Delta x} \quad (3.20)$$

The process described above is repeated until $t = i\Delta t = t_{max}$. Fully implicit methods such as the one described above have the benefit of unconditional stability with respect to the time step size. However, due to the computational intensity of simultaneously solving the system of equations, it is beneficial to optimize for a time step that is sufficiently small to capture interesting behavior at the boundary while sufficiently large to minimize i.

We use matrix operations to achieve our result, framing our system of equations in the form $\boldsymbol{A}x = b$ and solving the system using a forward difference in time. $\boldsymbol{A}$ is a sparse square matrix with dimensions N+M, containing coefficients to be multiplied by the elements of x (a vector of length N+M concentrations at each grid point for current time point i, [illegible] to yield the elements of b (a vector of length N+M concentrations at each grid point for subsequent time point $i+1$, [illegible]). The structure of the finite difference operators and boundary conditions used make $\boldsymbol{A}$ tridiagonal. In the future it might prove necessary to adopt an implicit or semi-implicit scheme, in which case inversion of the matrix will be required and the tridiagonal structure will make this operation efficient.

Application of experimental data to model framework

Ideally, k_{growth} *and* k_{exch} should be the only unknown parameters in our modeling, because experimental constraints are available to define the other parameters, namely the Gibbs energies, chemical potentials, and diffusivities in the solid and melt phases. Here we describe our choice of (possibly provisional) values for these parameters.

Solid and melt phases were treated with asymmetric solution models, with standard chemical potentials and solid excess mixing terms drawn from rhyolite-MELTS. Because rhyolite-MELTS was not calibrated to plagioclase endmember compositions in the liquid phase, it does not predict the melting points of pure albite and anorthite correctly (in contrast to the melting points of quartz, corundum,

wollastonite, and sodium metasilicate, which are constraints on the model). Therefore correction terms were applied to the liquid standard state chemical potentials to enforce expected behavior, such that ◆◆◆◆◆◆◆◆ = ◆◆◆◆◆◆◆◆ at 1095°C and ◆◆◆◆◆◆◆◆ = ◆◆◆◆◆◆◆◆ at 1550°C. The partial molar heat capacities of oxide components in the melt were adopted directly from rhyolite-MELTS, so the correction term is a simple constant shift in the standard enthalpies of the two end member liquid species. Additionally, the rhyolite-MELTS model is not designed to fit simple-system phase diagrams and does a poor job matching the known shape of the experimental phase loop for plagioclase (Bowen, 1913). We manually tuned the excess parameters of an asymmetric regular solution model between albite and anorthite end members in the liquid to obtain an optimal fit to the phase diagram, yielding chemical potentials and Gibbs energy functions that accurately predict the equilibrium behavior and can also be used to model the driving forces arising from disequilibrium.

Diffusion coefficients within the solid and the melt were drawn from existing literature. Within the solid, the CaAl-NaSi interdiffusion coefficient of plagioclase (An_{80}, based on homogenization of Huttenlocher lamellae, and so limited to the direction perpendicular to 03 T) has been measured experimentally and was used for Equation 3.2 (Grove et al. 1984).

$$◆◆_◆ = ◆◆◆◆◆◆◆◆◆◆◆◆◆◆ = 1.099 * 10^{-3} \exp\left(\left(-517 \pm 21 ◆◆◆◆/◆◆◆◆◆◆\right)/◆◆◆◆\right) \left(◆◆^2/◆◆\right) \# \left(3.22\right)$$

However, this interdiffusion value has not been measured in melt; an assumption was made that the slowest-diffusing among the coupled elements would be the limiting factor and hence provide a potential proxy for the interdiffusion coefficient. Therefore, the experimentally measured Si self-diffusion coefficient in a dry dacitic liquid was used for the melt, with *P* given in GPa and *T* in K (Tinker & Lesher, 2001):

$$◆◆_◆◆ = ◆◆◆◆◆◆◆◆◆◆ = \exp\left(\left(-3.1943 \pm 1.603\right) ◆◆ - \frac{\left(54245 \pm 690\right) - \left(8523 \pm 2984\right) ◆◆}{◆◆}\right) \left(◆◆^2/◆◆\right) \# \left(3.23\right)$$

Experimental results from Chapter 2 indicated that textural evolution of the samples when held at constant temperature results in moving phase boundaries at rates of ~0.5 μm/hr. Together with the thermodynamic model for Δg, this yields an initial estimate for k_{growth}. The initial estimate for k_{exch} is a very large value that forces the boundary compositions to the equilibrium value by generating a large flux across the phase boundary in response to any non-zero value of $\Delta\mu$. Of course, too large a value of k_{exch} will generate a numerical instability at the boundary, so in practice it cannot be infinite, but it can be large enough to force a close approach to equilibrium at the phase boundary. Subsequent model iterations will explore whether the data require disequilibrium at the boundary by decreasing k_{exch} until it affects the results.

Preliminary Results & Future Work

Development of the model framework is in progress. At the time of writing, implementation of the original numerical method has been completed. Initial test cases reveal both working components of the model as well as necessary modifications to the methods described above. Figure 3.3 shows several frames of the time sequence for a simulation of the isothermal experiments completed in Chapter 2.

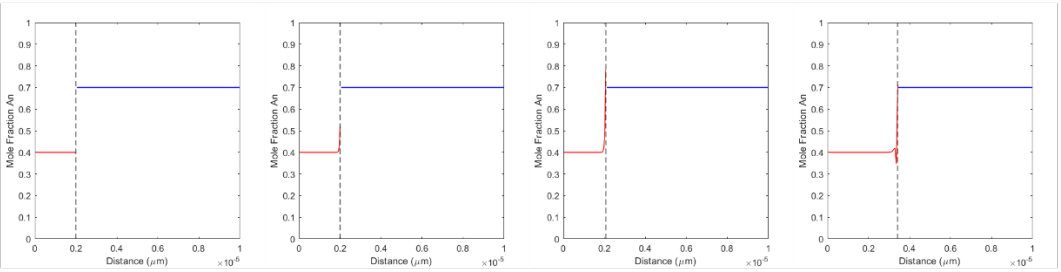

Figure 3.3. *Simulation of isothermal hold experiment.* A time sequence of the 1400°C isothermal hold experiment completed in Chapter 2 is shown, over the course of 1 minute. Initial conditions of the system were 0.4 An in the melt (red) and 0.7 An in the solid (blue), with $k_{exch} = -10^{-11}$ and $k_{growth} = 10^{-8}$. The moving boundary is shown with the dotted line in each frame.

The time sequence in Figure 3.3 demonstrates that the boundary is able to move as intended, shifting from x_b = 2 μm to x_b = 3.3 μm. However, there is a clear instability near the boundary in the melt. Figure 3.4 shows the subsequent time step a few seconds later, at which the concentration becomes unphysical (below 0% An); time steps after the one shown generate concentration values at even larger orders of magnitude, seemingly unable to stabilize. Currently, the scale of the velocity and chemical exchange terms are dictated by various combinations of the chemical potentials of the components. Δg and $\Delta \mu$ values range from zero to 10^6 depending on the level of disequilibrium at the boundary. However, the moving boundary is defined as $x_b^{t+\Delta t} = x_b^{t} + V\Delta t$ requiring the value $V\Delta t$ to always be within the range of the frame of reference (order ~10^1 μm dimensionalized, 0 to 1 nondimensionalized) to provide a physically meaningful result. Testing of various combinations of k_{exch} and k_{growth} have shown that treating them as constant values is insufficient to describe chemical behavior – once the concentration in a phase becomes unphysical, it is a positive feedback loop, unable to recover to physically meaning concentrations between 0 and 1. Therefore, the formulation of k_{exch} and k_{growth} require corresponding scaling functions that are able to adapt to the differences in thermodynamic values each time step.

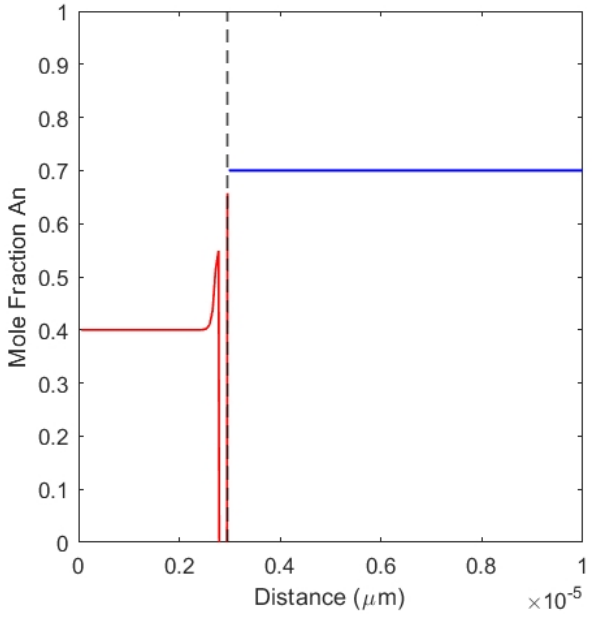

Figure 3.4. *Instability at the boundary*. Instability at the melt is a positive feedback loop, unable to recover once it surpasses physical values between 0 and 1 mole fraction anorthite.

Ongoing development is focused on the formulation of the appropriate scaling functions for k_{exch} and k_{growth}. Initial tests that scale k_{exch} and k_{growth} relative to their maximum possible values at a given temperature show more promising results with regard to stability at the boundary, but alternative functions for the two variables are being explored as well.

References

Albaréde, F. (1996). *Introduction to Geochemical Modeling*. Cambridge University Press.

Asimow, P. D., & Ghiorso, M. S. (1998). Algorithmic modifications extending MELTS to calculate subsolidus phase relations. In *American Mineralogist* (Vol. 83). http://pubs.geoscienceworld.org/msa/ammin/article-pdf/83/9-10/1127/3613708/1127.pdf

Bowen, N. L. (1913). The melting phenomena of plagioclase feldspars. *American Journal of Science*, *35*, 577–599.

Crank, J. (1975). *The Mathematics of Diffusion* (2nd ed.). Oxford University Press.

Fogel, R. A., & Rutherford, M. J. (1995). Magmatic volatiles in primitive lunar glasses: I. FTIR and EPMA analyses of Apollo 15 green and yellow glasses and revision of the volatile-assisted fire-fountain theory. *Geochimica et Cosmochimica Acta*, *59*(1), 201–215. https://doi.org/10.1016/0016-7037(94)00377-X

Ghiorso, M. S., Hirschmann, M. M., Reiners, P. W., & Kress, V. C. (2002). The pMELTS: A revision of MELTS for improved calculation of phase relations and major element partitioning related to partial melting of the mantle to 3 GPa. *Geochemistry, Geophysics, Geosystems*, *3*(5), 1–35. https://doi.org/10.1029/2001gc000217

Ghiorso, M. S., & Sack, R. O. (1995). Chemical mass transfer in magmatic processes IV. A revised and internally consistent thermodynamic model for the interpolation and extrapolation of liquid-solid equilibria in magmatic systems at elevated temperatures and pressures. *Contributions to Mineralogy and Petrology*, *119*(2–3), 197–212. https://doi.org/10.1007/BF00307281

Grose, C. J., & Afonso, J. C. (2019). Chemical disequilibria, lithospheric thickness, and the source of ocean island basalts. *Journal of Petrology*, *60*(4), 755–790. https://doi.org/10.1093/petrology/egz012

Grove, T. L., Baker, M. B., & Kinzler, R. J. (1984). Coupled CaAl-NaSi diffusion in plagioclase feldspar: Experiments and applications to cooling rate speedometry. *Geochimica et Cosmochimica Acta*, *48*(10), 2113–2121. https://doi.org/10.1016/0016-7037(84)90391-0

Gualda, G. A. R., Ghiorso, M. S., Lemons, R. V., & Carley, T. L. (2012). Rhyolite-MELTS: A modified calibration of MELTS optimized for silica-rich, fluid-bearing magmatic systems. *Journal of Petrology*, *53*(5), 875–890. https://doi.org/10.1093/petrology/egr080

Jennings, E. S., & Holland, T. J. B. (2015). A simple thermodynamic model for melting of peridotite in the system NCFMASOCr. *Journal of Petrology*, *56*(5), 869–892. https://doi.org/10.1093/petrology/egv020

Keller, T., & Katz, R. F. (2016). The role of volatiles in reactive melt transport in the asthenosphere. *Journal of Petrology*, *57*(6), 1073–1108. https://doi.org/10.1093/PETROLOGY/EGW030

Kogiso, T., Hirschmann, M. M., & Reiners, P. W. (2004). Length scales of mantle heterogeneities and their relationship to ocean island basalt geochemistry. *Geochimica et Cosmochimica Acta*, *68*(2), 345–360. https://doi.org/10.1016/S0016-7037(03)00419-8

Lasaga, A. C., & Kirkpatrick, R. J. (1981). *Kinetics of Geochemical Processes* (8th ed.). Mineralogical Society of America.

Liang, Y. (2003). Kinetics of crystal-melt reaction in partially molten silicates: 1. Grain scale processes. *Geochemistry, Geophysics, Geosystems*, *4*(5). https://doi.org/10.1029/2002GC000375

Liang, Y., & Liu, B. (2016). Simple models for disequilibrium fractional melting and batch melting with application to REE fractionation in abyssal peridotites. *Geochimica et Cosmochimica Acta*, *173*, 181–197. https://doi.org/10.1016/j.gca.2015.10.020

Qin, Z. (1992). Disequilibrium partial melting model and its implications for trace element fractionations during mantle melting. *Earth and Planetary Science Letters*, *112*(1–4), 75–90. https://doi.org/10.1016/0012-821X(92)90008-J

Rudge, J. F., Bercovici, D., & Spiegelman, M. (2011). Disequilibrium melting of a two phase multicomponent mantle. *Geophysical Journal International*, *184*(2), 699–718. https://doi.org/10.1111/j.1365-246X.2010.04870.x

Saal, A. E., Hauri, E. H., Cascio, M. Lo, Van Orman, J. A., Rutherford, M. C., & Cooper, R. F. (2008). Volatile content of lunar volcanic glasses and the presence of water in the Moon's interior. *Nature 2008 454:7201*, *454*(7201), 192–195. https://doi.org/10.1038/nature07047

Spiegelman, M., & Elliott, T. (1993). Consequences of melt transport for uranium series disequilibrium in young lavas. *Earth and Planetary Science Letters*, *118*(1–4), 1–20. https://doi.org/10.1016/0012-821X(93)90155-3

Spiegelman, M., & Kenyon, P. (1992). The requirements for chemical disequilibrium during magma migration. *Earth and Planetary Science Letters*, *109*(3–4), 611–620. https://doi.org/10.1016/0012-821X(92)90119-G

Tinker, D., & Lesher, C. E. (2001). Self diffusion of Si and O in dacitic liquid at high pressures. *American Mineralogist*, *86*(1–2), 1–13. https://doi.org/10.2138/AM-2001-0101

Tirone, M., & Sessing, J. (2017). Petrological geodynamics of mantle melting I. Alphamelts + Multiphase flow: Dynamic equilibrium melting, method and results. *Frontiers in Earth Science*, *5*, 273811. https://doi.org/10.3389/FEART.2017.00081/BIBTEX

Zhang, Y. (2008). *Geochemical Kinetics*. Princeton University Press.

Chapter 4

COPPER ISOTOPE RATIOS IN SERUM DO NOT TRACK CANCEROUS TUMOR EVOLUTION, BUT ORGAN FAILURE

Miaou, Emily, and François L.H. Tissot. Copper isotope ratios in serum do not track cancerous tumor evolution, but organ failure. In: *Metallomics* 15.11 (2023): mfad060. DOI: 10.1093/mtomcs/mfad060

Abstract

Relative to healthy controls, lighter copper isotopic compositions have been observed in the serum of breast cancer and end-stage liver disease patients, raising the possibility that Cu isotope ratios could be used as a tracer for disease progression. Here, we assess the potential of natural Cu isotopic variations (expressed as δ^{65}Cu) as diagnostic tools for cancer progression and/or liver failure by performing a first-order analysis of Cu isotopic cycling in the human body. Using a box model, we simulate the kinetics of Cu mass transfer throughout significant reservoirs in the body, allowing isotopic fractionation to occur during Cu uptake/release from these reservoirs. With this model, we determine under which conditions the serum δ^{65}Cu values would reflect perturbation related to cancer growth and/or liver failure at a level resolvable with modern mass spectrometry. We find that tumor growth alone is unable to explain the light isotopic signature observed in serum. Instead, we find that metabolic changes to the liver function resulting in a ~1 ‰ isotope fractionation during Cu uptake from the blood into the liver can readily explain the long-term serum isotopic shift of ~0.2 ‰ observed in cancer patients. A similar fractionation (~1.3 ‰) during Cu uptake into the liver also readily explains the –1.2 ‰ shift observed in the serum of cirrhosis patients with ascites, suggesting a potentially common driver of isotopic fractionation in both cases. Using this model, we then test hypotheses put forward by previous studies and begin to probe the mechanisms behind the measured isotopic compositions.

Introduction

Stable isotopes are formidable tracers of physico-chemical processes involving mass transfer at all scales, capable of unraveling the details of galactic chemical evolution, planetary differentiation, human migrations, or mineral crystallization (Holland and Turekian 2014). In the late 1990s, the advent of the Multi-Collector Inductively Coupled Plasma Mass Spectrometer (MC-ICP-MS) finally made possible high-precision isotopic characterization of metabolically critical transition metals (*e.g.*, Fe, Cu, Zn) in blood, serum, and other medically relevant samples (Maréchal, Télouk, and Albarède 1999). Pioneering studies in this still-emerging field, named *isotope metallomics* (Albarède, Télouk, and Balter 2017; Mahan et al. 2020), have since documented significant isotopic variability in both healthy patients and patients with diseases affecting organs in which transition metals play a fundamental metabolic role (*e.g.*, breast cancer/liver disease/Alzheimer's for Cu (Balter et al. 2015; Bondanese et al. 2016; Van Campenhout et al. 2020; Costas-Rodríguez et al. 2015, 2019; Flórez et al. 2018; Lauwens et al. 2016; Moynier et al. 2020; Télouk et al. 2022; Télouk et al. 2015), hereditary hemochromatosis for Fe (Van Heghe et al. 2013; Krayenbuehl et al. 2005), breast cancer/Alzheimer's for Zn (Larner et al. 2015; Moynier et al. 2020; Sullivan et al. 2021), osteoporosis for Ca (Channon et al. 2015; Eisenhauer et al. 2019; Heuser and Eisenhauer 2010; Morgan et al. 2012; Rangarajan et al. 2018; Shroff et al. 2021; Skulan et al. 2007; Skulan and DePaolo 1999)).

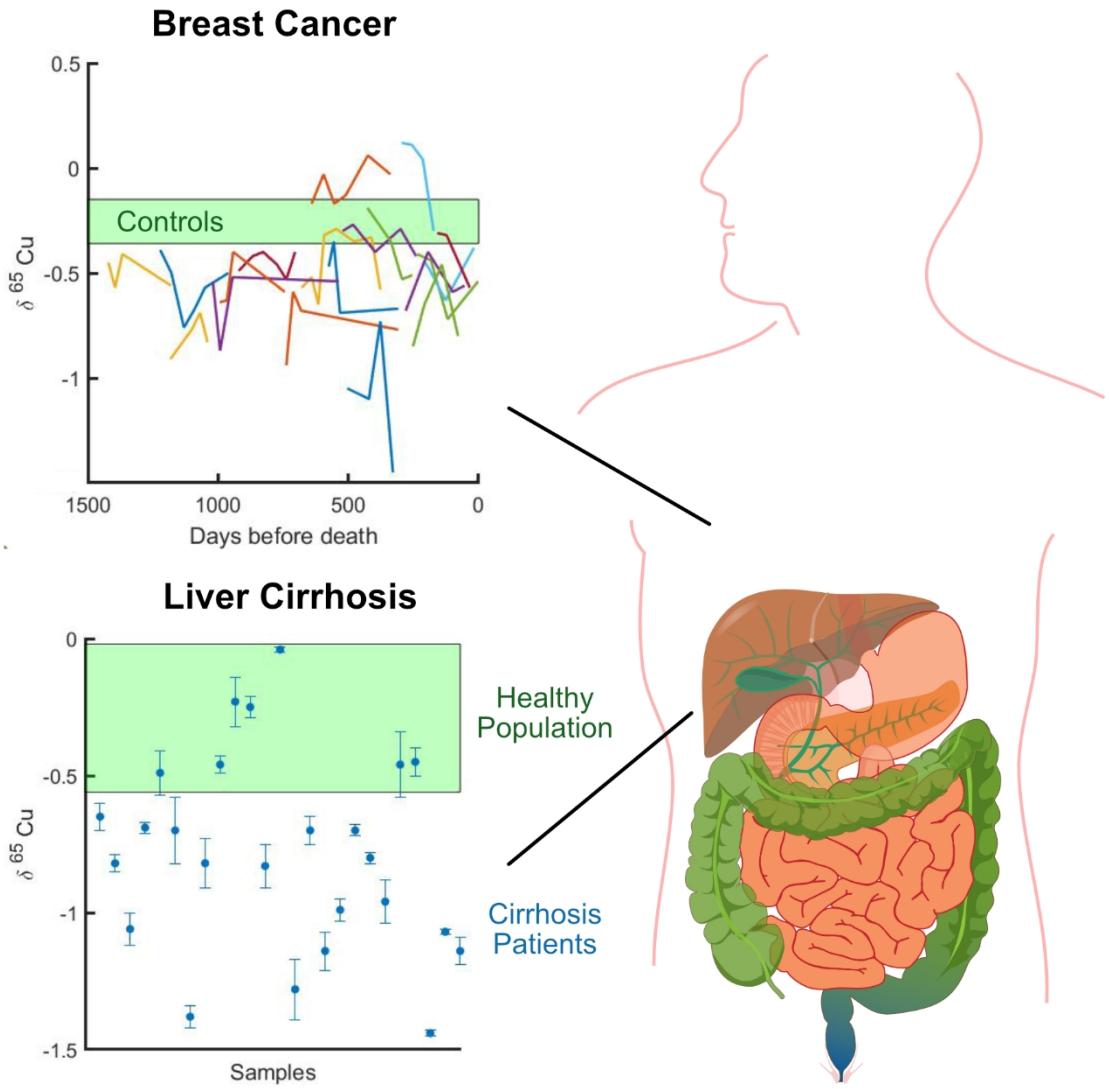

Figure 4.1. Serum copper isotopic compositions in the body. Existing mapping studies have shown consistently lower Cu isotopic compositions in the serum of breast cancer (top) and liver cirrhosis (bottom) patients relative to healthy controls. Breast cancer serum Cu isotopic values are replotted from Télouk, et al. (2015). Liver cirrhosis serum Cu isotopic values are from Costas-Rodríguez et al. (2015).

Copper, in particular, has been the focus of sustained attention. Indeed, the average copper isotope composition ($^{65}Cu/^{63}Cu$ ratio, hereafter expressed in permil

notation as δ^{65}Cu) was found to be significantly lower in the serum of breast cancer patients relative to healthy controls (Télouk et al. 2015). In hepatocellular carcinoma (HCC) patients, red blood cells have been shown to exhibit lower δ^{65}Cu values relative to those of healthy patients, while cancer tissue displays δ^{65}Cu values ~0.5 ‰ higher than surrounding healthy tissue (Balter et al. 2015). Furthermore, end-stage liver disease patients have serum Cu isotopic compositions that span a larger range of values compared to healthy controls, and are on average lower by ~0.6 ‰ (Costas-Rodríguez et al. 2015). These initial results led to optimism that such signatures could be introduced as a novel method of diagnosing or characterizing their respective diseases (Figure 4.1) (Balter et al. 2015; Costas-Rodríguez et al. 2015; Télouk et al. 2015). In recent years, additional studies have revealed a more complex picture, where both the mechanisms behind these isotopic variations and their sensitivity as potential biomarkers have been the subject of debate (Bondanese et al. 2016; Van Campenhout et al. 2020; Costas-Rodríguez et al. 2019; Flórez et al. 2018; Lauwens et al. 2016; Télouk et al. 2022). For instance, Bondanese et al. (2016) have proposed that hypoxic tumor environments can explain the observed Cu isotopic fractionation in HCC, bringing to light the potential broader impacts of oxidative stress in fractionation. Building on these results, Télouk et al. (2022) have proposed that the bimodal nature of Cu isotopic shifts in the serum of liver disease patients reflects a switch in resistance of hepatic tissues to oxidative stress, in turn leading to development of HCC. These studies warrant exploration of the relative magnitudes of impact that various factors can have on a patient's serum Cu isotope composition.

In light of these findings, this study seeks to build a quantitative framework to assess the potential for Cu isotope ratios to act as a diagnostic tool for disease onset and/or evolution and to probe the mechanisms behind the serum Cu isotope variations observed in humans. To determine the feasibility of using Cu isotope ratios as a biomarker, we must first ask the question, *"what makes an ideal medical diagnostic tool?"* It should satisfy the following general criteria to act as a pragmatic, competitive option:

(1) samples may be collected with a simple procedure,

(2) sample processing and measurement methods should be consistent and efficient,

(3) signatures must be resolvable by the instrument of choice, and

(4) signatures should appear and respond rapidly to the onset or evolution of the disease.

Point (1) is easily addressed, as much of the existing Cu isotope data primarily comes from serum samples, which are collected through routine wellness check procedures. With regard to Point (2), chemical processing methods for high-yield Cu separation and measurement from samples are well-documented in the literature and may be applied (Archer and Vance 2004; Bermin et al. 2006; Borrok et al. 2007; Jeong, Ra, and Choi 2021; C. Maréchal and Albarède 2002; C. N. Maréchal, Télouk, and Albarède 1999; Mason et al. 2004a, 2004b; Peel et al. 2007; Sossi et al. 2015; Sullivan et al. 2020; Yang et al. 2018). A current limitation, however, is that existing methods tend to require experienced users and are most commonly applied to small sample batches. Because many of the methods were designed for applications in research, they are currently not scalable to the needs of the medical field. As a result, they must be streamlined to focus on higher throughput for efficiency before this point is fulfilled. Points (3) and (4) are closely linked and are the focus of this study; given the difference in median serum Cu isotopic composition of healthy individuals relative to those with cancer or liver cirrhosis, the key is to determine how early the signature surpasses the instrument resolution threshold, and whether this shift occurs early enough in the disease progression to be a useful diagnostic tool. At this writing, the typical analytical uncertainty of δ^{65}Cu using state-of-the-art methods is ~ ±0.05 ‰, so the smallest measurable deviation from a control is ~ 0.1 ‰. We will primarily focus on exploring the possibility of signature detection given the restrictions of this current framework. In later sections, we also consider possible changes in these conclusions with future technological improvement.

A challenge to any quantitative assessment of the potential for Cu isotope ratios to act as tracers of disease is the limited knowledge of the mechanisms driving Cu isotope fractionation in the human body. Performing a first-order analysis of the system, however, circumvents the need to account for all the individual molecular mechanisms while still providing quantitative results for interpretation. This method is well-established and has been used successfully by others in the metallomics field to better understand trace metal isotopic systems, such as zinc in the human body (Jaouen et al. 2019). Here, we thus quantitatively model the human body to explore some of the unanswered questions regarding trends seen in previous Cu isotope studies, such as:

(i) When can Cu isotopic fractionation due to tumor growth alone in an otherwise healthy body create measurable serum isotopic differences?

(ii) When does complete liver failure (*e.g.*, from HCC) cause measurable Cu isotopic differences in serum?

(iii) How may the isotopic fractionation of tissue affected by metabolic changes linked to the progression of cancer or liver disease (*e.g.*, oxidative stress) be reflected in serum Cu composition?

Copper in the Body

Copper is an essential trace element and the third most abundant transition metal in the human body (Jomova et al. 2022), where it exists in two main oxidation states (Cu^{+} and Cu^{2+}). It is versatile for performing biochemical redox reactions, acting as a useful cofactor in many enzymes (*e.g.*, ceruloplasmin, superoxide dismutase, lysyl oxidase), though it simultaneously poses a risk for toxicity if improperly regulated by the body. As such, Cu is almost always bound to proteins or peptides, and “free” or unbound copper is uncommon (Ramos et al. 2016).

The total mass of Cu in the average healthy adult body is ~100 mg. Distribution of this mass between its main reservoirs (Table 4.1) have been well established through

nutritional studies (see review in (Ross et al. 2012)). Copper enters the body through food consumption, with the recommended Cu intake for a healthy adult being ~1 mg/day (*i.e.*, ~100 days residence time) (Russell et al. 2001). Absorption of the nutrient occurs through the small intestine, where it binds to albumin and macroglobulins in the blood to be carried to the liver. The liver acts as the primary storage and regulatory compartment. Hepatic cells synthesize ceruloplasmin (Cp, the primary Cu protein carrier in the blood), and copper is bound to Cp or other proteins while circulating the body for delivery to various organs. Excess Cu is filtered out by the kidneys or released from the liver into the gallbladder, after which Cu exits the body through urine or fecal matter.

Organ	**Mass of Cu used in Computation (mg)***
Liver	10
Blood	6
Bones	40
Muscle	23
Brain	8
Other	13

Table 4.1. Cu distribution in organs of the human body.

***Cu mass distribution values are taken from Modern Nutrition in Health and Disease, 11th ed. (Ross et al. 2012).

Though elemental Cu is already well-established as an essential trace metal for humans, much less is known about its stable isotopes and their behaviors in the body. A few select studies have approached Cu fractionation on a molecular level with a combination of experiments and first-principles calculations to quantify the fractionation of individual Cu-interacting proteins (Cadiou et al. 2017; Selden et al. 2022; Tennant, Rauk, and Wieser 2017). Such investigations are necessary steps toward achieving a mechanistic understanding of the isotopic effects, but the rate of development of these understandings is relatively slow for several reasons. There are over 50 proteins in the human Cu proteome that may contribute to net fractionation effects and would need to be characterized (Blockhuys et al. 2017); first principles

calculations are time-intensive and computationally expensive, requiring a relatively specialized skillset, while *in vitro* experiments involving individual protein expression, purification, and analyses are often difficult and time-consuming, depending on the stability and other chemical characteristics of the molecules in question.

Considering these uncertainties, this study takes a macroscopic approach to investigate Cu in cancer: whole-body Cu behavior is quantified using well-established values from nutritional literature, while assumptions about molecular-level relationships between Cu and cancer are non-essential and thus limited.

Methods

We aim to model and observe three main scenarios (see next Section for details). In the first scenario, a tumor begins to grow in an otherwise healthy body, participating in the uptake and release of Cu to aid its proliferation. Because tumor behavior differs depending on cancer type, location, and stage, our system has been defined as simulating early-stage breast cancer growth, forming a single tumor mass in the body. This specific system was selected for several reasons. First, modeling cancer allows us to make direct comparisons between our results and those of the existing studies (Balter et al. 2015; Bondanese et al. 2016; Flórez et al. 2018; Télouk et al. 2022; Télouk et al. 2015). Second, breast cancer in its early stages does not directly or immediately affect the function of important Cu reservoirs, in contrast, for instance, to hepatic cancer affecting the liver, which is the major Cu regulator of the body. This allows us to easily differentiate between the effects of the tumor versus those of another reservoir when we built the model. Third, drawing conclusions on whether isotopic signatures can be diagnostic tools depends on the behavior of early-stage cancer growth and whether it translates into a measurable signal; modeling metastatic behavior would be less useful for this purpose. In the second scenario, liver-only fractionation is considered. This type of fractionation may represent several physical cases that could afflict this major reservoir including

various stages of liver disease, from nonalcoholic fatty liver disease (NAFLD) to liver cirrhosis or even HCC. Finally, the last scenario broadly simulates altered isotopic fractionation of originally healthy tissue, due to potential effects from metabolic responses to disease (*e.g.*, oxidative stress), to explore the sensitivity of serum Cu isotopic composition as a possible prognostic marker.

To examine the role of major elemental reservoirs in the body and the fluxes between them, we built a multi-box system. The components of interest are as follows: (1) a fixed copper influx from daily food intake according to recommended health standards, (2) the blood, which acts as a conduit through which Cu is able to be transported throughout the body to other reservoirs, (3) healthy tissue, such as bone and muscle, that contain a large proportion of the body's copper but do not directly interact with the cancerous tumor, (4) the tumor itself, (5) the liver, which acts as the storage and regulatory compartment for Cu, and (6) the gallbladder, which we effectively treat as a waste accumulation reservoir for any Cu outflux from the body. Our treatment of the gallbladder is due to the expectation that almost all Cu released to the gallbladder from the liver is excreted via biliary incorporation into feces (Ross et al. 2012; Turnlund 1998). As such, the "gallbladder" compartment is not considered in the analysis of diagnostic potential, as it is not expected to influence any of the other reservoirs. All Cu flows between reservoirs were treated as first-order reactions, the precedent for which is established by existing nutritional studies (Dunn, Green, and Leach 1991; Turnlund 1998). With the exception of unidirectional nutrient flow from the food to the blood and the liver to the gallbladder, all other flows were allowed forward and back exchange to mimic realistic behavior of the circulatory system (Figure 4.2).

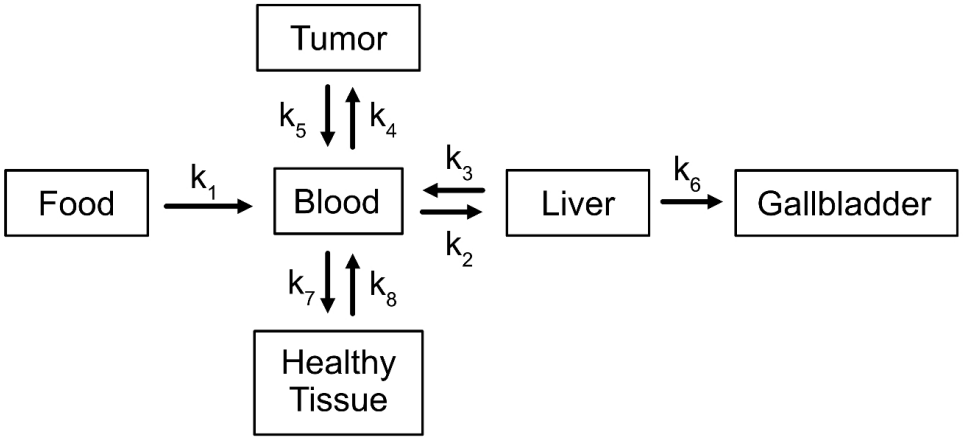

Figure 4.2. *Box model of major Cu reservoirs in the human body.* The six groups presented in the diagram represent the major reservoirs of interest participating in copper storage and transport, with the arrows representing the allowable Cu flows between them. First-order kinetic constants for fluxes in and out of each reservoir i, k_i, are scaled based on compartmental models from existing nutritional studies (Dunn et al. 1991; Turnlund 1998).

Two systems of ordinary differential equations (ODEs) were established to represent the elemental and isotopic mass balance of Cu in the body, using the general forms shown in Eqs. 4.1 and 4.2, respectively, modified from Albarède (1996).

$$\frac{dm_i}{dt} = -\sum_{j \neq i} k_{ij}\, m_i + \sum_{j \neq i} k_{ji}\, m_j \quad (4.1)$$

$$\frac{d(m_i R_i)}{dt} = R_i \sum_{j \neq i} k_{ij}\left(1 - \alpha_{ij}\right) + \sum_{j \neq i} k_{ji}\left(\alpha_{ji} R_j - R_i\right) \frac{m_j}{m_i} \quad (4.2)$$

In these equations, i and j are distinct reservoirs/organs of the body, m_i is the total mass of Cu in reservoir i, k_{ij} is the first order kinetic coefficient of mass transport from reservoir j to i. In Eq. 4.2, R_i is the $^{65}Cu/^{63}Cu$ ratio in reservoir i and α_{ij} is the fractionation factor of Cu transfer from reservoir j to i (*i.e.*, the composition of the material extracted toward reservoir i divided by the composition of parent reservoir j

). Specifically, the explicit ODEs for mass change in the blood, liver, tumor, and healthy tissue, respectively, are given in Eqs. 4.3–4.6 below:

$$\frac{dm_{blood}}{dt} = k_1 + k_3 m_{liver} - k_2 m_{blood} + k_5 m_{tumor} - k_4 m_{blood} + k_8 m_{healthy} - k_7 m_{blood} \quad (4.3)$$

$$\frac{dm_{liver}}{dt} = k_2 m_{blood} - k_3 m_{liver} - k_6 m_{liver} \quad (4.4)$$

$$\frac{dm_{tumor}}{dt} = k_4 m_{blood} - k_5 m_{tumor} \quad (4.5)$$

$$\frac{dm_{healthy}}{dt} = k_7 m_{blood} - k_8 m_{healthy} . \quad (4.6)$$

Similarly, the ODEs describing the change in isotopic composition of these reservoirs are given in Eqs. 4.7–4.10. In all cases, the kinetic constants are numbered according to Figure 4.2. The fractionation factors are numbered to represent the reservoirs in the same order as the kinetic constants (Table 4.2).

$$\frac{d\delta_{blood}}{dt} = \frac{1}{m_{blood}}\left(k_2\left(1-\alpha_2\right) + k_4\left(1-\alpha_4\right) + k_7\left(1-\alpha_7\right)\right) + \frac{k_1\left(\delta_1 m_{blood} - \delta_{blood}\right)}{m_{blood}} + k_3\left(\delta_3 m_{liver} - \delta_{blood}\right)\frac{m_{liver}}{m_{blood}} + k_5\left(\delta_5 m_{tumor} - \delta_{blood}\right)\frac{m_{tumor}}{m_{blood}} + k_8\left(\delta_8 m_{healthy} - \delta_{blood}\right)\frac{m_{healthy}}{m_{blood}} \quad (4.7)$$

$$\frac{d\delta_{liver}}{dt} = \frac{1}{m_{liver}}\left(k_3\left(1-\alpha_3\right) + k_6\left(1-\alpha_6\right)\right) + k_2\left(\alpha_2 m_{blood} - \delta_{liver}\right)\frac{m_{blood}}{m_{liver}} \quad (4.8)$$

$$\frac{d\delta_{tumor}}{dt} = \frac{1}{m_{tumor}}\left(k_5\left(1-\alpha_5\right)\right) + k_4\left(\alpha_4 m_{blood} - \delta_{tumor}\right)\frac{m_{blood}}{m_{tumor}} \quad (4.9)$$

$$\frac{d\delta_{healthy}}{dt} = \frac{1}{m_{healthy}}\left(k_8\left(1-\alpha_8\right)\right) + k_7\left(\alpha_7 m_{blood} - \delta_{healthy}\right)\frac{m_{blood}}{m_{healthy}} \quad (4.10)$$

To constrain the values of the kinetic constants (Table 4.2), a careful examination of the sparse literature data was done. First, the dietary intake of Cu for a healthy adult was set. Though the recommended daily intake value is ~1 mg Cu, only approximately 0.8 mg of it is absorbed by the intestine and enters the circulatory system; therefore we use k_1 = 0.8 mg/day (Ross et al. 2012; Russell et al. 2001). The

other kinetic constants controlling Cu flow between the blood and relevant organs/tissues were constrained by two conditions. First, Cu reservoirs must return to expected steady-state mass values after an imposed perturbation. The Cu inventory of organs/tissues in a healthy body are relatively well-known, and this condition represents the homeostatic response of a healthy body to small fluctuations in Cu (*e.g.*, variations in diet) (Linder 2013; Ross et al. 2012). Second, the rate at which reservoirs responded to perturbations had to be consistent with the available experimental data (Turnlund 1998). Approximate values satisfying the conditions for kinetic constants were drawn from existing nutritional studies that utilized mice for compartmental modeling of short- and long-term Cu turnover in the body (Levenson and Janghorbani 1994; Turnlund 1998). The values were then tuned in small increments to ensure the stability of the system, such that it would respond to deviations or perturbations from the expected mass of each reservoir to re-equilibrate it to healthy, steady-state values (*e.g.*, if the mass of Cu is suddenly raised to 8 mg in the blood due to a Cu-rich diet, the model would reflect the body's attempt to lower it back to the healthy expected value of 6 mg). Figure 4.3a demonstrates the response to perturbation of Cu masses of each reservoir compared to steady state, and the ability of the system to recover over time and maintain homeostasis, while Figure 4.3b demonstrates that the model's short and long turnover timescales closely match existing studies (Levenson and Janghorbani 1994; Scott and Turnlund 1994).

Reservoir Transfer, ◆→◆	Rate Constants	Steady state values[1]	Fractionation Factor	Range of values considered[2]
Food → Blood	k_1	0.8	D_1	1

Blood → Liver	k_2	0.3	D_2	1-1.001
Liver → Blood	k_3	0.11	D_3	0.999-1
Blood → Tumor	k_4	0.00002	D_4	1-1.003
Tumor → Blood	k_5	0.00001	D_5	1
Liver → Gallbladder	k_6	0.081	D_6	1-1.001
Blood → Other Healthy Tissue	k_7	0.8	D_7	1
Other Healthy Tissue → Blood	k_8	0.06	D_8	0.997-1

Table 4.2. *Rate constants and fractionation factors for box model reservoirs.* [1] Steady state *k* values were approximated based on Cu half-life measurements in different organisms from Levenson & Janghorbani (1994).

[2] Possible fractionation factors were based on *ab initio* calculations of copper ion binding to amino acids in aqueous solution from Fujii et al. (2014) and Cadiou et al. (2017).

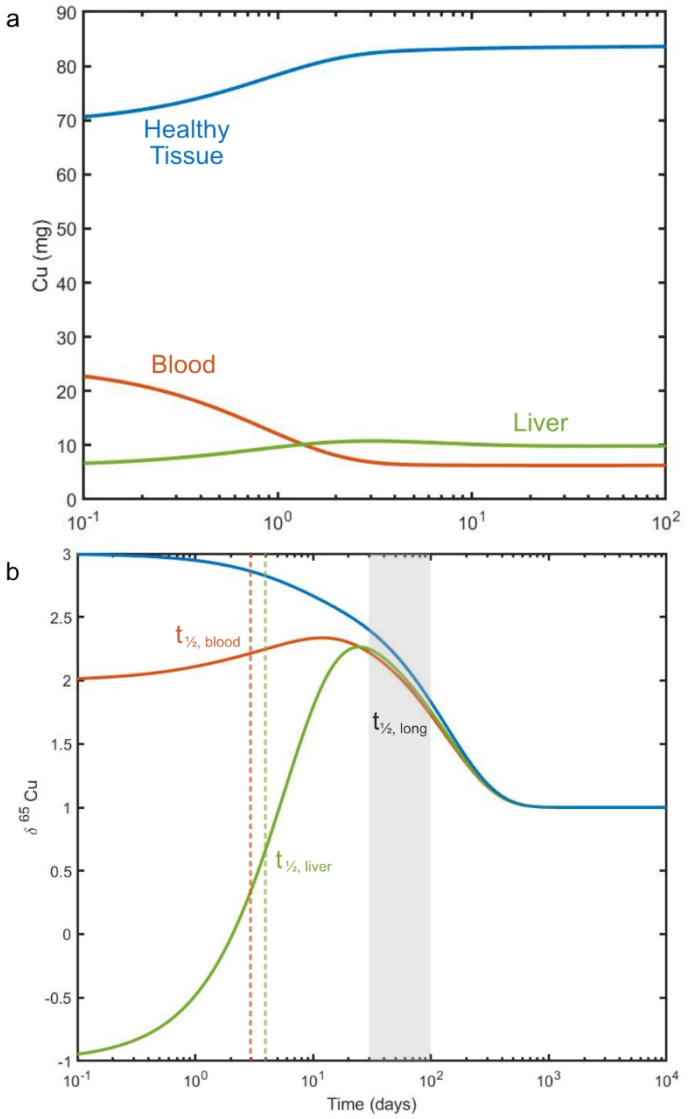

Figure 4.3. Model response to mass and isotopic perturbation. (a) Cu masses of each reservoir were strongly perturbed from expected steady state values, simulating the case of an intravenous injection of Cu. The reservoirs return to expected steady state Cu masses over time to maintain homeostasis, demonstrating the robustness of the model. (b) All reservoirs were initialized to random δ^{65}Cu values and allowed to return to steady state. All reservoirs in the system converge to the isotopic composition of the food input (δ^{65}Cu = 1 ‰) over time. Red and green dotted lines represent the expected short half-lives ($t_{1/2}$) of plasma and liver, respectively, presented in Levenson & Janghorbani (1994) and Scott & Turnlund (1994). These

short half-lives represent the expected immediate behavior to a perturbation. The grey band represents the range of expected half-lives of long-term Cu turnover ($t_{1/2,\,long}$) in the reservoirs from Levenson & Janghorbani (1994).

The next condition to be established was tumor growth behavior. Different subtypes of breast cancer have differing growth parameters, and approximate doubling times for primary breast cancer range extremely widely—from a few months to over a year (Förnvik et al. 2016; L. Heuser, Spratt, and Polk 1979). Furthermore, because many factors determine the spatial and temporal growth of tumors at different stages of its progression (*e.g.*, diffusion-limitation of nutrients, allowable space in the host, successful vascularization), the growth does not follow a simple exponential curve over time, contrary to what would be expected from uncontrolled cell division alone. Due to the variable and uncertain nature of tumor growth, we decided to use a linear growth model, which is one of several commonly used models for cancer development (Brú et al. 2003; Murphy, Jaafari, and Dobrovolny 2016). This type of growth most accurately characterizes tumor growth after the initial exponential replication phase but prior to metastasis, which is a time frame of interest for diagnostic purposes. The next step was to determine the rate of Cu uptake by the tumor to fuel its growth. The average amount of time a primary breast cancer tumor has been growing prior to detection ranges from 1 to 4 years (Spratt, Greenberg, Heuser 1986). In 2010, at time of detection, 67% of breast tumors were < 2.0 cm, with approximately 27% of these tumors falling in the 1–2 cm range, which is the upper bound for what is generally considered a "smaller" tumor (Welch et al. 2016). Assuming a density of 1 g/cm^3 for the cell, which is mainly composed of water, a spherical tumor with 2 cm diameter would weigh ~4.2 g. Measurements of Cu concentration in breast tumors range from 2 to 10 μg/g (wet mass basis) (Kuo et al. 2002; Margalioth, Schenker, and Chevion 1983). Therefore, a relatively fast-growing tumor (2 cm diameter growth over 1 year) would need to uptake and sequester ~0.04 mg Cu/year. This rate was taken as a first-order estimate for the slope of the linear growth curve and used to calibrate k_4 (= 0.00002 day^{-1}). This growth

rate reflects the most optimistic scenario for detection of a small tumor, *i.e.*, the faster the tumor grows, the quicker it sequesters Cu and may be detected by isotopic measurements. Changing this growth rate by one order of magnitude (higher or lower) also did not impact our conclusions (see next section).

For each scenario tested, the box model was initialized with steady-state values of Cu in each reservoir: 6 mg in the blood, 10 mg in the liver, and 84 mg in healthy tissue (Table 4.1). The fractionation factors were all set to $\alpha_{i,j} = 1$, indicating no fractionation between any of the reservoirs. At t = 0, the system was perturbed by the introduction of tumor growth, and a fractionation factor was applied to the reservoir of interest. A range of fractionation factors (Table 4.2) were considered for each scenario described below.

Scenarios and Results

We present a suite of computational test scenarios that draws from several studies and their experimental observations. All experimental studies referenced in this section reported δ^{65}Cu values using the international Cu isotopic standard NIST SRM 976. Delta notation is used as follows

$$\delta^{65}X = \left(\frac{R_{sample}}{R_{NIST\ SRM\ 976}} - 1 \right) \times 1000 \quad (4.11)$$

$$\Delta^{65}X(t) = \delta^{65}X(t) - \delta^{65}X(0) \quad (4.12)$$

for any given reservoir *i* at time *t*. Table 4.3 provides a summary of pertinent observations from the studies referenced in this section.

		Serum δ^{65}Cu (‰)

Literature Reference		Median or Mean	Range
Télouk et al. (2015)	Healthy/Control (n=30)	Median: -0.26	-0.80 to 0.05
	Breast Cancer (n=86)	Median: -0.52	-1.45 to 0.12
Van Campenhout et al. (2019)	Healthy/Control (n=22)	Median: -0.13 (males), -0.26 (females)	-0.49 to 0.05 (males), -0.46 to -0.08 (females)
	NAFL (n=10)	Median: -0.87	-1.01 to -0.32
Costas-Rodríguez et al. (2015)	Healthy/Control (n=29)	Mean: -0.29	-0.54 to -0.06
	Liver Cirrhosis (n=25)	Mean: -0.78	-1.44 to -0.04
Télouk et al. (2022)	Healthy/Control (n=105)	Median: -0.11	-0.63 to 0.28
	HCC (n=98)	Median: -0.51	-1.71 to 0.07
Lauwens et al. (2016)	ESLD, pre-LTx (n=32)	Median: -0.74	-1.45 to -0.40
	ESLD, 3mo post-LTx (n=32)	Median: -0.55	-1.54 to -0.18
	ESLD, 9mo post-LTx (n=17)	Median: -0.45	-1.27 to -0.09
Costas-Rodríguez et al. (2019)	Sham-operated Mice, 4w post-operation	Mean: -0.67	nr
	CBDL Mice, 4w post-operation	Mean: -1.14	nr

Table 4.3. *Parameters in "Scenarios and Results" section.* All experimental studies referenced in this section reported δ^{65}Cu values using the international Cu isotopic standard NIST SRM 976. nr = not reported. NAFL = non-alcoholic fatty liver, HCC = hepatocellular carcinoma, ESLD = end stage liver disease, LTx = liver transplantation, CBDL = common bile duct ligation

Tumor-only fractionation: To assess whether the Cu isotope composition of the blood and organs can be affected by the tumor growth, we considered a scenario where a

tumor appears in a body at steady-state, and an isotopic fractionation is associated with Cu uptake/release into the tumor. As can be seen in Figure 4.4, while the tumor composition directly reflects each of the applied fractionation factors, the blood, liver, and healthy tissue compositions are virtually unchanged, remaining at 0 ‰ for each of the cases. Sensitivity tests were performed on the tumor growth factor to gauge stability of the system under different scenarios, exploring a range of k_4 values spanning two orders of magnitude (0.00002-0.002 day^{-1}). Even at the maximum tumor growth rate tested with a 3‰ fractionation into the tumor, the drop in serum isotopic composition was < 0.05 ‰. This is because the absolute amount of Cu sequestered by the tumor is negligible compared to the body's Cu budget (mass of Cu in tumor is 0.012% of total body Cu, Figure 4.4b). The same limitation applies in the case where the Cu isotopic fractionation is associated with Cu release from the tumor. Thus, while the tumor composition is strongly fractionated from that of the blood (and by construction, the organs as well), the Δ^{65}Cu of the blood and other reservoirs due to the tumor are also negligible (-0.0005 ‰). Given the expected precision of approximately 0.1-0.2 ‰ referenced in this study, the differences in isotopic compositions of the blood due to tumor growth alone would be unresolvable.

Télouk et al. (2015) proposed that serum copper of cancer patients may become isotopically lighter compared to controls due to the Warburg effect: the increased usage of anaerobic glycolysis in cancer cells that can lead to higher concentrations of L-lactate in the cytosol. This lactate can bind to free Cu^{2+}, with the chelation reaction having a strong preference for ^{65}Cu over ^{63}Cu. Based on *ab initio* calculations, the equilibrium Cu isotope composition of Cu(II)(L-lact)(D-lact) is expected to be ~3‰ heavier than that of $Cu(I)(Cys)(H_2O)_4^{2+}$, which is representative of the Cu binding motif of ATP7A, one of the primary cellular transmembrane transporters of Cu. This results in isotopically heavy Cu being sequestered in the cytosol of cancer cells with lactate while ^{63}Cu is preferentially shuttled out to the bloodstream by ATP7A. While the chemistry of this hypothesis is promising, this scenario is equivalent to a Cu isotope fractionation associated solely with the tumor,

as only the Cu taken up and/or released by the tumor will be isotopically fractionated. As shown in Figure 4.4, such scenarios have a negligible impact on the blood Cu isotopic composition because of the overall negligible amount of Cu channeled through the tumor over time. Therefore, the Warburg effect, which applies primarily to the cancer mass, would be insufficient to explain the observed ~ 0.4 ‰ δ^{65}Cu offset in the serum of cancer patients vs healthy patients.

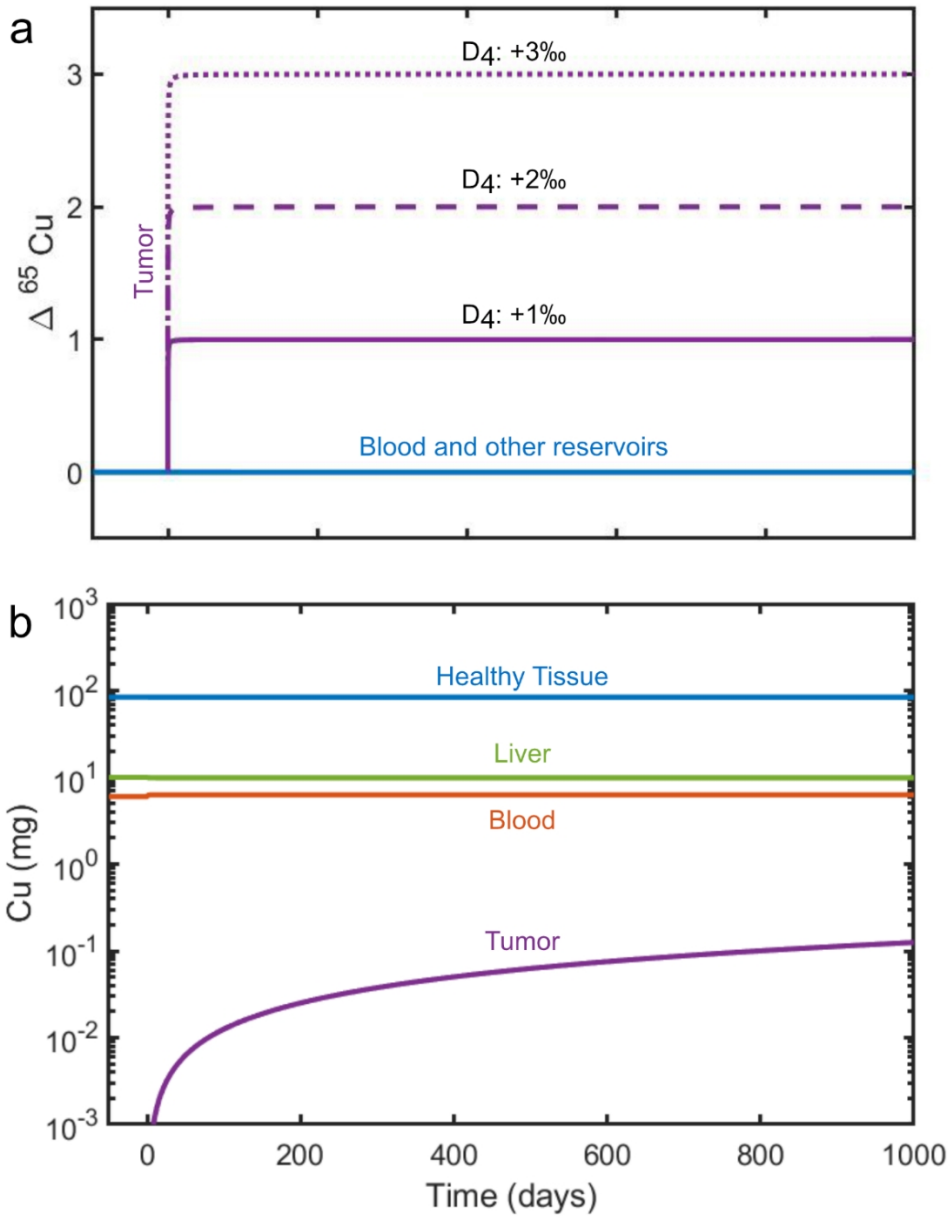

Figure 4.4. Effects of tumor-only Cu isotope fractionation as a function of time. (a) The composition of each reservoir is arbitrarily set to 0 per mil at the start of the simulation. At time equal 0 days, the tumor is introduced and allowed to grow. An isotopic fractionation is associated with Cu uptake in the tumor, *i.e.*, the fractionation factor D_4, was varied (see label on each curve), while all other reservoir interactions maintained a fractionation factor of 1. Cu isotope ratios are expressed as deviation

relative to t = 0, just before perturbation, *i.e.*, $\Delta^{65}Cu = \delta^{65}Cu(t) - \delta^{65}Cu(0)$. (b) The relative masses of Cu in each reservoir are plotted on a log scale. Cu mass in the tumor is orders of magnitude less than that of any other organ, resulting in its negligible contribution to the serum Cu isotopic composition, despite its ongoing exchange with the blood.

Liver-only fractionation: Considering the negligible effect the tumor alone has on the $\Delta^{65}Cu$ of other reservoirs, the question remains of which reservoirs *are* sufficiently large to induce a measurable change in serum $\delta^{65}Cu$. Because the liver is the primary regulator of copper and a fairly large reservoir (10% of the body's Cu budget), its dysregulation would be expected to have a noticeable effect on copper throughout the rest of the body. Some studies have investigated the effects of liver disease on serum $\delta^{65}Cu$ values at different stages, from non-alcoholic fatty liver disease (NAFLD) to HCC (Balter et al. 2015; Van Campenhout et al. 2020; Costas-Rodríguez et al. 2015; Lauwens et al. 2016; Télouk et al. 2022). Van Campenhout et al. (2020) found significantly (> 0.5 ‰) lower serum $\delta^{65}Cu$ value in NAFLD patients relative to healthy controls. Costas-Rodríguez et al. (2015) also observed a much lighter Cu isotope composition in the serum of patients with cirrhosis, which represents a worsening of NAFLD. More recently, Télouk et al. (2022) showed that patients with further progression to HCC also demonstrated a ~0.5 ‰ drop in serum $\delta^{65}Cu$ values relative to healthy controls. The consistent signature seen among these studies was used to guide the formulation of this scenario. There are two bounding cases by which Cu fractionation by the liver may result in isotopically lighter serum. The liver may preferentially uptake ^{65}Cu from the blood (Figure 4.5a) or preferentially release ^{63}Cu into the blood (Figure 4.5b). In stark contrast to tumor-only fractionation patterns, a fractionation of 1 ‰ in either scenario can change the composition of the blood, tumor, and other healthy tissues at a readily measurable level (> 0.5 ‰). This result demonstrates the order-of-magnitude of difference between organ-driven and tumor-driven fractionation. Intermediate cases in between these two extremes (*e.g.*, the liver preferentially taking heavy Cu from the blood but

also preferentially releasing heavy Cu back into the blood) would simply result in a dampening effect on the isotopic fractionations seen in Figure 4.5. The agreement between the experimental observations and our computational results further supports ideas presented in the aforementioned works that the observed serum Cu composition is due to liver disease. Our model also aligns with observations from Lauwens et al. (2016), which demonstrated that measurable changes in liver Cu isotopic fractionation (following liver-transplant) are reflected in serum composition over the timescale of 3-9 months, consistent with the largest changes occurring within ~200 days in the model.

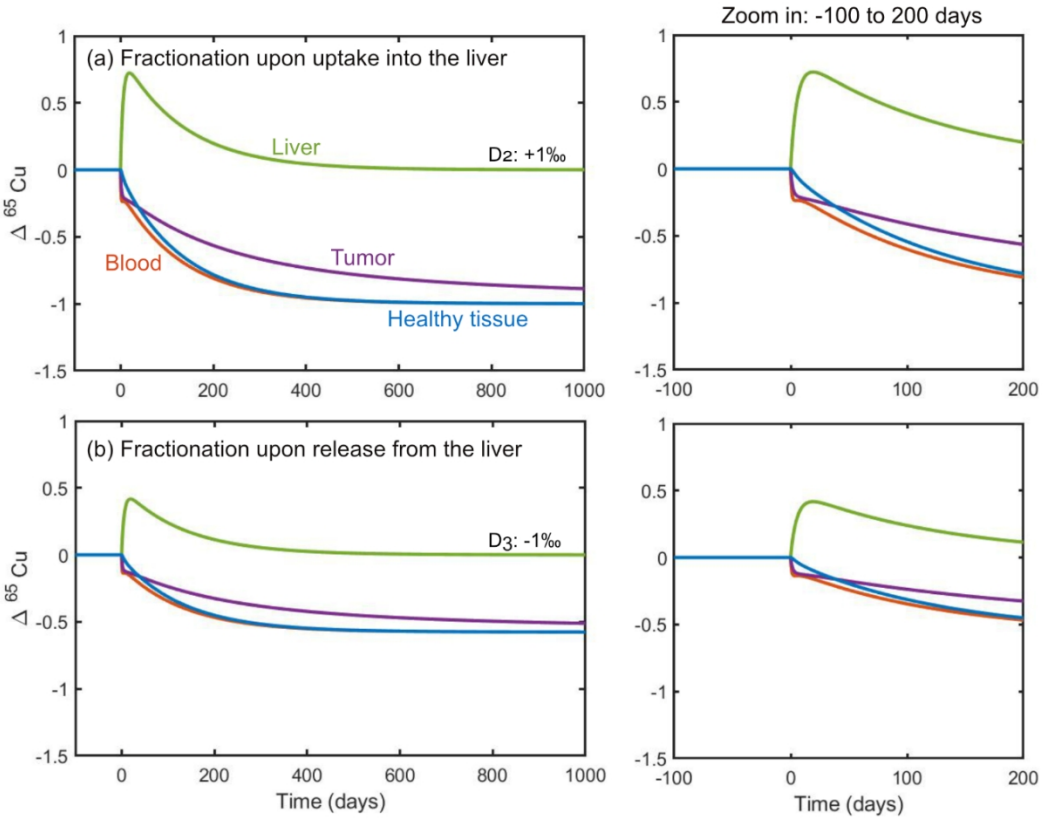

Figure 4.5. Effects of liver-only Cu isotope fractionation as a function of time. The composition of each reservoir is arbitrarily set to 0 per mil at the start of the simulation. At *t* = 0 days, the tumor is introduced and allowed to grow. Cu isotope

ratios are expressed as deviation relative to t = 0, just before perturbation, *i.e.*, $\Delta^{65}Cu = \delta^{65}Cu(t) - \delta^{65}Cu(0)$. (a) An isotopic fractionation associated with Cu uptake from the blood to the liver, *i.e.*, fractionation factor D_2, was set to 1.001 while all other reservoir interactions maintained a fractionation factor of 1. (b) An isotopic fractionation associated with Cu release from the liver to the blood, *i.e.*, fractionation factor D_3, was set to 0.999 while all other reservoir interactions maintained a fractionation factor of 1.

After seeing this repeated trend of light serum Cu isotopic composition in liver disease patients compared to healthy controls, Costas-Rodriguez et al. (2019) sought to determine more specifically the mechanism behind these results. Comparing mice populations that underwent sham operations vs. common bile duct ligation (CBDL), they observed that the overall Cu isotopic composition of the entire mouse body became ~0.6 ‰ lighter one month post-CBDL. They hypothesized that typical excretion from the liver to the bile is isotopically light, but the CBDL-operated mice were unable to preferentially release ^{63}Cu, resulting in its accumulation in the body. Figure 4.6 tests this hypothesis by comparing the difference in Cu isotopic composition ($\Delta^{65}Cu$) of reservoirs from a sham-operated mouse relative to a CBDL-operated mouse. The results of the model appear to match the measurements from [43] very well, with the liver becoming 1 ‰ lighter and the other reservoirs nearly 0.6‰ lighter. Once again, this scenario reinforces the idea that liver-only fractionation can create resolvable compositional changes in other reservoirs.

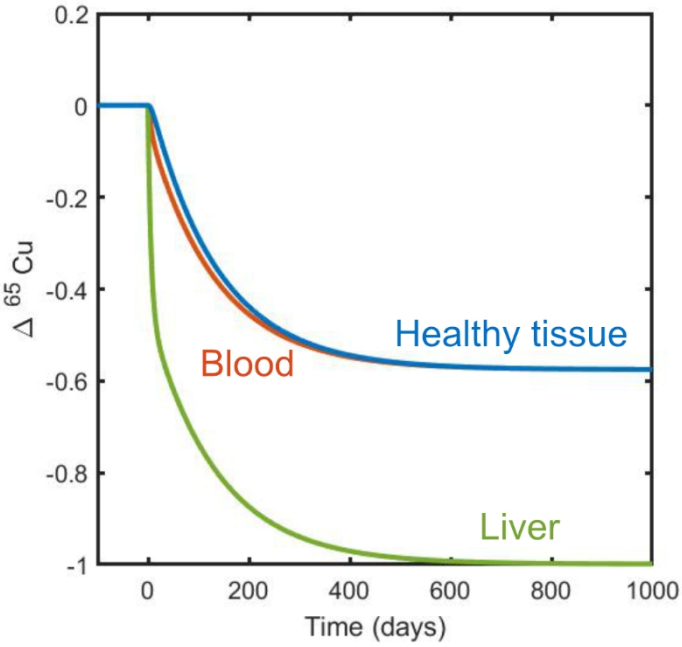

Figure 4.6. Effects of bile duct ligation in mice. Cu isotopic compositions of the reservoirs of the sham-operated mouse ($\delta^{65}Cu_{sham}$) are compared to Cu isotopic compositions of the reservoirs of the CBDL-operated mouse ($\delta^{65}Cu_{CBDL}$), with $\Delta^{65}Cu = \delta^{65}Cu_{CBDL} - \delta^{65}Cu_{sham}$. Bile duct ligation prevents release of ^{63}Cu from the liver to the bile relative to its regular healthy process, resulting in a decrease in the $\delta^{65}Cu$ of the liver. A fractionation factor of D_6 = 1.001 was used to describe this physical scenario, in accordance with the observed drop in liver isotopic composition from Costas-Rodriguez et al. (2019)

Alteration of healthy tissue metabolism/fractionation: A handful of studies investigated the mechanistic cause of serum Cu isotopic changes from liver disease and determined that oxidative stress is likely the primary contributing factor to the observed changes, with HepG2 cells under oxidative stress conditions exhibiting $\delta^{65}Cu$ values up to 2 ‰ heavier relative to those in normoxic environments (Bondanese et al. 2016; Flórez et al. 2018). If otherwise healthy cells are undergoing oxidative stress or inflammation due to any disease, including cancers or NAFLD/cirrhosis, a significant proportion of the total body mass could start to

exhibit altered metabolism, which may be reflected in the serum Δ^{65}Cu value at different stages of the disease progression, and to different degrees. This scenario broadly explores the physical phenomenon of the body undergoing increasing amounts of oxidative stress for any reason (*e.g.*, in response to cancer) by calculating what proportion of cells would need to be responding to oxidative stress to affect the blood isotopic compositions. To do so, the original healthy tissue reservoir is now divided into two: one representing healthy cells undergoing aerobic cellular respiration and the other representing formerly healthy cells metabolizing under oxidative stress conditions. Figure 4.7 demonstrates that greater than ~10 mass % of originally healthy tissue would have to be affected with a fractionation factor of +3 ‰ in order for the blood to undergo a > 0.2 ‰ drop in Δ^{65}Cu, which is a fairly large proportion of the body. If this is indeed the primary method by which the serum isotopic composition becomes lighter, only an extremely large or metastasized tumor could probably subject the body to such levels of oxidative stress to produce a detectable signature. At that point, it would very likely have already caused other serious symptoms to alert the patient to illness, and this type of isotopic analysis would not be required for detection and diagnosis. Notice that the result of this scenario is effectively an exacerbated case of the tumor-only fractionation: the blood composition recovers to its original state over time in this scenario. This contrasts with the liver-only fractionation scenario, where the blood Cu isotope composition reaches a new steady-state, different from its starting composition. This is because, in the liver-only fractionation scenario, the liver composition is not only affected by forward and backward exchange with the blood, but it is also siphoned away by the gallbladder. As a result, ^{65}Cu is continuously preferentially removed from the circulatory system, and the blood cannot recover back to its original composition. In contrast, when healthy tissue is affected and undergoes altered fractionation, the long-term effects on the blood are dampened by the continual back-exchange between the affected tissue and the blood. In short, any case in which a reservoir uptakes copper with a fractionation factor but subsequently also releases said composition back into the bloodstream will create this dampening effect, ultimately

resulting in the recovery of the blood back to its original (pre-perturbation) composition. Such scenarios cannot explain long terms changes on the blood Cu isotope compositions.

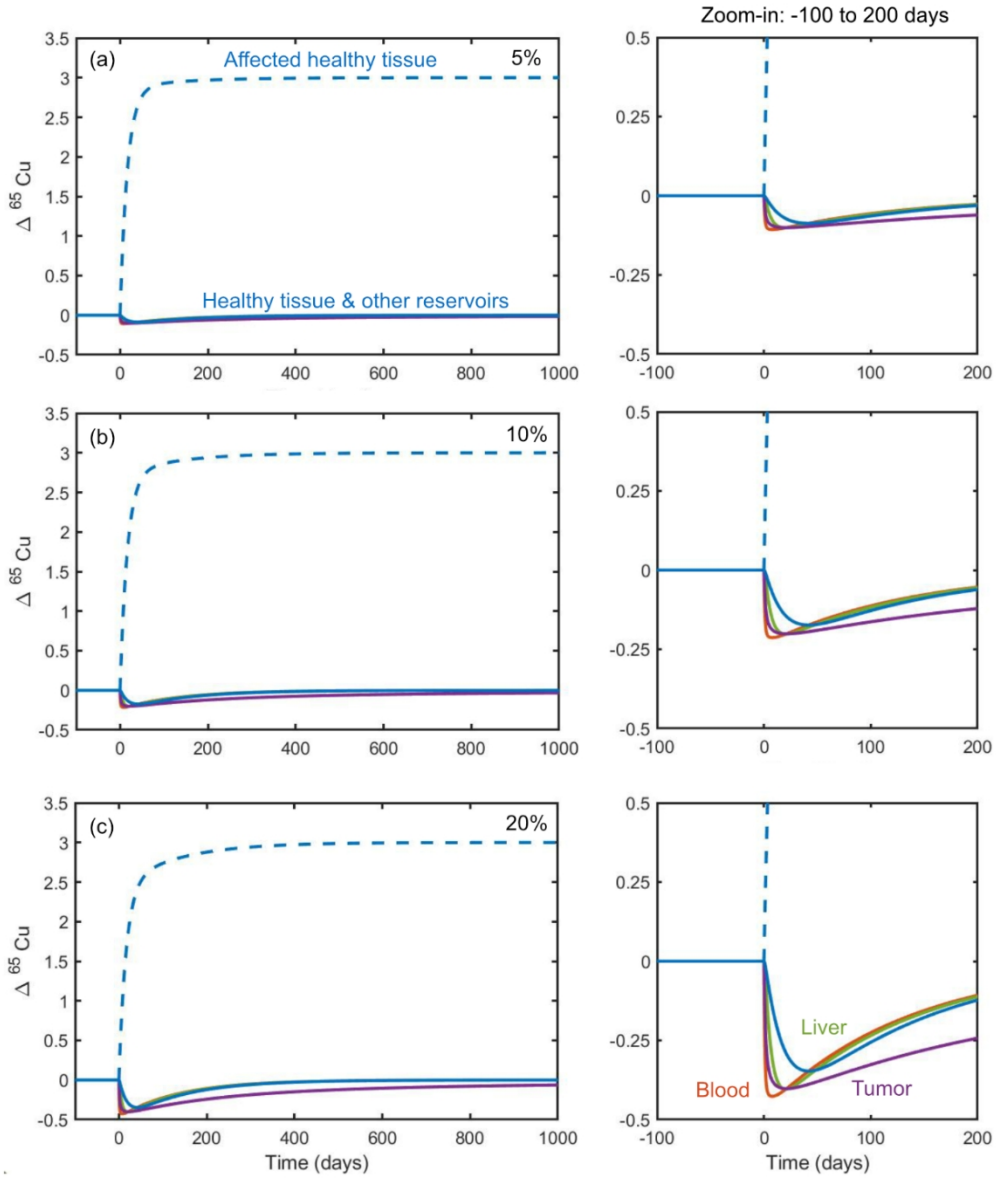

Figure 4.7. Isotopic fractionation effects of Cu chelation by lactate. A designated proportion of healthy tissue is affected by oxidative stress ("affected healthy tissue") and begins to undergo anaerobic glycolysis: (a) 5%, (b) 10%, (c) 20%. Cu isotope ratios are expressed as deviation relative to t = 0, just before perturbation, *i.e.*, Δ^{65}Cu

= $\delta^{65}Cu(t) - \delta^{65}Cu(0)$. A fractionation factor of 0.997 is used to describe the expected Cu chelation effect resulting from lactate production due to glycolysis, based on *ab initio* calculations from Télouk et al. (2015).

Discussion

Early studies raised interest in the idea that the offset in the serum Cu isotope composition of cancer patients could be used as a potentially powerful prognostic or diagnostic tool (Balter et al. 2015; Costas-Rodríguez et al. 2015; Télouk et al. 2015). In agreement with more recent studies (Bondanese et al. 2016; Van Campenhout et al. 2020; Costas-Rodríguez et al. 2015, 2019; Flórez et al. 2018; Télouk et al. 2022), our results point to a more complex picture. We find the simple proposal that Cu isotope ratios exclusively track tumor growth/evolution is not tenable. Indeed, the model demonstrates that the growth of a tumor in an otherwise healthy body cannot create a measurable (> 0.1 ‰) drop in blood Cu isotopic composition when any reasonable fractionation factor is imposed on the tumor (Figure 4.4).

Unlike the tumor, with its small size and Cu inventory, we find that a significantly larger reservoir can alter the blood composition. Exploration of the liver-only fractionation case shows that the imposition of a fractionation factor reflecting a +1 ‰ change in $\delta^{65}Cu$ uptake from the blood into the liver could successfully generate a corresponding –1 ‰ change in $\Delta^{65}Cu$ of the blood, which would certainly be measurable (Figure 4.5). This type of alteration in liver fractionation could describe the physical scenario of liver disease, considering that liver failure is also a common effect in mid- to late-stage cancer patients. This idea is supported by several recent experimental studies which found that liver disease of varying stages can result in a significant (0.5 ‰ or more) decrease in their serum isotopic compositions relative to healthy controls (Figure 4.1) (Van Campenhout et al. 2020; Costas-Rodríguez et al. 2015; Lauwens et al. 2016; Télouk et al. 2022). Considering oxidative stress as another possible source of isotopic fractionation on a large scale, we find that >10% of originally healthy tissue would have to impart a Cu

isotopic fractionation of ~ +1 ‰ during Cu uptake into the tissues to create a measurable effect in the blood (Figure 4.7). Further patient studies will be needed to monitor the isotopic variability induced by controls such as patient age or the degree of cancer progression, as well as clarify the specificity of these signatures.

For reasons previously discussed, our current calculations utilize a model of linear tumor growth. The integration of this model already provides clear results that can be directly compared to existing studies. However, in acknowledgment that different cancer types and subtypes exhibit different growth behaviors, other models warrant future exploration, such as exponential growth (Murphy, Jaafari, and Dobrovolny 2016). Though our calculations do not explicitly implement an exponential growth model, the tuning of the tumor growth rate, k_4, to be orders of magnitude larger (100x) than the expected rate provides a reasonably similar comparison to exponential growth behavior. Even in this scenario, tumor growth alone still failed to create a measurable Cu isotopic composition change in the blood, indicating the low dependency of our findings to the tumor growth behavior.

Ultimately, this study sought to utilize box modeling to quantitatively assess the potential for natural Cu isotopic variations in serum to act as a diagnostic tool for breast cancer and liver cirrhosis. Through modeling, we were able to determine whether Cu isotopic compositions satisfy criteria (3) and (4) set forth for a competitive medical diagnostic tool. Criteria (3) required that the drop in Cu isotopic composition of the patient serum must be resolvable by current MC-ICP-MS capabilities, which was determined to be largely dependent on the size of the reservoir causing the fractionation. With tumor-only fractionation, the serum composition is not sufficiently modified by the growth of the tumor due to its small size and Cu content relative to other reservoirs in the body. In contrast, isotopic fractionation associated with a larger reservoir, such as the liver or a large proportion (>10%) of healthy tissue undergoing severe oxidative stress, may cause an isotopic shift in the serum composition of the patient compared to healthy controls. Yet, only in the liver fractionation scenario does the serum composition shift permanently to a

new steady-state value that is lower than initial controls. In contrast, some percentage of healthy tissue with altered metabolic behavior affects the serum temporarily under homeostatic conditions. Criteria (4) required that signatures develop relatively early in the disease, which we see to be true if the fractionating reservoir is sufficiently large. When a fractionation factor is imposed on a specific reservoir, the change in isotopic composition of other reservoirs is reflected quickly, typically on the timescale of months (Lauwens et al. 2016). However, given the nature of the conditions used in the box modelling, *i.e.*, that the body attempts to return to steady state Cu distributions if functioning properly, the results presented above may not be fully relevant to a patient that is seriously ill and unable to maintain homeostasis as expected. Although these parameters may be changed in future studies to explore other possible response timescales, we consider the estimates presented above as conservative since the inability of the body to return to steady-state would only lead to shorter timescales for the expression and detection of isotopic signatures.

Concluding remarks

While much remains to be learned on the exact mechanisms driving Cu isotope fractionations during the evolution of cancer and other diseases, consideration of first-order box-model scenarios allowed us to show that the lower δ^{65}Cu observed in the serum of breast cancer patients is not a result of tumor growth itself. Instead, these signatures are much more likely due to isotopic fractionation developing during organ failure (*e.g.*, liver failure) or in association with synergistic effects in otherwise healthy tissue, and may be used instead in pursuit of prognosis or diagnosis of liver-related diseases or cancers (Hastuti et al. 2020).

The future of mass spectrometry technology will undoubtedly yield even higher resolution measurements of isotopes, decreasing the analytical uncertainty by up to several-fold relative to currently achieved values. Hypothetically, it would not be unreasonable to expect resolving power to routinely reach 0.02 ‰ or better in the next decade. Given this possibility, reevaluation of Points (3) and (4) regarding ideal

diagnostic tools would be warranted. Point (3), pertaining to the resolvability of the signals, would be met even more easily, and the detection of changes due to any given disease would occur earlier in its progression, improving upon Point (4) as well. However, with this better precision comes the need to face the inherent difficulties associated with discerning meaningful signals from biological noise. Specifically, the precision of the measurement may exceed our understanding of the causes of variations within the system. In the case of copper, many studies have evaluated natural variations of serum δ^{65}Cu in healthy individuals and shown that they can fall within a large range (from ~ –0.6 to +0.2 ‰). Studies dedicated to understanding the exact drivers of isotope ratio variability for a given individual over time, as well as variability between different demographics, would have to be conducted to enable meaningful interpretations of these results with improved measurement precision.

As more kinetic and isotopic data become available, models like the one we described above may be improved and refined. In particular, one additional criterion of a diagnostic tool that should be explored as more clinical studies are performed is the uniqueness of the signature, *i.e.*, whether the appearance of the signature can be directly connected to cancer, or whether other diseases (*e.g.*, liver cirrhosis, Wilson's disease (Lamboux et al. 2020)) may also produce an identical result. Considering our observations that oxidative stress may generate similar signatures, it would be worthwhile to explore serum Cu isotopic compositions found in other diseases strongly linked to oxidative stress, such as cardiovascular (*e.g.*, atherosclerosis) and neurological (*e.g.*, Parkinson's, Alzheimer's) diseases (Pizzino et al. 2017). Unfortunately, due to the scarcity of serum isotopic data across the numerous other possible diseases at this writing, it is currently impossible to tell whether the drop in serum Cu isotopic composition in cancer patients is sufficiently distinctive. Finally, future considerations should include the effects of chemotherapeutic treatment on the liver. Given that cancer literature has widely documented the stress and imbalance imposed on liver metabolism in response to chemotherapy (Grigorian and O'brien 2014; Maor and Malnick 2013; Ramadori and Cameron 2010), it would be valuable

to understand whether chemotherapy may act as a confounding factor for the prognosis potential of Cu isotope ratios. Specifically, liver injury due to chemotherapy may alter serum Cu isotopic composition, adding to or potentially masking the signature from the original disease.

Most diagnostic tools work in conjunction with each other to help deduce the disease presented (*e.g.*, masses detected on CT scans are confirmed by immunostaining of tissue biopsies), and it seems δ^{65}Cu is no exception. To date, observations have shown that serum Cu isotope ratios may act as good nonspecific markers; at a minimum, it could be used as an initial filter in routine medical examinations to signal a need for more targeted tests that can then narrow down possible disease candidates. As the field looks towards potential medical applications of Cu isotope ratios, it will certainly be worthwhile to explore their use as part of a suite of diagnostic tools, including other isotope ratios (e.g., Zn (Hastuti et al. 2020), S (Balter et al. 2015)) or molecular markers.

References

Albaréde, F. (1996). *Introduction to Geochemical Modeling.* Cambridge University Press.

Albarède, F., Télouk, P., & Balter, V. (2017). Medical applications of isotope metallomics. *Non-Traditional Stable Isotopes*, *82*(October), 851–885. https://doi.org/10.2138/rmg.2017.82.20

Archer, C., & Vance, D. (2004). Mass discrimination correction in multiple-collector plasma source mass spectrometry: An example using Cu and Zn isotopes. *Journal of Analytical Atomic Spectrometry*, *19*(5), 656–665. https://doi.org/10.1039/B315853E

Balter, V., Nogueira, A., Paky, V., Jaouen, K., & Lamboux, A. (2015). Natural variations of copper and sulfur stable isotopes in blood of hepatocellular carcinoma patients. *Proceedings of the National Academy of Sciences, 112*(4), 1–4. https://doi.org/10.1073/pnas.1415151112

Bermin, J., Vance, D., Archer, C., & Statham, P. J. (2006). The determination of the isotopic composition of Cu and Zn in seawater. *Chemical Geology, 226*(3–4), 280–297. https://doi.org/10.1016/J.CHEMGEO.2005.09.025

Blockhuys, S., Celauro, E., Hildesjö, C., Feizi, A., Stål, O., Fierro-González, J. C., & Wittung-Stafshede, P. (2017). Defining the human copper proteome and analysis of its expression variation in cancers. *Metallomics, 9*(2), 112–123. https://doi.org/10.1039/c6mt00202a

Bondanese, V. P., Lamboux, A., Simon, M., Lafont, J. E., Albalat, E., Pichat, S., Vanacker, J. M., Télouk, P., Balter, V., Oger, P., & Albarède, F. (2016). Hypoxia induces copper stable isotope fractionation in hepatocellular carcinoma, in a HIF-independent manner. *Metallomics*, *8*(11), 1177–1184. https://doi.org/10.1039/C6MT00102E

Borrok, D. M., Wanty, R. B., Ridley, W. I., Wolf, R., Lamothe, P. J., & Adams, M. (2007). Separation of copper, iron, and zinc from complex aqueous solutions for isotopic measurement. *Chemical Geology, 242*(3–4), 400–414. https://doi.org/10.1016/J.CHEMGEO.2007.04.004

Brú, A., Albertos, S., Subiza, J. L., García-Asenjo, J. L., & Brú, I. (2003). The universal dynamics of tumor growth. *Biophysical Journal, 85*(5), 2948. https://doi.org/10.1016/S0006-3495(03)74715-8

Cadiou, J. L., Pichat, S., Bondanese, V. P., Soulard, A., Fujii, T., Albarède, F., & Oger, P. (2017). Copper transporters are responsible for copper isotopic

fractionation in eukaryotic cells. *Scientific Reports*, *7*(1). https://doi.org/10.1038/srep44533

Channon, M. B., Gordon, G. W., Morgan, J. L. L., Skulan, J. L., Smith, S. M., & Anbar, A. D. (2015). Using natural, stable calcium isotopes of human blood to detect and monitor changes in bone mineral balance. *Bone*, *77*, 69–74. https://doi.org/10.1016/J.BONE.2015.04.023

Costas-Rodríguez, M., Anoshkina, Y., Lauwens, S., Van Vlierberghe, H., Delanghe, J., & Vanhaecke, F. (2015). Isotopic analysis of Cu in blood serum by multi-collector ICP-mass spectrometry: A new approach for the diagnosis and prognosis of liver cirrhosis? *Metallomics*, *7*(3), 491–498. https://doi.org/10.1039/C4MT00319E

Costas-Rodríguez, M., Van Campenhout, S., Hastuti, A. A. M. B., Devisscher, L., Van Vlierberghe, H., & Vanhaecke, F. (2019). Body distribution of stable copper isotopes during the progression of cholestatic liver disease induced by common bile duct ligation in mice. *Metallomics*, 11(6), 1093–1103. https://doi.org/10.1039/C8MT00362A

Dunn, M. A., Green, M. H., & Leach, R. M. (1991). Kinetics of copper metabolism in rats: A compartmental model. *American Journal of Physiology – Endocrinology and Metabolism*, *261*(1). https://doi.org/10.1152/ajpendo.1991.261.1.e115

Eisenhauer, A., Müller, M., Heuser, A., Kolevica, A., Glüer, C. C., Both, M., Laue, C., Hehn, U. V., Kloth, S., Shroff, R., & Schrezenmeir, J. (2019). Calcium isotope ratios in blood and urine: A new biomarker for the diagnosis of osteoporosis. *Bone Reports*, *10*, 100200. https://doi.org/10.1016/J.BONR.2019.100200

Flórez, M. R., Costas-Rodríguez, M., Grootaert, C., Van Camp, J., & Vanhaecke, F. (2018). Cu isotope fractionation response to oxidative stress in a hepatic cell line studied using multi-collector ICP-mass spectrometry. *Analytical and Bioanalytical Chemistry*, 410(9), 2385–2394. https://doi.org/10.1007/S00216-018-0909-X/FIGURES/5

Förnvik, D., Lång, K., Andersson, I., Dustler, M., Borgquist, S., & Timberg, P. (2016). Estimates of breast cancer growth rate from mammograms and its relation to tumor characteristics. *Radiation Protection Dosimetry*, *169*(1–4), 151–157. https://doi.org/10.1093/RPD/NCV417

Fujii, T., Moynier, F., Blichert-Toft, J., & Albarède, F. (2014). Density functional theory estimation of isotope fractionation of Fe, Ni, Cu, and Zn among species relevant to geochemical and biological environments. *Geochimica et Cosmochimica Acta, 140*, 553–576. https://doi.org/10.1016/J.GCA.2014.05.051

Grigorian, A., & O'brien, C. B. (2014). Hepatotoxicity secondary to chemotherapy. *Journal of Clinical and Translational Hepatology, 2*(2), 95. https://doi.org/10.14218/JCTH.2014.00011

Hastuti, A. A. M. B., Costas-Rodríguez, M., Matsunaga, A., Ichinose, T., Hagiwara, S., Shimura, M., & Vanhaecke, F. (2020). Cu and Zn isotope ratio variations in plasma for survival prediction in hematological malignancy cases. *Scientific Reports, 10*(1), 1–12. https://doi.org/10.1038/s41598-020-71764-7

Heuser, A., & Eisenhauer, A. (2010). A pilot study on the use of natural calcium isotope (44Ca/40Ca) fractionation in urine as a proxy for the human body calcium balance. *Bone*, *46*(4), 889–896. https://doi.org/10.1016/J.BONE.2009.11.037

Heuser, L., Spratt, N. S., & Polk, H. C. (1979). Growth rates of primary breast cancers. *Cancer*, *43*(5), 1888-94. https://doi.org/10.1002/1097-0142(197905)43:5

Holland, H. D., & Turekian, K. K. (2014). *Treatise on Geochemistry* (2nd ed.). Elsevier.

Jaouen, K., Pouilloux, L., Balter, V., Pons, M. L., Hublin, J. J., & Albarède, F. (2019). Dynamic homeostasis modeling of Zn isotope ratios in the human body. *Metallomics, 11*(6), 1049–1059. https://doi.org/10.1039/C8MT00286J

Jeong, H., Ra, K., & Choi, J. Y. (2021). Copper, zinc and lead isotopic delta values and isotope ratios of various geological and biological Reference Materials. *Geostandards and Geoanalytical Research, 45*(3), 551–563. https://doi.org/10.1111/GGR.12379/ABSTRACT

Jomova, K., Makova, M., Alomar, S. Y., Alwasel, S. H., Nepovimova, E., Kuca, K., Rhodes, C. J., & Valko, M. (2022). Essential metals in health and disease. *Chemico-Biological Interactions, 367*, 110173. https://doi.org/10.1016/J.CBI.2022.110173

Krayenbuehl, P.-A., Walczyk, T., Schoenberg, R., Von Blanckenburg, F., & Schulthess, G. (2005). Hereditary hemochromatosis is reflected in the iron isotope composition of blood. *Blood, 105*(10), 3812-3816.

Kuo, H. W., Chen, S. F., Wu, C. C., Chen, D. R., & Lee, J. H. (2002). Serum and tissue trace elements in patients with breast cancer in Taiwan. *Biological trace element research*, *89*, 1–11.

Lamboux, A., Couchonnal-Bedoya, E., Guillaud, O., Laurencin, C., Lion-François, L., Belmalih, A., Mintz, E., Brun, V., Bost, M., Lachaux, A., & Balter, V. (2020). The blood copper isotopic composition is a prognostic indicator of the hepatic injury in Wilson disease †. *Metallomics*, *12*, 1781. https://doi.org/10.1039/d0mt00167h

Larner, F., Woodley, L. N., Shousha, S., Moyes, A., Humphreys-Williams, E., Strekopytov, S., Halliday, A. N., Rehkämper, M., & Coombes, R. C. (2015). Zinc isotopic compositions of breast cancer tissue. *Metallomics*, *7*(1), 107–112.

Lauwens, S., Costas-Rodríguez, M., Van Vlierberghe, H., & Vanhaecke, F. (2016). Cu isotopic signature in blood serum of liver transplant patients: A follow-up study. *Scientific Reports*, *6*(1), 1–9. https://doi.org/10.1038/srep30683

Levenson, C. W., & Janghorbani, M. (1994). Long-term measurement of organ copper turnover in rats by continuous feeding of a stable isotope. *Analytical Biochemistry*, *221*(2), 243–249. https://doi.org/10.1006/abio.1994.1408

Linder, M. C. (2013). *The Biochemistry of Copper* (Vol. 10). Springer Science & Business Media.

Mahan, B., Chung, R. S., Pountney, D. L., Moynier, F., & Turner, S. (2020). Isotope metallomics approaches for medical research. *Cellular and Molecular Life Sciences*, *77*(17), 3293–3309. https://doi.org/10.1007/s00018-020-03484-0

Maor, Y., & Malnick, S. (2013). Liver injury induced by anticancer chemotherapy and radiation therapy. *International Journal of Hepatology*, 2013, 1–8. https://doi.org/10.1155/2013/815105

Maréchal, C. N., & Albarède, F. (2002). Ion-exchange fractionation of copper and zinc isotopes. *Geochimica et Cosmochimica Acta*, *66*(9), 1499–1509. https://doi.org/10.1016/S0016-7037(01)00815-8

Maréchal, C. N., Télouk, P., & Albarède, F. (1999). Precise analysis of copper and zinc isotopic compositions by plasma-source mass spectrometry. *Chemical Geology*, *156*(1–4), 251–273. https://doi.org/10.1016/S0009-2541(98)00191-0

Margalioth, E. J., Schenker, J. G., & Chevion, M. (1983). Copper and zinc levels in normal and malignant tissues. *Cancer*, *52*(5), 868-872. https://doi.org/10.1002/1097-0142(19830901)52:5

Mason, T. F. D., Weiss, D. J., Horstwood, M., Parrish, R. R., Russell, S. S., Mullane, E., & Coles, B. J. (2004a). High-precision Cu and Zn isotope analysis by plasma source mass spectrometry, Part 1. Spectral interferences and their correction. *Journal of Analytical Atomic Spectrometry*, *19*(2), 209–217. https://doi.org/10.1039/B306958C

Mason, T. F. D., Weiss, D. J., Horstwood, M., Parrish, R. R., Russell, S. S., Mullane, E., & Coles, B. J. (2004b). High-precision Cu and Zn isotope analysis by plasma source mass spectrometry. Part 2. Correcting for mass discrimination effects. *Journal of Analytical Atomic Spectrometry*, *19*(2), 209–217. https://doi.org/10.1039/B306958C

Morgan, J. L. L., Skulan, J. L., Gordon, G. W., Romaniello, S. J., Smith, S. M., & Anbar, A. D. (2012). Rapidly assessing changes in bone mineral balance using natural stable calcium isotopes. *Proceedings of the National Academy of Sciences of the United States of America*, *109*(25), 9989–9994.

Moynier, F., Borgne, M. Le, Lahoud, E., Mahan, B., Mouton-Ligier, F., Hugon, J., & Paquet, C. (2020). Copper and zinc isotopic excursions in the human brain affected by Alzheimer's disease. *Alzheimer's & Dementia: Diagnosis, Assessment & Disease Monitoring*, *12*(1). https://doi.org/10.1002/DAD2.12112

Murphy, H., Jaafari, H., & Dobrovolny, H. M. (2016). Differences in predictions of ODE models of tumor growth: A cautionary example. *BMC Cancer*, *16*(1), 163. https://doi.org/10.1186/S12885-016-2164-X

Peel, K., Weiss, D., Chapman, J., Arnold, T., & Coles, B. (2007). A simple combined sample–standard bracketing and inter-element correction procedure for accurate mass bias correction and precise Zn and Cu isotope ratio measurements. *Journal of Analytical Atomic Spectrometry*, *23*(1), 103–110. https://doi.org/10.1039/B710977F

Pizzino, G., Irrera, N., Cucinotta, M., Pallio, G., Mannino, F., Arcoraci, V., Squadrito, F., Altavilla, D., & Bitto, A. (2017). Oxidative stress: harms and benefits for human health. *Oxidative Medicine and Cellular Longevity*, 2017. https://doi.org/10.1155/2017/8416763

Ramadori, G., & Cameron, S. (2010). Effects of systemic chemotherapy on the liver. *Annals of Hepatology*, *9*(2), 133–143. https://doi.org/10.1016/S1665-2681(19)31651-5

Ramos, D., Mar, D., Ishida, M., Vargas, R., Gaite, M., Montgomery, A., & Linder, M. C. (2016). Mechanism of copper uptake from blood plasma ceruloplasmin by mammalian cells. *PLOS ONE*, *11*(3), e0149516. https://doi.org/10.1371/JOURNAL.PONE.0149516

Rangarajan, R., Mondal, S., Thankachan, P., Chakrabarti, R., & Kurpad, A. V. (2018). Assessing bone mineral changes in response to vitamin D supplementation using natural variability in stable isotopes of Calcium in Urine. *Scientific Reports*, *8*(1). https://doi.org/10.1038/S41598-018-34568-4

Ross, A. C., Caballero, B., Cousins, R. J., Tucker, K. L., & Ziegler, T. R. (Eds.). (2012). *Modern nutrition in health and disease* (11th ed.). Lippincott Williams & Wilkins.

Russell, R., Beard, J. L., Cousins, R. J., Dunn, J. T., Ferland, G., Hambidge, K., Lynch, S., Penland, J. G., Ross, A. C., Stoecker, B. J., & Suttie, J. W. (2001). *Dietary Reference Intakes for Vitamin A, Vitamin K, Arsenic, Boron, Chromium, Copper, Iodine, Iron, Manganese, Molybdenum, Nickel, Silicon, Vanadium, and Zinc.* National Academies Press.

Scott, K. C., & Turnlund, J. R. (1994). Compartmental model of copper metabolism in adult men. *The Journal of Nutritional Biochemistry*, *5*(7), 342–350. https://doi.org/10.1016/0955-2863(94)90064-7

Selden, C., Schilling, K., Basu, A., & Yee, N. (2022). Experimental investigation of amino acid binding as a mechanism for fractionating metal stable isotopes. Annual V.M. *Goldschmidt Conference*.

Shroff, R., Fewtrell, M., Heuser, A., Kolevica, A., Lalayiannis, A., McAlister, L., Silva, S., Goodman, N., Schmitt, C. P., Biassoni, L., Rahn, A., Fischer, D. C., & Eisenhauer, A. (2021). Naturally occurring stable calcium isotope ratios in body compartments provide a novel biomarker of bone mineral balance in children and young adults. *Journal of Bone and Mineral Research*, *36*(1), 133–142. https://doi.org/10.1002/JBMR.4158

Skulan, J., Bullen, T., Anbar, A. D., Puzas, J. E., Shackelford, L., LeBlanc, A., & Smith, S. M. (2007). Natural calcium isotopic composition of urine as a marker of bone mineral balance. *Clinical Chemistry*, *53*(6), 1155–1158. https://doi.org/10.1373/CLINCHEM.2006.080143

Skulan, J., & DePaolo, D. J. (1999). Calcium isotope fractionation between soft and mineralized tissues as a monitor of calcium use in vertebrates. *Proceedings of the National Academy of Sciences of the United States of America*, *96*(24), 13709–13713. https://doi.org/10.1073/PNAS.96.24.13709/ASSET/AB91944C-0129-4281-9359-DF8D3806091B/ASSETS/GRAPHIC/PQ2394049004.JPEG

Sossi, P. A., Halverson, G. P., Nebel, O., & Eggins, S. M. (2015). Combined separation of Cu, Fe and Zn from rock matrices and improved analytical protocols for stable isotope determination. *Geostandards and Geoanalytical Research, 39*(2), 129–149. https://doi.org/10.1111/J.1751-908X.2014.00298.X/ABSTRACT

Spratt, John S., Greenberg, Richard A., Heuser, L. S. (1986). Geometry, growth rates, and duration of cancer and carcinoma in situ of the breast before detection by screening. *Cancer Research, 46*(2). https://aacrjournals.org/cancerres/article/46/2/970/490366/Geometry-Growth-Rates-and-Duration-of-Cancer-and

Sullivan, K., Layton-Matthews, D., Leybourne, M., Kidder, J., Mester, Z., & Yang, L. (2020). Copper isotopic analysis in geological and biological reference materials by MC-ICP-MS. *Geostandards and Geoanalytical Research*, *44*(2), 349–362. https://doi.org/10.1111/GGR.12315/ABSTRACT

Sullivan, K. V., Moore, R. E. T., Capper, M. S., Schilling, K., Goddard, K., Ion, C., Layton-Matthews, D., Leybourne, M. I., Coles, B., Kreissig, K., Antsygina, O., Coombes, R. C., Larner, F., & Rehkämper, M. (2021). Zinc stable isotope analysis reveals Zn dyshomeostasis in benign tumours, breast cancer, and adjacent histologically normal tissue. *Metallomics, 13*(6), 27. https://doi.org/10.1093/MTOMCS/MFAB027

Télouk, P., Plissonnier, M.-L., Merle, P., Zoulim, F., Fares, N., Guilloreau, P., Parent, R., Bacchetta, J., Danan, M., Carandina, S., & Albarède, F. (2022). Copper isotope evidence of oxidative stress–induced hepatic breakdown and the transition to hepatocellular carcinoma. *Gastro Hep Advances, 1*(3), 480–486. https://doi.org/10.1016/j.gastha.2022.02.024

Télouk, P., Puisieux, A., Fujii, T., Balter, V., Bondanese, V. P., Morel, A. P., Clapisson, G., Lamboux, A., & Albarede, F. (2015). Copper isotope effect in serum of cancer patients. A pilot study. *Metallomics, 7*(2), 299–308. https://doi.org/10.1039/c4mt00269e

Tennant, A., Rauk, A., & Wieser, M. E. (2017). Computational modelling of the redistribution of copper isotopes by proteins in the liver. *Metallomics*, 9, 1809. https://doi.org/10.1039/c7mt00248c

Turnlund, J. R. (1998). Human whole-body copper metabolism. *The American Journal of Clinical Nutrition, 67*(5), 960S-964S. https://doi.org/10.1093/ajcn/67.5.960S

Van Campenhout, S., Hastuti, A. A. M. B., Lefere, S., Van Vlierberghe, H., Vanhaecke, F., Costas-Rodríguez, M., & Devisscher, L. (2020). Lighter serum copper isotopic composition in patients with early non-alcoholic fatty

liver disease. *BMC Research Notes, 13*(1), 1–6. https://doi.org/10.1186/S13104-020-05069-3/TABLES/2

Van Heghe, L., Delanghe, J., Van Vlierberghe, H., & Vanhaecke, F. (2013). The relationship between the iron isotopic composition of human whole blood and iron status parameters. *Metallomics, 5*(11), 1503–1509. https://doi.org/10.1039/C3MT00054K

Welch, H. G., Prorok, P. C., O'Malley, A. J., & Kramer, B. S. (2016). Breast-cancer tumor size, overdiagnosis, and mammography screening effectiveness. *New England Journal of Medicine, 375*(15), 1438–1447.

Yang, S. C., Welter, L., Kolatkar, A., Nieva, J., Waitman, K. R., Huang, K. F., Liao, W. H., Takano, S., Berelson, W. M., West, A. J., Kuhn, P., & John, S. G. (2018). A new anion exchange purification method for Cu stable isotopes in blood samples. *Analytical and Bioanalytical Chemistry, 411*(3), 765–776. https://doi.org/10.1007/S00216-018-1498-4